RICE UNIVERSITY

Near-Field Radiative Energy Exchange Analysis of Nanospheres and Nanorods: Space Waste Heat Recovery Device Design

by

Laurie Yvette Carrillo

A THESIS SUBMITTED
IN PARTIAL FULFILLMENT OF THE
REQUIREMENTS FOR THE DEGREE

Doctor of Philosophy

APPROVED, THESIS COMMITTEE:

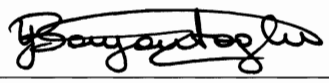

Yildiz Bayazitoglu, Harry S. Cameron Chair Professor of Mechanical Engineering, Department of Mechanical Engineering and Materials Science

Andrew Dick, Assistant Professor, Department of Mechanical Engineering and Materials Science

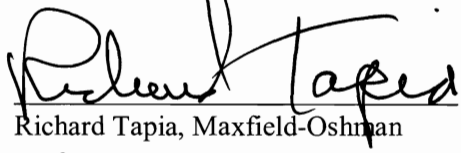

Richard Tapia, Maxfield-Oshman Professor, Department of Computational and Applied Mathematics

HOUSTON, TEXAS
MAY 2011

Abstract

Near-Field Radiative Energy Exchange Analysis of Nanospheres and Nanorods: Space Waste Heat Recovery Device Design

by

Laurie Yvette Carrillo

In the present study, a theoretical method for sphere-to-sphere radiative heat exchange is implemented for silica, lithium fluoride, and arsenic triselenide nanospheres of equal and unequal radii. The method is extended to approximate a sphere-to-plane geometric configuration via an asymptotic method. The asymptotic method calls for an iterative process by which the radiative exchange is continuously calculated up to convergence as the radii of one microsphere is increased. These results are compared to previously published theoretical approximations and experimental data.

A theoretical method for cylinder-to-cylinder radiative heat exchange is formulated. The method utilizes a modified version of the numerical method for near-field sphere-to-sphere radiative exchange. Modifications were made to the numerical procedure to make it applicable to cylindrical geometry of nanorods. Nanorods investigated had length to diameter ratios of 3:1 and 7:1. The heat exchange of nanorods is plotted vs. gap to assess the impact of near-field radiative transfer as gap decreases. Graphical results of energy vs. nanorod radii are also presented. A nanorod-to-plane configuration is estimated utilizing a nanorod asymptotic

method. The nanorod-to-nanorod method approximates a nanorod-to-plane geometric configuration when one nanorod radii is held constant, and the second nanorod radii is iteratively increased until the corresponding radiative exchange converges.

A theoretical method for cylinder-to-cylinder radiative heat exchange is formulated by utilizing a sphere approximation method. The sphere approximation method calls for dividing the cylinders into smaller connected spheres and applying a previously published numerical method for near-field sphere-to-sphere radiative exchange. The overall radiative power exchange is obtained by an additive ray tracing assumption. These results are compared to results produced by a rigorous cylinder-to-cylinder radiative heat exchange method. The heat exchange of nanorods is plotted vs. gap to assess the impact of near-field radiative transfer as gap decreases. The unit sphere method is applied to nanorod configurations having length to diameter ratios of 3:1, 5:1, 7:1. Graphical results of energy vs. nanorod radii are presented. A nanoradii/gap dimensionless relationship caused by geometric effects is found and related to power for nanorods of different aspect ratios and temperatures. A V-shaped configuration is considered with the results plotted for heat exchange vs. angle. An assessment of the number of spheres required to produce an accurate approximation of the V-shaped configuration of nanorods is presented. An error analysis of this method based on a ray blocking assumption from neighboring spheres is discussed.

An analysis is presented of a new device that utilizes near-field radiative heat transfer incorporated with pyroelectric materials to convert spacecraft waste heat to electrical energy. A background of pyroelectric material devices is presented to show the background as applied to this application. Near-field plane-to-plane radiative heat exchange is implemented for calculation of the near-field radiative heat exchange within the device. The numerical method is

based upon an asymptotic approximation shown in previous work for sphere-to-sphere. One sphere is iteratively increased with the radiative heat exchange continuously calculated until convergence, whereby, the geometric configuration approaches plane-to-sphere. By superimposing this method on multiple spheres, the plane-to-plane approximation is achieved. This procedure is applied for silica and lithium fluoride coated planes. Near-field radiative heat transfer results expected in the spacecraft device are presented.

Acknowledgements

I would like to thank my PhD advisor, Dr. Yildiz Bayazitoglu for her guidance during the process of creating this research work. Her experience and knowledge was essential for me to successfully complete this research. She enabled me to grow with her patient support throughout the process. I would also like to thank my PhD thesis committee, Dr. Andrew Meade, Dr. Andrew Dick, and Dr. Richard Tapia. They shared their expertise and provided suggestions that allowed this work to fully develop.

I extend my appreciation to those organizations that supported me financially. Financial support included the Society of Women Engineers' Presidential Fellowship, the Zonta International Amelia Earhart Fellowship, and the Hispanic Engineers National Achievement Award Conference (HENAAC)/Daimler Chrysler Fellowship. I also give a special thanks to NASA for their funding support towards my education throughout the years.

I extend my deepest gratitude to my family and friends for their encouragement and belief in my success. Their love and support gave me the strength to overcome the obstacles along the way. Finally, I am thankful to God for the opportunity to experience these years of blessings, challenges, and life lessons. I acknowledge that only with God's grace can such an accomplishment be possible.

Table of Contents

Nomenclature

English

A	=	surface area, m^2
a	=	cylinder radius, m
b	=	Wein's displacement constant, 2.898×10^{-3} m·K
C	=	capacitance, F
c	=	pilot vector, unitless
D_{PE}	=	electric displacement of pyroelectric, V/m
$\overline{\boldsymbol{D}}$	=	intermediate coefficient matrix, unitless
E	=	electric field, V/m
E_{PE}	=	electric field of pyroelectric, V/m
$\overline{\overline{G_E}}$	=	electric dyadic Green function, 1/m
$\overline{\overline{G_M}}$	=	magnetic dyadic Green function, 1/m
H	=	magnetic field, V/m
h	=	time harmonic function, unitless
$H^{(1)}$	=	Hankel function, unitless
$\hbar$	=	Dirac constant, 1.055×10^{-34} J·s
J	=	cylindrical Bessel function of the 1st kind, unitless
j	=	spherical Bessel function of the 1st kind, unitless
$\vec{J}$	=	current density, A/m^2

k_b = Boltzmann constant, 1.381×10^{-23} J/K

$\vec{k}$ = wave propagation vector, 1/m

L = Legendre polynomial, unitless

$\vec{M}$ = solenoidal vector wave function

$\vec{N}$ = solenoidal vector wave function

r = point location, m

R_c = reflection coefficient, unitless

$\overline{\boldsymbol{R}}$ = reflection coefficient matrix, unitless

T = temperature, K

t = thickness, m

T_c = transmission coefficients, unitless

V = volume

V_{PE} = voltage of the pyroelectric, V

x = Bessel function argument, unitless

Y = cylindrical Bessel function of the 2nd kind, unitless

y = spherical Bessel function of the 2nd kind, unitless

Greek

δ_{lm} = Kronecker delta, unitless

δ = Dirac delta function, 1/m

ε = permittivity, F/m

ε_0 = permittivity of a vacuum, 8.854×10^{-12} F/m

ε'' = imaginary part of dielectric function, unitless

θ = mean energy of Planck oscillator, J

λ = wavelength in vacuum, m

μ = permeability, H/m

μ_0 = permeability of vacuum, $4\pi \times 10^{-7}$ H/m

ω = angular frequency, rad/s

ρ = radial distance from the z axis, m

ϕ = azimuthal angle, degrees

ψ = scalar wave, V/m

Subscripts

i = first Cartesian component

j = second Cartesian component

m = order of function

n = order of function

max = maximum

Chapter 1

Introduction

1.1 Motivation

The area of microtechnology and nanotechnology research is progressing at a very fast pace in all areas of science and engineering development. Microtechnology indicates those systems that exist at the microscale level or micrometer level. The current state of the art electronics exist in this regime. Nanotechnology development refers to those systems at the atomic or molecular scale level, normally 1 to 100 nanometers. Nanotechnology has a wide span of potential benefits to society. These include making possible lifesaving medical robots, cryobiological treatments of cancerous tissues, high frequency circuit boards, advanced energy storage systems, and unprecedented water treatment capabilities. Of critical importance to developing these systems, is an understanding of the thermal transport that can occur at the nanoscale level, specifically the radiative transfer known as near-field radiative heat transfer. This research takes a look at the near-field radiative heat transfer regime.

1.2 Statement of problem

Traditional far-field radiative energy transport theories that are applicable at the macroscale become unusable at the nanoscale due to a breakdown in the assumptions that they are based on. These assumptions, while true with far-field radiative transfer at the macroscale level, are no longer valid at the nanoscale where near-field radiative often dominates. This is due to the

occurrence of near field radiative transfer from radiation tunneling. Radiation tunneling is supported when the separation distance is less than the dominant wavelength. The surface evanescent waves of one object can tunnel and transfer heat into the neighboring body. There is an increase in energy transfer than what would be predicted by far-field alone. The evanescent waves decay at distances larger than the dominant wavelength, which is typical for macroscopic cases. The traditional radiative transfer equations which account for far-field transfer alone are an accurate representation for most macroscopic cases since the near-field evanescent waves have decayed before reaching the neighboring body. However, in the nano regime, often the separation distances fall below the critical separation distances, mandating an alternate computation procedure to incorporate the near-field effects. Thus, it is required to take a step back to the fundamental Maxwell's equations to derive the radiative heat transfer. This will ensure that not only will the traditional far-field radiation be accounted for, but also the dominant near-field radiative energy.

1.3 Objective

The aim of this work is to numerically represent and investigate the radiative transfer below the critical separation distance whereby near-field energy transfer is the dominant heat transfer method. Nanospheres and nanorods of a variety of sizes and configurations are considered for the near-field radiative transfer effects. Several different materials are considered for the composition of the nanospheres and nanorods. The calculation is done by utilizing the electromagnetic fundamentals whereby the Poynting vector is derived from the vector wave fields. This procedure is then modified to calculate an asymptotic approximation involving nanorods/nanospheres and planes. A simplified model for radiative power determination is developed and compared for nanorods. This simplified model is based on breaking the nanorods

into smaller nanospheres and computing the nanosphere by nanosphere power. Finally, the research is applied to a potential space application involving electrical energy production by converting waste heat from a pyroelectric device. This document presents the approach and results used for this thermal analysis.

1.4 Contribution

In order to truly utilize the potential of nanotechnology, it is imperative that we have a full understanding of as much of the physics that occurs as possible. This thesis rigorously considers the radiative energy transfer for a variety of different nanosphere configuration. The nanorod-to-nanorod calculation procedure is developed and applied. A simplified nanorod procedure is considered via spherical divisions and compared to the rigorous method. The calculation procedure is adapted for nanosphere-to-plane, and nanorod-to-plane. This is achieved through an asymptotic method that involves iteratively increasing the sphere until it estimates a plane. When the results converge to a specified error criterion, the approximation is acquired. As a last step, the experience gained from this research is applied to a novel space application whereby improved heat transfer is shown to be possible using the design proposed. The application has the potential to create useful electrical energy from waste heat that previously is radiated into space at 100% loss to the spacecraft system.

1.5 Structure of Thesis

The thesis is structured such that the first chapter presents an overview of the content of the material. The second chapter covers the nanosphere configuration research. The third chapter deals with nanorods. The fourth chapter presents the simplified nanorod method using spherical divisions. The final chapter details the application of the investigated methods to a space

application. Each of the following chapters covers a particular aspect of the research. The chapters are presented such that not only can they be read in progressive order in the full dissertation format, but also as stand-alone works. Each chapter contains its own background material and references to ease the reader that is interested in one particular aspect of the thesis. However, the chapters are ordered such that the reader who will study the full dissertation, will do so in a logical progressive order.

Chapter 2

Nanosphere Near-field Radiative Heat Exchange Analysis

2.1 Introduction

When two bodies exchanging radiation at a dominant wavelength, λ, are at a distance λ apart or less, near-field radiation effects are observed. Since the separation distance is based on wavelength, it is also dependent on temperature as described by Wein's displacement law. Wein's displacement law states that the dominant wavelength of radiative emission is inversely proportional to the temperature of the body according to the formula:

$$\lambda_{max} = \frac{b}{T}. \tag{2.1}$$

Here, Wein's displacement constant, b, is equivalent to 2.898×10^{-3} m·K. As the temperature of the bodies increases, the dominant wavelengths of radiative exchange become shorter. This means that the near-field domination distance between the two bodies decreases as the temperature increases. Traditional radiative heat transfer equations that are used to describe typical macroscale heat exchange neglect near-field radiation. This is an accurate representation when the bodies are farther apart than λ, which is the case in most macroscopic situations. However, at the nanoscale, when radiative transfer often includes near-field effects, these equations are no longer applicable. The radiative exchange is underpredicted by traditional radiative heat transfer equations.

Discussion of the limits of the laws of macroscopic heat transfer was published in [1]. Recently there has been significant interest and advancements in describing radiative exchange

including near-field effects [1, 2]. Near-field radiative exchange occurs because of evanescent waves. These waves occur at the boundary of the material, but rapidly decay as the distance away from the boundary increases. When a second body is brought near enough to the first, such that the evanescent wave has not yet decayed, the evanescent wave can tunnel into the second body. This radiation tunneling phenomena generates the near-field energy transfer. An editorial overview of micro/nanoscale radiative heat transfer work was conducted in [3]. The radiative transfer of two semi-infinite bodies at nanometric distances has been investigated in [4]. Equations that define radiative heat transfer between two spherical nanoparticles assuming dipole point sources, electromagnetic energy density near a surface, and the near-field radiative transfer between two planar surfaces is covered in [1]. A solution for radiative exchange including near-field effects beyond the dipole approximation has been developed for two spherical bodies by Narayanaswamy and Chen in [5]. Also, is an application of this solution to calculate the exchange between two silica microspheres of equal radii. Results of this method are compared to experimental data in [6]. The fields are written in terms of Dyadic Green's Function (DGF). The Fluctuation Dissipation Theorem (FDT) is utilized and covered in detail in [7-9]. A more in-depth look at DGFs is found in [10-12]. Bessel functions are utilized to express various equations mathematically. Details of Bessel function are found in [13-15]. A look at the thermal emission and exchange among an ensemble of spheres is examined in [16].

In this paper the procedure presented by Narayanaswamy and Chen in [5] is utilized. For verification purposes, and to ensure that the procedure was being properly applied, the silica microsphere of equal radii case from [5] was duplicated. The next step was to look at additional cases that had not been investigated. The smaller nanoscale regime was investigated. It has been stated by [5] that this regime can be approximated adequately by the dipole approximation. We

would expect the dipole approximation to yield approximately the same values as those presented here. A comparison of the two methods was done and included in the results section. Results agree for most of the gap range. As the gap decreased for the range of radii of spheres investigated in this paper, the accuracy also seems to decrease. The more rigorous procedure in [5] is utilized in this paper in order to attain increased accuracy in these lower gap ranges, as well as to gain increased familiarity with the method. The procedure in [5] was also applied to spheres of unequal radii. In addition to silica, the authors investigated other materials in the sphere-to-sphere configuration. An analysis was also done of the sphere-to-plane geometric configuration. This paper presents the results utilizing a new asymptotic method. This was done by taking the sphere-to-sphere case and calculating the radiative exchange iteratively. The radius of one sphere was iteratively increased with the radiative exchange recalculated each time. This process was continued until the value calculated did not change significantly. These results were compared to experimental results acquired by Narayanaswamy, Shen, and Chen in [6]. Theoretical results were also presented in [6] but by a different method. In [6], the theoretically calculated sphere-to-sphere radiative exchange curve was fit to the experimental data by adjusting a multiplier and adding an adjusted constant. The asymptotic method results in this work more closely match the experimental data. The work presented in this paper is done to contribute to the understanding of near-field radiative exchange which has applications in nanomanufacturing, near-field thermal photovoltaic devices, and nanostructure imaging [17].

2.2 Formulation

We aim to calculate the Poynting vector, E x H, from the electromagnetic wave fields E and H to determine the spectral radiative exchange between spheres. These electromagnetic wave fields deal directly with emission of thermal radiation. We can then integrate over the

wavelength to produce the total radiative exchange between the spheres. The Poynting vector is given in [5] as:

$$\begin{aligned}&\left\langle E_{i\omega} H^{*}_{j\omega} \right\rangle \\ &= i\omega\mu_0 \int_V d^3 r' \left\{ \overline{\overline{G_E}}(\vec{r}_1, \vec{r}, \omega) \overline{\overline{G_M}}^{*}(\vec{r}_1, \vec{r}', \omega) \left\langle \vec{J}_l(\vec{r}, \omega) \vec{J}^{*}_m(\vec{r}', \omega) \right\rangle \right\}\end{aligned} \tag{2.2}$$

where $\overline{\overline{G_E}}(\vec{r}_1, \vec{r}, \omega)$ and $\overline{\overline{G_H}}(\vec{r}_1, \vec{r}, \omega)$ are the DGFs due to a source at $\vec{r}$. Here, an additional mathematical technique involving kernals called DGFs which utilize second rank dyad tensors is incorporated. DGFs are covered in detail in [10-12]. The integration is performed over the entire volume V containing the source. μ_0 is the permeability of vacuum, and $\vec{J}(\vec{r}, \omega)$ is the Fourier component of fluctuating current. To deal with the phenomena of fluctuation, a statistical average must be included within the formulation. This is denoted as $\langle \cdot, \cdot \rangle$. The equation can be manipulated further by the application of the Fluctuation Dissipation Theorem (FDT) developed by Rytov in [9]. This theorem states that the density matrix for thermal fluctuations can be expressed in terms of $\theta(\omega, T)$ or the mean energy of the quantum oscillator where:

$$\theta(\omega, T) = \hbar\omega \Big/ \left(\exp\left(\hbar\omega \Big/ k_b T \right) - 1 \right). \tag{2.3}$$

There are several different forms of the FDT. The one utilized in this work is from [7] shown as follows:

$$\left\langle \vec{J}_l(\vec{r}, \omega) \vec{J}_m^{*}(\vec{r}', \omega) \right\rangle = \omega \varepsilon_0 \varepsilon''(\omega) \theta(\omega, T) \delta_{lm} \delta(\vec{r} - \vec{r}') \tag{2.4}$$

where $\varepsilon''(\omega)$ is the imaginary part of the dielectric function, and ε_0 is the permittivity of a vacuum. Details of this calculation process and applicable computational convergence analysis information are given in [5, 10]. By substitution, the following can then be written:

$$\left\langle E_i(\vec{r}_1,\omega)H_j^*(\vec{r}_1,\omega)\right\rangle = \frac{i\varepsilon_o\varepsilon''(\omega)\mu_0\omega^2\theta(\omega,T)}{\pi}\int_V d^3r\left\{\left(\overrightarrow{G_E}(\vec{r}_1,\vec{r},\omega)\overrightarrow{G_H^*}(\vec{r}_1,\vec{r}',\omega)\right)_{ij}\right\} \tag{2.5}$$

The Fourier component of the fluctuating electric and magnetic field at any point r_1 outside a volume containing the sources is given by [12] as:

$$\vec{E}(\vec{r}_1,\omega) = i\omega\mu_0\int_V \overline{\overline{G_E}}(\vec{r}_1,\vec{r},\omega)\cdot\vec{J}(\vec{r},\omega)d^3r \tag{2.6}$$

$$\vec{H}(\vec{r}_1,\omega) = \int_V \overline{\overline{G_H}}(\vec{r}_1,\vec{r},\omega)\cdot\vec{J}(\vec{r},\omega)d^3r \tag{2.7}$$

where $\overline{\overline{G_E}}(\vec{r}_1,\vec{r},\omega)$ and $\overline{\overline{G_H}}(\vec{r}_1,\vec{r},\omega)$ are the DGFs due to a source at $\vec{r}$.

2.3 Results

Figure 2.1 details a comparison between the dipole approximation of radiative transfer described by Joulain in Ref. 1 vs. the rigorous method presented by Narayanaswamy and Chen in Ref. 5. Based on these results, the calculated values agree as the gap increases. This seems to be true due to the fact that as the gap increases, the dipole geometry is more closely duplicated. To maintain accuracy in the entire range of investigation, the more rigorous method in Ref. 5 was utilized in the remaining graphs.

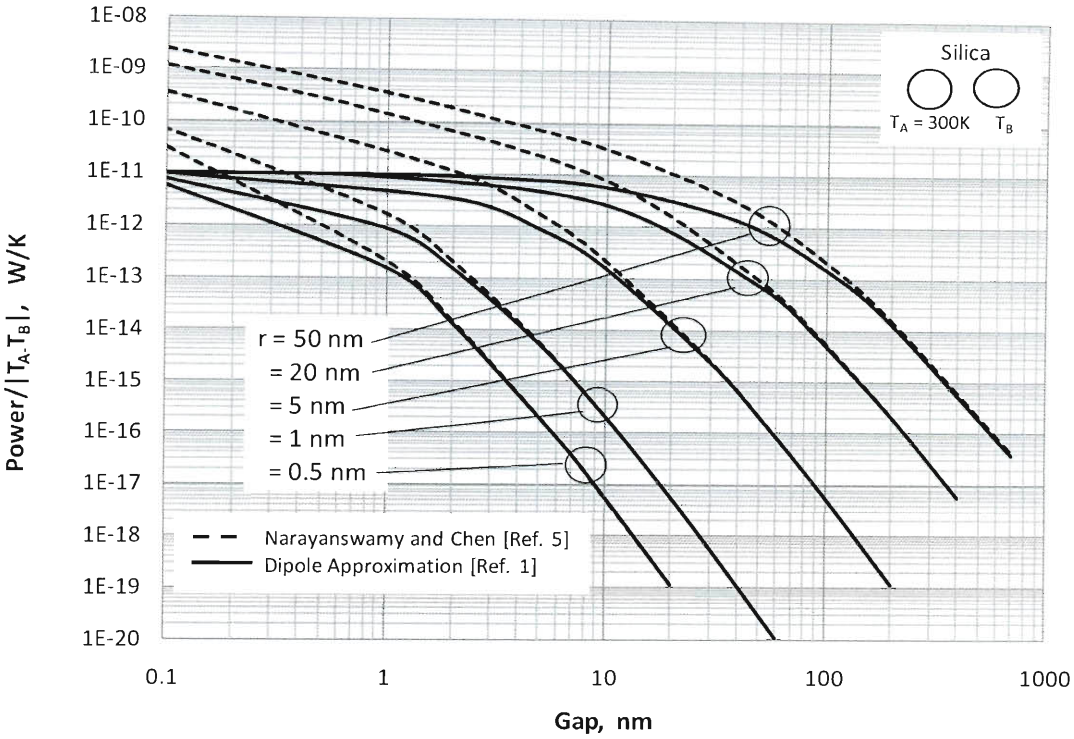

Figure 2.1: The Dipole Approximation Method in [1] vs. the more rigorous method in [5].

Figure 2.2 shows the results calculated compared to published results from Narayanaswamy and Chen in [5]. This was done for microspheres from 1-25 μm at varying separation gaps. Radiative exchange power over temperature difference vs. gap is plotted on a log-log graph. The data is plotted $T_A \rightarrow T_B$ as described in [5]. The radiative exchange between two microspheres is analyzed to validate that computational procedures produce results in a reasonable range as published data. The differences between the two results are due to the fact that graphical results and not exact numerical values were given in [5]. The authors estimated the numerical values by pulling points off the graph of [5] and plotting it with their results.

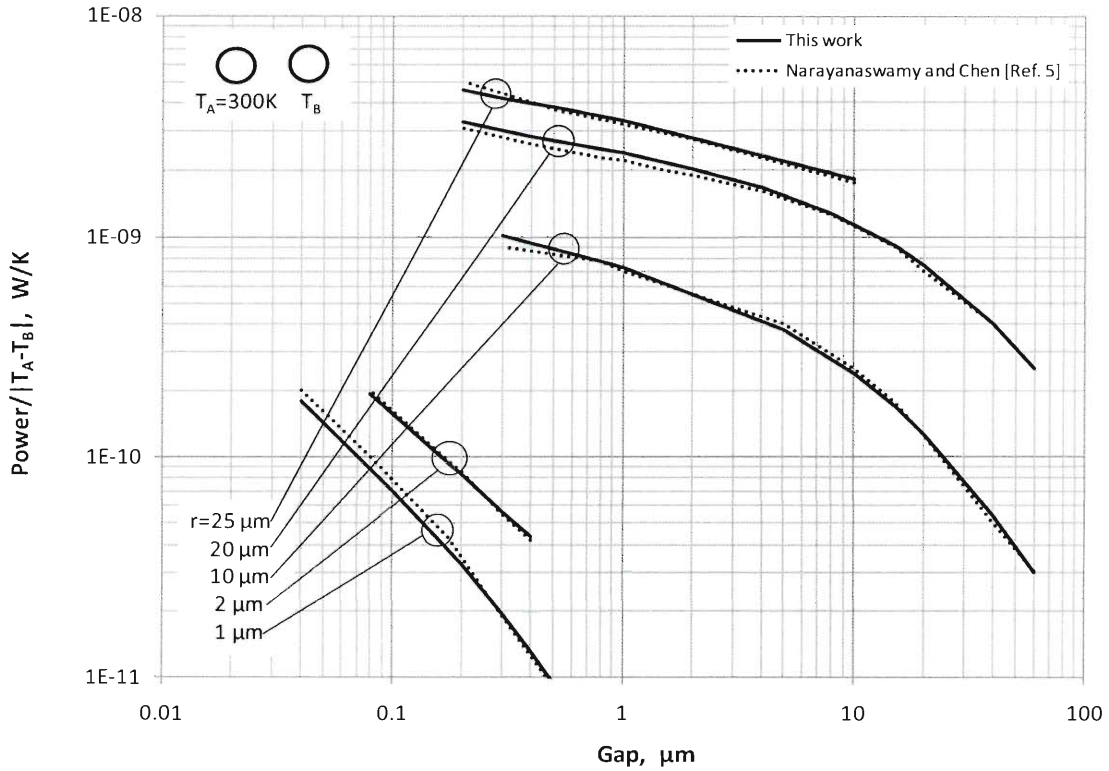

Figure 2.2: Calculated vs. Published Values for Microscale Silica Spheres of Equal Radii

The radiative exchange between a 25 μm nanosphere and planar substrate are shown in Figure 2.3. Note that the experimental data only includes near-term radiative heat transfer and neglects far-field radiative effects. The far- field effects had to be subtracted from the total theoretical radiative exchange computed from the calculation process in this work. A best fit line was acquired based on an equation containing a linear contribution proportional to the gap and a power contribution inversely proportional to the gap. The linear contribution representing the far- field effects was then subtracted. The dark line is the best fit line corresponding to the experimental data from [6]. The dotted line is a curve acquired by taking the n from a best fit $y=Ax^{-n} + B$ curve for two 25 μm spheres and adjusting A and B to fit the experimental data. This procedure and data are presented in [6]. The mean error for this curve is 0.070 nW/K. The

dotted line represents the asymptotic approach utilized to approximate the radiative exchange between the planar media and nanosphere. The results generated were acquired by beginning with two spheres at 25 μm. One of the spheres was slowly increased and the radiative exchange recalculated until convergence. Convergence was defined as $\frac{x_2 - x_1}{x_1} < 0.05$ where x_1 and x_2 represent two subsequent calculated results. The radius was increased to approximately 250 μm to reach the convergence criteria. For the cases tested, gap influenced the time it took for the results to be acquired, but did not have a significant effect on when convergence was achieved. The mean error of the theoretical asymptotic approximation presented in this work is 0.032 nW/K. This is a 54% increase in the overall accuracy from the previously presented data when looking at the range from 3-10 μm. However, below 3μm, the results generated by the asymptotic method in this paper are in agreement with those calculated by Narayanaswamy, Shen, and Chen in [6].

Additional radiative exchange calculations for various nanosphere scenarios that have not been previously investigated were also analyzed. Additional configurations include radiative exchange between spheres of different temperatures, different materials, different radii ratios, and smaller nanosphere radii down to r = 0.5 nm. These graphs include both the effects of near-field and far-field exchange. The results that follow represent these cases. Figure 2.4 shows results for the radiative exchange versus gap between two same size silica nanospheres. The range of radii is 50 nm down to 0.5 nm. The temperatures included are for the cases of T_A=1000K, 500K, and 300K.

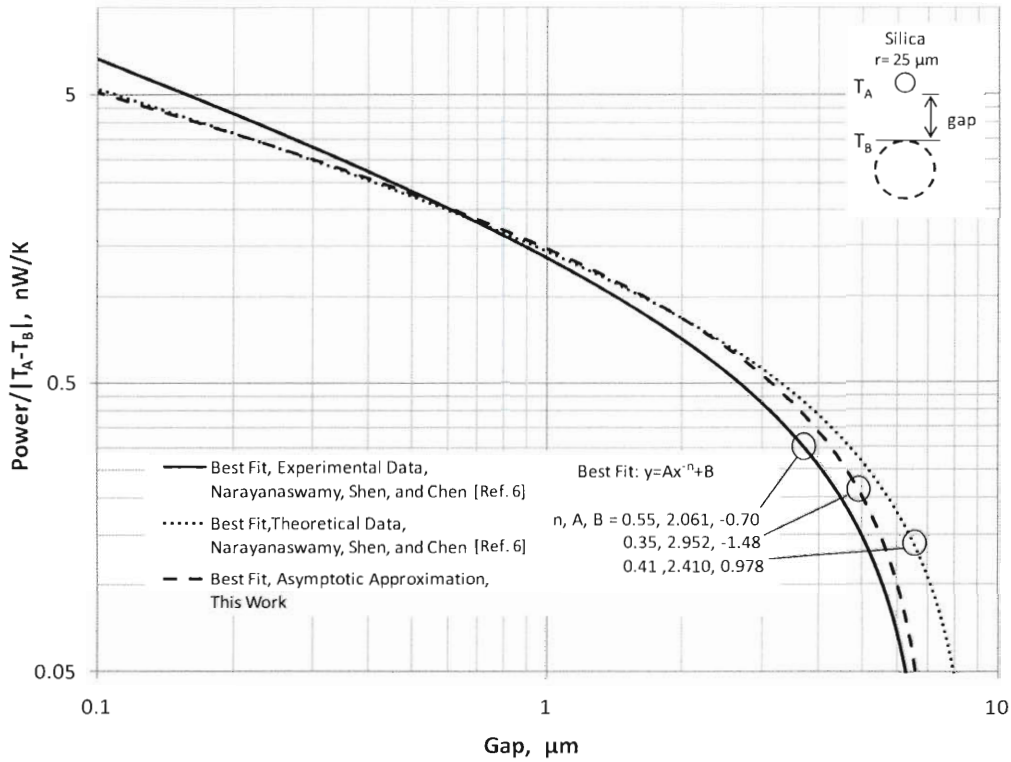

Figure 2.3 Sphere to Plane Radiative Exchange.

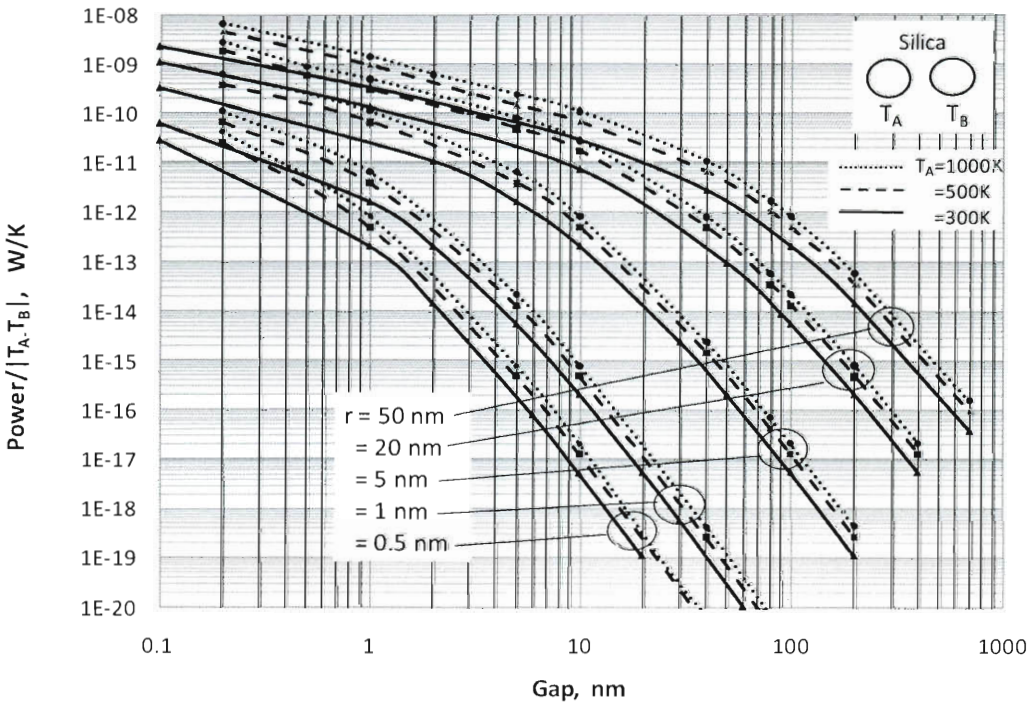

Figure 2.4 Sphere-to-Sphere Radiative Exchange: Silica, Equal Radii, Nanoscale

Several different materials were investigated for consideration of inclusion in thermal analysis. The primary material of investigation is amorphous silica. This is because experimental data, theoretical data, and resonant behavior of silica at the nanoscale are available in [5, 6]. Additional materials considered for investigation were lithium niobate, sodium chloride, cubic carbon, arsenic triselenide-crystalline, silicon dioxide-alpha crystalline, titanium dioxide, potassium chloride, silicon monoxide, arsenic triselenide, silicon nitride, and lithium fluoride. The availability of data, technological applications, and feasibility toward analysis were assessed. Lithium niobate, arsenic triselenide-crystalline, silicon dioxide-alpha crystalline, and titanium dioxide have refractive indexes that varied with axis making them difficult for analysis. The softness of sodium chloride makes its applications limited. The hardness of cubic carbon results in an unreasonable processing expense to create spherical geometries. Potassium chloride is hygroscopic, attracts water molecules, and therefore has limited applications. Data for silicon nitride, and silicon monoxide had limited data available. Arsenic triselenide and lithium fluoride had available data at the frequency range of interest, refractive index data that did not vary with axis, and technological applications. For these reasons, these materials were also included in the analysis. Properties were taken from [18].

Figure 2.5 and 2.6 display calculated values similar to Figure 2.4, but for lithium fluoride and arsenic triselenide. These results are for the temperature case of T_A=300K. The calculated values range from 1e-9 to1e-22 W/K for arsenic triselenide, and from 1e-8 to 1e-19 for lithium flouride. When comparing the material results in Figures 2.4, 2.5 and 2.6, lithium flouride is shown to support the greatest degrees of radiative exchange, with the arsenic triselenide supporting the least. There is roughly a two order of magnitude difference between the radiative exchange calculated for lithium flouride than for the same configuration in arsenic triselenide.

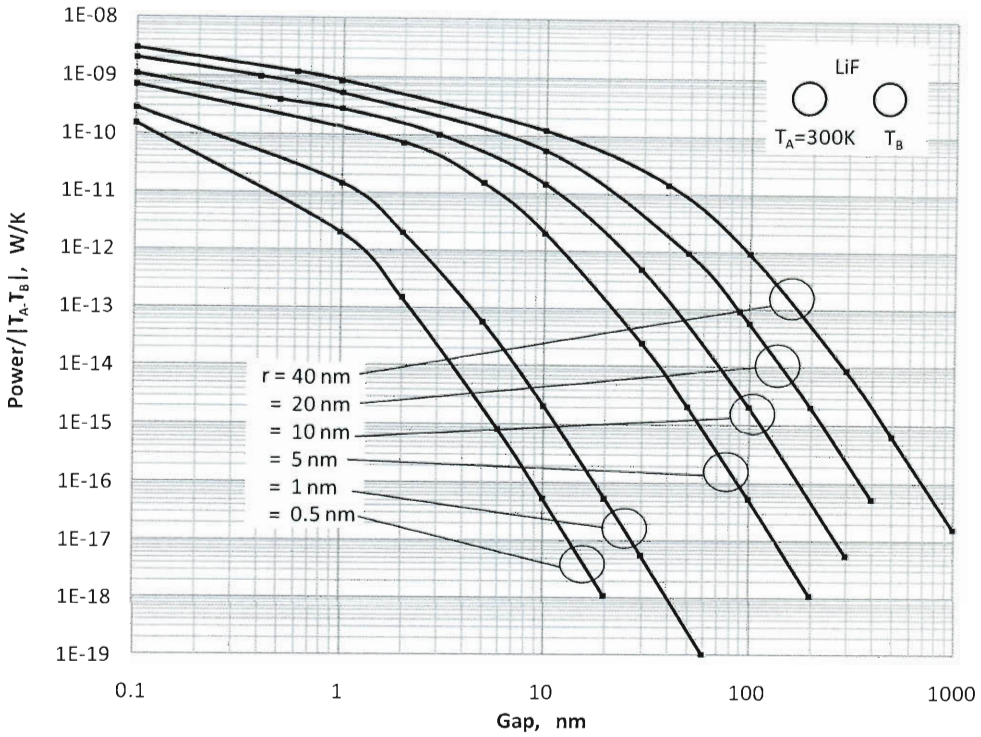

Figure 2.5: Sphere-to-Sphere Radiative Exchange: LiF, Equal Radii, Nanoscale

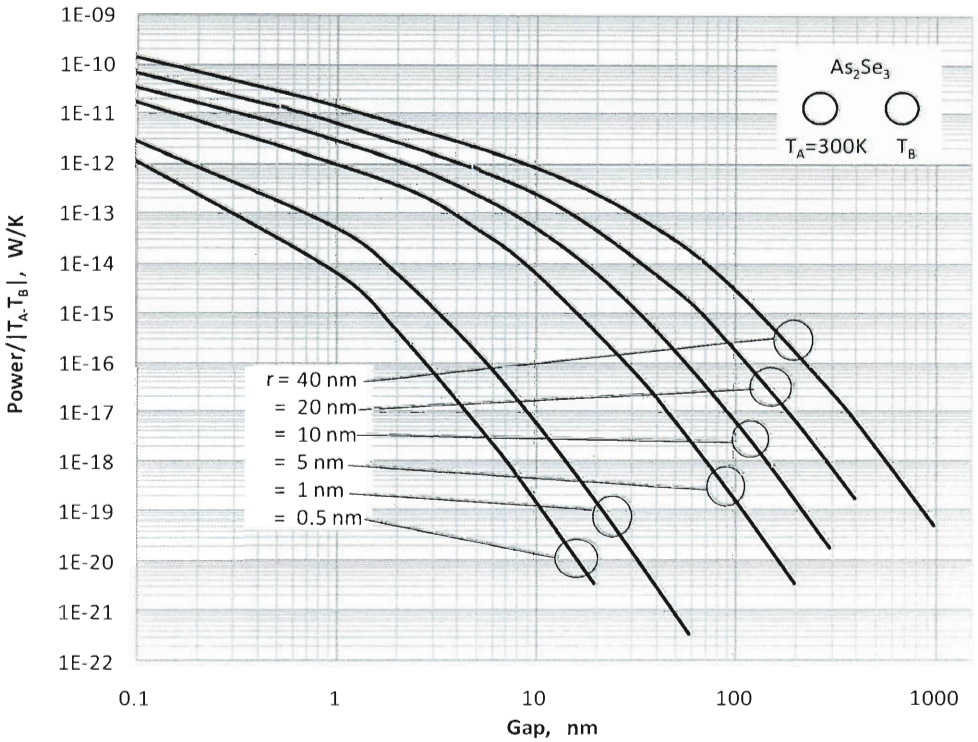

Figure 2.6: Sphere-to-Sphere Radiative Exchange: Arsenic Triselenide, Equal Radii, Nanoscale

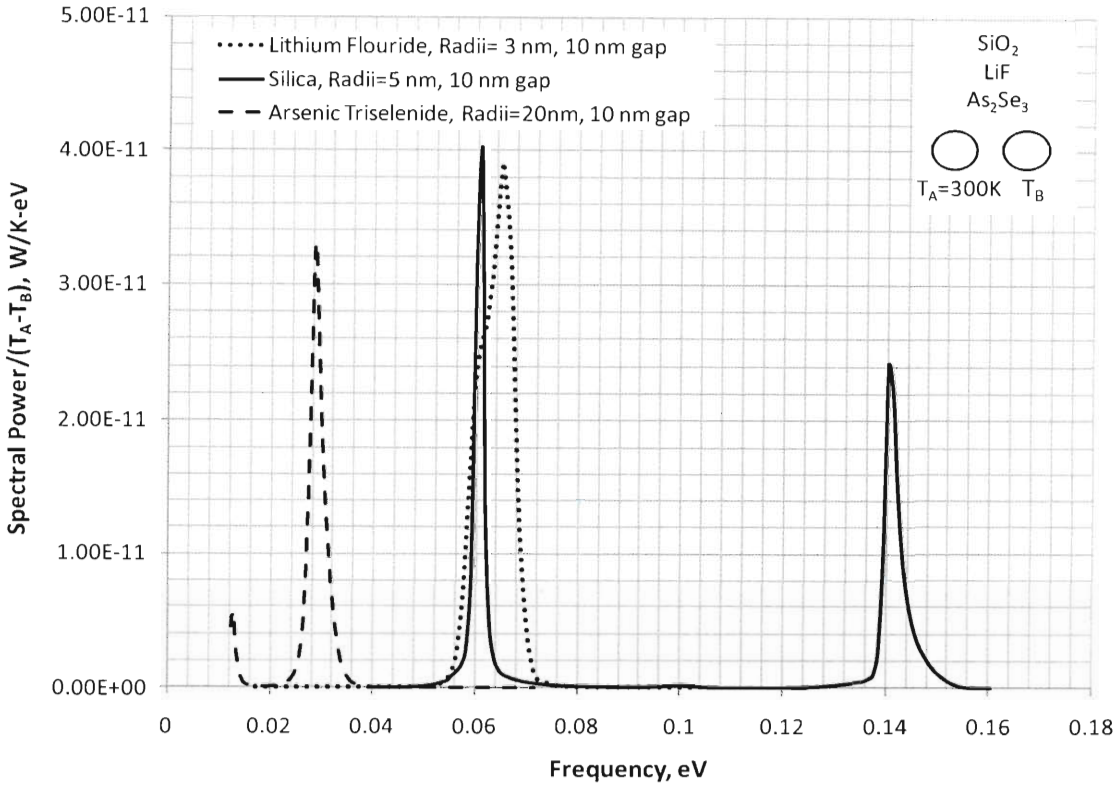

Figure 2.7: Sphere-to-Sphere Spectral Radiative Exchange: Various Materials, Equal Radii, Nanoscale

Physically, the variations amongst materials can be understood by looking at a selection of spectral data for these materials. The following figure shows the resonance regions that occur within the spectral radiative power exchanged. The cases for each material were chosen such that the peaks would be approximately between 3e-11 to 4e-11 for plotting purposes. Note that for a gap of 10 nm, the arsenic triselenide sphere radius must be 20 nm to yield a peak in this range. Since the resonant peak is much lower in arsenic triselenide for a given geometry compared with lithium fluoride and silica, it follows that the overall power will also be lower. Silica is unique in that it has two peaks. However, the width of the peak of the lithium fluoride is much thicker than silica, yielding a higher total power. In addition, the smaller sphere radii of 3 nm was required to plot the peak in the desired range, while silica required a radii of 5 nm.

These resonant regions correspond to the refractive index, specifically the imaginary component of the dielectric constant. Peaks occur within the dielectric constant at corresponding eV as the resonant peaks shown in the spectral plot.

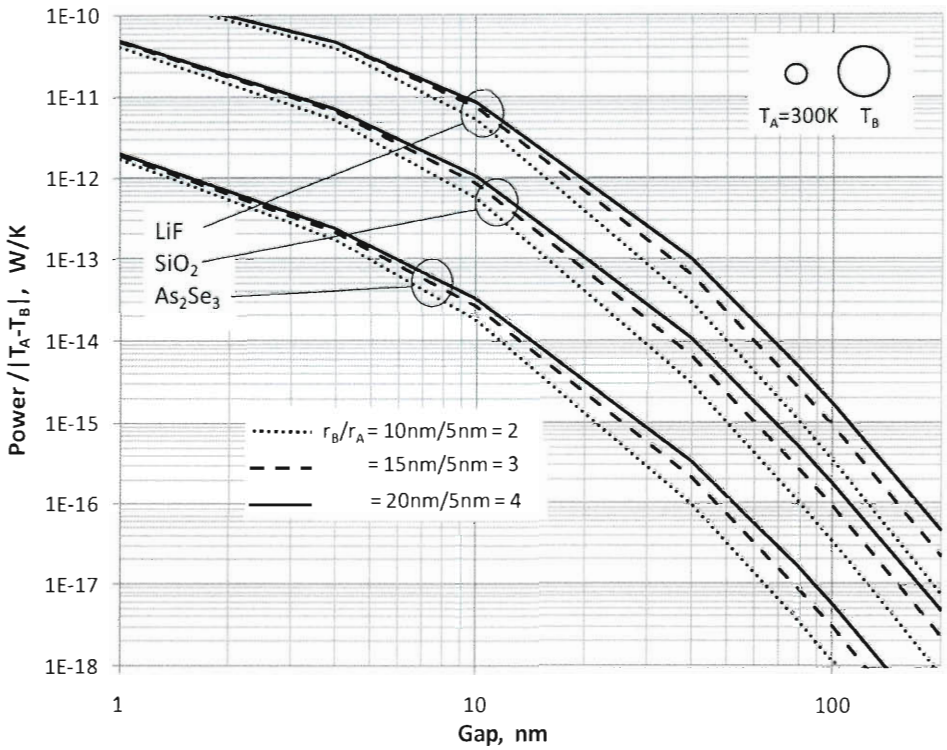

Figure 2.8: Sphere-to-Sphere Radiative Exchange: Varying Material, Varying Radii Ratio, Nanoscale

The results shown in Figure 2.8 depict the power over temperature difference calculated for two nanospheres of different radii at varying gap. These results are for the temperature case of T_A=300K. All three of the materials investigated are displayed. The higher degree of radiative exchange that exists in lithium flouride is observed in this graph when the values are compared to the same configurations of silica and arsenic triselenide nanospheres. Results ranged from 1e-18 to 1e-11 W/K.

To investigate the dependence of radiative exchange on radii ratio further, calculations were done for the same radii ratio but with different individual nanosphere radii. These results are presented in Figure 2.9. The radiative exchange is based on both radii of the spheres. There is a five-order of magnitude increase in the value for the exchange between 1 nm to 2 nm nanospheres and 10 nm to 20 nm nanospheres.

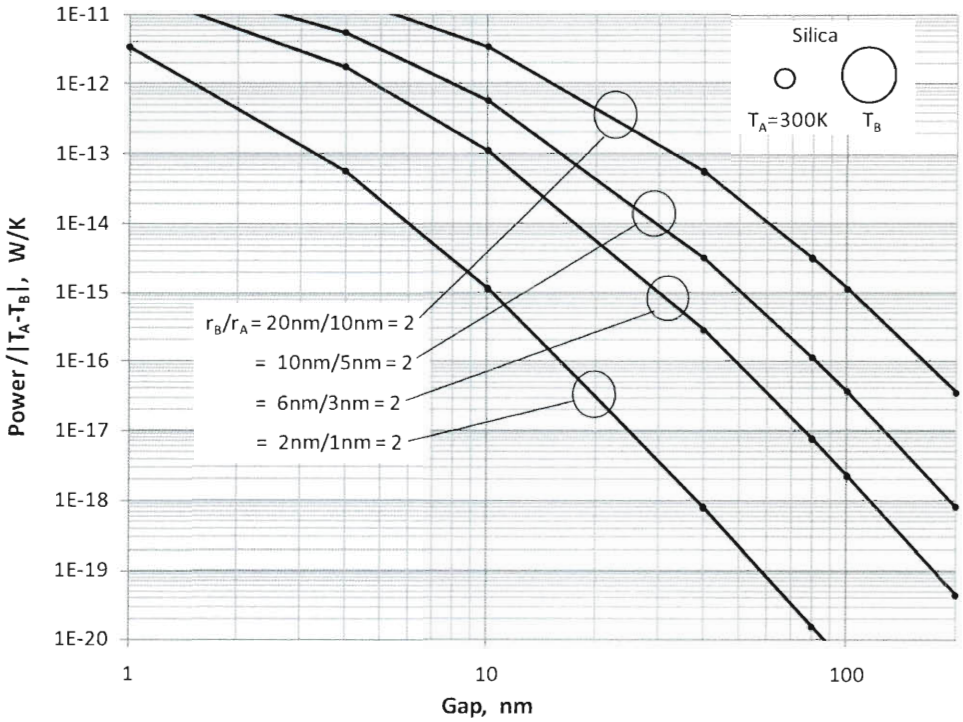

Figure 2.9: Sphere-to-Sphere Radiative Exchange: Silica, Radii Ratio=2, Nanoscale

2.4 Conclusions

An investigation of near-field radiative heat transfer was conducted. Two methods were calculated and then a comparison was plotted. The more complex method was utilized for accuracy. The author's results generated for silica sphere to silica sphere near-field transfer at the microscale agree with previously published data. Radii ratio, unequal spheres, and varied

temperature cases at the nanoscale were also examined. A new method for calculating sphere-to-plane radiative transfer was presented and results were shown to agree well with published theoretical and experimental data. The spectral radiative transfer was investigated to understand the material's thermal performance.

2.5 References

[1] Volz, S. (ed.), *Microscale and Nanoscale Heat Transfer*, Topics in Applied Physics Series, Springer Berlin, Heidelberg, 2006, Ch. 1, 4, 6.
doi: 10.1007/11767862

[2] Joulain, K., Mulet, J., Marquier, F., Carminati, R., and Greffet, J. J., "Surface Electromagnetic Waves Thermally Excited: Radiative Heat Transfer, Coherence Properties and Casimir Forces Revisted in the Near Field," *Surface Science Reports*, Vol. 57, No. 3-4, May 2005, pp. 59-112.
doi: 10.1016/j.surfrep.2004.12.002

[3] Zhang, Z., and Menguc, M.P., "Special Issue on Nano/Microscale Radiative Transfer," *J. Heat Transfer,* Vol. 129, No. 1, Jan. 2007, pp. 1-2.
doi: 10.1115/1.2401204

[4] Mulet, J., Joulain, K., Carminati, R., and Greffet, J., "Enhanced Radiative Heat Transfer at Nanometric Distances," *Nanoscale and Microscale Thermophysical Engineering*, Vol. 6, No. 3, July 2002, pp. 209-222.
doi: 10.1080/10893950290053321

[5] Narayanaswamy, A., and Chen, G., "Thermal Near-Field Radiative Transfer Between Two Spheres," *Phys. Rev B77,* Vol. 77, No. 7, 2008, pp. 1-12.
doi: 10.1103/PhyRevB.77.075125

[6] Narayanaswamy, A., Shen, S., and Chen, G., "Near-field Radiative Heat Transfer Between a Sphere and a Substrate," *Phys. Rev B78,* Vol. 78, No. 11, 2008, pp. 1-4.
doi: 10.1103/PhyRevB.78.115303

[7] Landau, L. D., and Lifshitz, E. M., *Statistical Physics*, 3rd ed., Part I, Reed Educational Publishing, Boston, 1985, pp 386-393.

[8] Rytov, S. M., "Theory of Electric Fluctuations and Thermal Radiation," U.S. Airforce Cambridge Research Lab., Rept. AD0226765, Bedford, MA, July 1959.

[9] Rytov, S. M., Kravtsov, Y. A., Tatarskii, V. I., *Principles of Statistical Radiophysics*, Vol. 3, Springer-Verlag, Berlin, 1989, pp 109-122.

[10] Chew, W. C., *Waves and Fields in Inhomogeneous Media,* IEEE Press, Piscataway, NJ, 1995, pp 15-16, 184-189, 375-428.
doi: 10.1163/156939393X00787

[11] Tsang, L., Kong, J.A., and Ding, K., *Scattering of Electromagnetic Waves: Theories and Application,* Wiley, Hoboken, NJ, 2000, pp 54-60.

[12] Tai, C., *Dyadic Green's Function in Electromagnetic Theory,* 2nd ed., IEEE Press, Piscataway, NJ, 1994.

[13] Korenev, B. G., *Bessel Functions and Their Applications,* CRC Press, Boca Raton, FL, 2002, pp. 17-19.

[14] Abramowitz, M. and Stegun, I. A. (Eds.), *Handbook of Mathematical Functions with Formulas, Graphs, and Mathematical Tables,* 9th ed., Dover, NY, 1972, pp. 435-478.

[15] Arfken, G., *Mathematical Methods for Physicists,* Academic Press, 3rd ed., Orlando, FL, 1985, pp. 633-634.

[16] Mackowski, D., and Mishchenko, M., "Prediction of Thermal Emission and Exchange Among Neighboring Wavelength-Sized Spheres," *Journal of Heat Transfer*, Vol. 130, 112702, November 2008, pp. 1-7.
doi: 10.1115/1.2957596

[17] Basu, S., Zhang, Z.M., and Fu, C.J., 2009, "Review of Near-Field Thermal Radiation and Its Application to Energy Conversion," *International Journal of Energy Research,* Vol. 33, pp. 1203-1232.

[18] Palik, E. D., *Handbook of Optical Constants of Solids,* Academic Press, New York, 1985, pp. 623-798.

Chapter 3

Nanorod Near-field Radiative Heat Exchange Analysis

3.1 Introduction

Near-field radiative exchange between two bodies has been the topic of recent study due to its energy conversion applications. Specifically, application related to nanomanufacturing, near-field thermal photovoltaic devices, and nanostructure imaging [1]. Near-field radiative transfer occurs when two bodies are at a separation distance that is equal or less than the radiative exchange's dominant wavelength. Given that the dominant wavelength is dependent on the temperature of the bodies, the near-field exchange is also temperature dependent. An investigation into this related to Wien's displacement law and observed deviations can be found in [2]. When the separation distance criterion is satisfied, radiation tunneling is supported resulting in near-field radiative energy transfer. Radiation tunneling is the process by which surface or evanescent waves are able to tunnel into a nearby body. At separation distances above the critical distance, the rapidly decaying evanescent waves are not able to tunnel into the nearby body to transfer energy in this manner. For more information about near-field radiative exchanged the reader is directed to [3-9].

In recent published works, near-field radiative exchange has been considered in a variety of different geometric configurations. Two semi-infinite bodies with a nanometric separation distance were investigated in [6]. Two planar surfaces and nanospheres treated as dipoles were analyzed in [3]. An array of studies has been produced for near-field exchange amongst spheres

beyond the initial dipole assumption. In [10] Narayanaswamy and Chen formulate a solution for radiative exchange between two nanospheres including a calculation for two silica microspheres of equal radii. An experimental assessment of this configuration was presented in [11]. This method was implemented for silica, lithium fluoride, and arsenic selenide nanospheres of equal and unequal radii in [12]. An asymptotic method for extending this formulation to a sphere-to-plane geometry is also given in [12]. An aggregate of spheres and dense nanoparticulate media was addressed in [13] and [14], respectively. A formulation of the solution to near-field radiative heat transfer in one dimensional layered media with an analysis of cubic boron nitride can be found in [15]. The topic of near-field thermal emissions within thin films was investigated in [16, 17]. A discussion of numerical methods associated with radiative transfer at the nanoscale is discussed in [18].

In this paper the procedure to calculate near-field radiative exchange presented by Narayanaswamy and Chen in [6] for sphere-to-sphere is modified and applied to a cylinder-to-cylinder geometry of nanorods. The fundamentals utilized for the spherical configuration are briefly covered in this work, with a detailed discussion of cylindrical geometry specific equations. Further details of the wave fields and scattering theory utilized in this work can be found in [19-20]. The fields are presented in forms that incorporate the Fluctuation Dissipation Theorem (FDT), Dyadic Green's Function (DGF), and Bessel Functions. Background on these mathematical tools can be found in [19-27]. The cylindrical addition theorem applied in the formulation of this work is described in [19, 28-29]. The procedure for calculating radiative exchange between the cylinder-to-cylinder geometry was extended to estimate a cylinder-to-plane geometric configuration utilizing a new asymptotic method. In this method, the cylinder-to-plane radiative exchange is approximated by holding the radius of one nanorod constant while

the radius of the neighboring nanorod is iteratively increased to approach a planar geometry. The radiative exchange is calculated after each iteration until the solution converges.

Based on [30], non-local optical response has traditionally been incorporated for particles at the nanoscale. A blue-shift of the resonance has been observed on these scales with an additional small secondary resonance excitation. Since the resonance magnitude does not change, but is simply shifted, the overall impact is not expected to alter the overall findings significantly. The smaller secondary excitations may impact the overall results, but given that they are much smaller when compared to the other resonance peaks, neglecting these is an acceptable first step. Non-local optical response impacts are left as future work.

3.2 Formulation

The methodology utilized in for the calculation of near-field radiative heat transfer between nanorods shares the framework established for sphere-to-sphere near-field radiative transfer framework given in [12]. Within this framework, modifications were made to make it applicable to a cylindrical geometry. An overview is given here of the fundamental governing equations in describing near-field radiative heat transfer between nanospheres. Following this, a discussion of the additional modifications required to adapt this configuration to apply to a cylindrical geometry is covered.

The spectral radiative exchange between nanorods is determined from the Poynting vector given in [10] as

$$\begin{aligned}&\left\langle E_{i\omega} H^{*}_{j\omega} \right\rangle \\ &= i\omega\mu_0 \int_V d^3r' \left\{ \overline{\overline{G_E}}(\vec{r}_1, \vec{r}, \omega) \overline{\overline{G_H}}^{*}(\vec{r}_1, \vec{r}', \omega) \left\langle \vec{J}_l(\vec{r}, \omega) \vec{J}^{*}_m(\vec{r}', \omega) \right\rangle \right\}\end{aligned} \tag{3.1}$$

where $\overline{\overline{G_E}}(\vec{r}_1,\vec{r},\omega)$ and $\overline{\overline{G_H}}(\vec{r}_1,\vec{r},\omega)$ are the DGFs due to a source at $\vec{r}$. Here the mathematical technique of kernels known as the Dyadic Green's Function which include second rand dyad tensors is utilized. Additional information on Dyadic Green's Function is found in [19-20, 24]. The integration is performed over the entire cylindrical volume containing the source. μ_0 is the permeability of vacuum given by $4\pi\times10^{-7}$ H/m and $\vec{J}(\vec{r},\omega)$ is the Fourier component of fluctuating current. To handle the fluctuating nature of the current, a statistical average, represented as <·,·>, is implemented. The * indicates the complex conjugate. The Cartesian components are denoted by the subscript i and j. This equation can be further developed by implementing the Fluctuation Dissipation Theorem (FDT) given by Rytov in [23]. The FDT indicates that the thermal fluctuations can be expressed as a density matrix in terms of the mean energy quantum oscillator, $\theta(\omega,T)$. This is expressed as:

$$\theta(\omega,T)=\hbar\omega\Big/\left(\exp\left(\hbar\omega/k_bT\right)-1\right). \tag{3.2}$$

The $\hbar$ is the Dirac constant given as 1.055×10^{-34} J·s. The angular frequency in rad/s is denoted by ω. k_b is Boltzmann's constant equivalent to 1.381×10^{-23} J/K. T is temperature in Kelvin. The form of the FDT equation utilized in this work is shown as follows from [21] as:

$$\left\langle \vec{J}_l(\vec{r},\omega)\vec{J}_m^{\,*}(\vec{r}',\omega)\right\rangle=\omega\varepsilon_0\varepsilon''(\omega)\theta(\omega,T)\delta_{lm}\delta(\vec{r}-\vec{r}') \tag{3.3}$$

where ε_0 is the permittivity of vacuum equivalent to 8.854×10^{-12} F/m, and ε'' is the imaginary part of the dielectric function which is unitless. The Kronecker delta function is denoted as δ_{lm} and the Dirac delta function as δ. The mean energy quantum oscillator is represented as $\theta(\omega,T)$. Incorporating the Fluctuation Dissipation Theorem, the following equation is written:

$$\left\langle E_i(\vec{r}_1,\omega)H_j^*(\vec{r}_1,\omega)\right\rangle = \frac{i\varepsilon_o\varepsilon''(\omega)\mu_0\omega^2\theta(\omega,T)}{\pi}\int_V d^3r\left\{\left(\overline{\overline{G_E}}(\vec{r}_1,\vec{r},\omega)\overline{\overline{G_H}}^*(\vec{r}_1,\vec{r}',\omega)\right)_{ij}\right\} \tag{3.4}$$

The Fourier components of the fluctuating fields given by [24] are written as:

$$\vec{E}(\vec{r}_1,\omega) = i\omega\mu_0\int_V \overline{\overline{G_E}}(\vec{r}_1,\vec{r},\omega)\cdot\vec{J}(\vec{r},\omega)d^3r \tag{3.5}$$

$$\vec{H}(\vec{r}_1,\omega) = \int_V \overline{\overline{G_H}}(\vec{r}_1,\vec{r},\omega)\cdot\vec{J}(\vec{r},\omega)d^3r \tag{3.6}$$

where $\overline{\overline{G_E}}(\vec{r}_1,\vec{r},\omega)$ and $\overline{\overline{G_H}}(\vec{r}_1,\vec{r},\omega)$ are the DGFs due to a source at $\vec{r}$. Additional details can be found in [10].

The background of this formulation can be understood by taking a look back to its relationship to fundamental vector wave equations. The vector wave solution is written as follows:

$$\nabla\times\nabla\times\boldsymbol{E}(\boldsymbol{r}) - \omega^2\mu\varepsilon(\boldsymbol{E}(\boldsymbol{r})) = 0. \tag{3.7}$$

where E is the electric field, ε is the permittivity, μ is the permeability, and ω is the angular frequency. The vector wave solution is derived from the general wave equation. The general wave solution is written as follows:

$$\psi_{m,n} = j_n(kr)L_n^m(\cos\theta)h(m\phi). \tag{3.8}$$

It is composed of Legendre polynomials, $L_n^m(\cos\theta)$, spherical Bessel functions $j_n(kr)$, and time harmonic functions, $h(m\phi)$. Bessel functions are critical in the overall process of calculating the radiative exchange and will be dealt with later in greater detail. The general wave equation can

be handled in any coordinates of interest: rectangular, spherical, or cylindrical coordinates. In this case, based on the geometry of interest, spherical coordinates are utilized. The general wave equation is solved from the Helmholtz equation. The Helmholtz equation is

$$\left(\nabla^2 + k^2\right)\boldsymbol{E}(\boldsymbol{r}) = 0. \tag{3.9}$$

Here, ∇^2 is the Laplacian and k is the wave propagation vector. A special case of the Helmholtz equation is the Laplace equation, whose solutions are known as spherical harmonics. The scalar version of the Helmholtz equation is written as

$$\left(\nabla^2 + k^2\right)\psi(\boldsymbol{r}) = 0. \tag{3.10}$$

where $\psi(\boldsymbol{r})$ is the scalar potential and k is the wave propagation vector. The Helmholtz equation is derived directly from the Maxwell's equations, which describe the electromagnetic fields associated with the nanospheres.

Now that we have an idea of origination of the vector wave solution, we begin solving our problem by mathematically constructing it. In depth information on this process is given in [18] and [19]. The vector wave solution consists of three types of waves: M waves, N waves, and L waves. The L waves are based on a gradient operator and written as:

$$\boldsymbol{L}_{nm}(k, \boldsymbol{r}) = \frac{1}{k}\nabla\psi_{nm}(k, \boldsymbol{r}) \tag{3.11}$$

L waves are translationally invariant and therefore of little interest for our purpose by which one object is a translation of the other. The M and N waves are the crux of what we will need for the vector wave equation. M waves are characterized as

$$\boldsymbol{M}_{nm}(k,\boldsymbol{r}) = \nabla \times c\psi_{nm}(\boldsymbol{r}) \tag{3.12}$$

where $\boldsymbol{c}$ is known as the pilot vector. The N waves are expressed as:

$$\boldsymbol{N}_{nm}(k,\boldsymbol{r}) = \frac{1}{k}\nabla \times \boldsymbol{M}(k,\boldsymbol{r}) = \frac{1}{k}\nabla \times \nabla \times c\psi_{nm}(\boldsymbol{r}). \tag{3.13}$$

There are similarities between these two equations, though the final equations to represent them are different. Both M and N waves are based on the curl operator. The M waves can be thought of as representing the transverse electric field, while the N wave is associated with the transverse magnetic field. The forms of these equations are quite different for spherical, rectangular, and cylindrical coordinate systems. The spherical system is unique in that the M and N waves are decoupled, for homogeneous and isotropic media.

Both M and N waves are incident standing waves that hit the spherical boundary from the outside. Each M and N waves produce a reflected wave and transmitted wave. These are governed by the transmitted wave formula and reflected wave formula. The formulas governing these waves are different for the M and N waves. In the following formulas, the wave is considered to impinge at the spherical boundary. The subscripts 1 indicate the region inside the spherical boundary, and the subscripts 2 represent the region outside the spherical boundary. The reflected wave formula for M waves is expressed as:

$$R_c^M = \frac{\sqrt{\varepsilon_1\mu_2}\,\hat{j}_n(k_2a)\hat{j}_n'(k_1a) - \sqrt{\varepsilon_2\mu_1}\,\hat{j}_n(k_1a)\hat{j}_n'(k_2a)}{\sqrt{\varepsilon_2\mu_1}\,\hat{j}_n(k_1a)\hat{h}_n'^{(1)}(k_2a) - \sqrt{\varepsilon_1\mu_2}\,\hat{h}_n^{(1)}(k_2a)\hat{j}_n'(k_1a)} \tag{3.14}$$

while the transmitted wave formula is

$$T_c^M = \frac{i\mu_1\sqrt{\frac{\varepsilon_1}{\mu_1}}}{\sqrt{\varepsilon_2\mu_1}\hat{j}_n(k_1a)\hat{h}_n'^{(1)}(k_2a) - \sqrt{\varepsilon_1\mu_2}\hat{h}_n^{(1)}(k_2a)\hat{j}_n'(k_1a)}. \tag{3.15}$$

For N waves the reflected wave formula is described as

$$R_c^N = \frac{\sqrt{\varepsilon_2\mu_1}\hat{j}_n(k_2a)\hat{j}_n'(k_1a) - \sqrt{\varepsilon_1\mu_2}\hat{j}_n(k_1a)\hat{j}_n'(k_2a)}{\sqrt{\varepsilon_1\mu_2}\hat{j}_n(k_1a)\hat{h}_n'^{(1)}(k_2a) - \sqrt{\varepsilon_2\mu_1}\hat{h}_n^{(1)}(k_2a)\hat{j}_n'(k_1a)} \tag{3.16}$$

and the transmitted waves as

$$T_c^N = \frac{i\varepsilon_1\sqrt{\frac{\mu_1}{\varepsilon_2}}}{\sqrt{\varepsilon_1\mu_2}\hat{j}_n(k_1a)\hat{h}_n'^{(1)}(k_2a) - \sqrt{\varepsilon_2\mu_1}\hat{h}_n^{(1)}(k_2a)\hat{j}_n'(k_1a)}. \tag{3.17}$$

where ε is the permittivity and μ is the permeability. Both M and N waves are written in terms of spherical Bessel and related functions. The types utilized include first order, second order, Hankel, and derivative spherical Bessel functions. Spherical Bessel functions of the first kind are expressed as:

$$j_n(x) \equiv \sqrt{\frac{\pi}{2x}} J_{n+\frac{1}{2}}(x). \tag{3.18}$$

The spherical Bessel functions of the 2nd kind are given as:

$$y_n(x) \equiv \sqrt{\frac{\pi}{2x}} Y_{n+\frac{1}{2}}(x) \tag{3.19}$$

$J_n(x)$ is a general Bessel function of the first kind and $Y_n(x)$ is a general Bessel function of the second kind. The Hankel function is composed of first and second order Bessel functions. The Hankel function is expressed as:

$$h_n(x) = j_n(x) + iy_n(x) \tag{3.20}$$

Additional useful relationships describing a function derived from the Bessel functions are known as the recurrence relations:

$$j_n'(x) = j_{n-1}(x) - \frac{n}{x} j_n(x) \tag{3.21}$$

and

$$y_n'(x) = y_{n-1}(x) - \frac{n}{x} y_n(x). \tag{3.22}$$

See [19, 26-27] for additional information regarding these functions.

Once the vector wave solution has been written for the coordinate system of each unit sphere, the overall vector wave solution must be calculated by combing these solutions. This is done via the spherical vector translation addition theorem expressed as

$$M_{nm}(\boldsymbol{r}) = \sum_{\nu=1}^{\nu} \sum_{\mu=-\nu} \left[M_{\nu\mu}(\boldsymbol{r}') A_{\nu\mu,nm} + N_{\nu\mu}(\boldsymbol{r}') B_{\nu\mu,nm} \right]. \tag{3.23}$$

Where $\boldsymbol{r} = \boldsymbol{r}' + \boldsymbol{r}''$ is shown below and represents the center of each sphere:

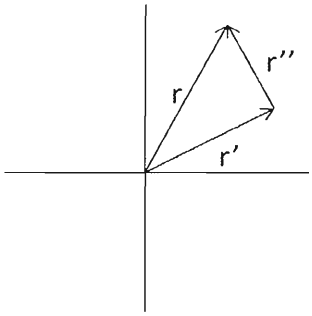

Figure 3.1: Geometric representation of r vector

The above equation enables the vector spherical M waves to be calculated for the second sphere, by combing the vector spherical M and N waves from the sphere at the first location.

The implementation of these equations for the case of cylindrical nanorods could not be done in the same manner as what was presented in [12] for nanospheres. There were modifications that were required before this process could be applied to the cylindrical geometry that occurs in nanorods. The original process described in the near-field radiative transfer for nanospheres utilized spherical vector waves with spherical Bessel functions. These no longer apply. Instead, cylindrical vector waves with cylindrical Bessel functions were substituted. Cylindrical vector wave functions are written as:

$$\bar{M}_n\left(k_p, k_z, \bar{r}\right) = \nabla \times \hat{z} J_n\left(k_p \rho\right) e^{ik_z z + in\phi} \tag{3.24}$$

and

$$\bar{N}_n\left(k_p, k_z, \bar{r}\right) = \frac{1}{k} \nabla \times \bar{M}_n\left(k_p, k_z, \bar{r}\right) \tag{3.25}$$

where

$$k_\rho^2 + k_z^2 = k^2 \tag{3.26}$$

The wave propagation vector is represented by k. The subscript ρ refers to the coordinates in the radial direction of the cylinder. The subscript z refers to the coordinates in the lengthwise direction of the cylinder. For further details, see [19]. Cylindrical Bessel functions are related to spherical Bessel functions as follows:

$$J_n(x) = \sqrt{\frac{2x}{\pi}} j_{n-1/2}(x)) \tag{3.27}$$

where *J(x)* represents a cylindrical Bessel function of the first kind, and *j(x)* represents a spherical Bessel function of the first kind. The relationship between spherical and cylindrical Bessel functions of the 2nd kind are similarly given as

$$Y_n(x) = \sqrt{\frac{2x}{\pi}} y_{n-1/2}(x)) \tag{3.28}$$

where *Y(x)* represents a cylindrical Bessel function of the second kind, and y*(x)* represents a spherical Bessel function of the second kind. Additional details of Bessel functions can be found in Ref [25-27].

The M and N waves described above are the transverse magnetic and transverse electric waves, respectively. The cylindrical geometry differs from the spherical geometry in that these waves do not decouple. To deal with this difference, instead of using scalar reflective coefficients for each wave type as done in the spherical configuration, a reflective matrix is used containing coefficients for both the transverse electric and transverse magnetic field waves. The reflection coefficient matrix is given in [19]:

$$\overline{\boldsymbol{R}} = \overline{\boldsymbol{D}}^{-1} \cdot \left[J_n^{(1)}(k_{1\rho}a) \overline{\boldsymbol{J}}_n^{(1)}(k_{2\rho}a) - J_n^{(1)}(k_{2\rho}a) \overline{\boldsymbol{J}}_n^{(1)}(k_{1\rho}a) \right] \tag{3.29}$$

In the above equation, the following relationships hold true:

$$\overline{\boldsymbol{D}} = \left[\boldsymbol{J}_n\left(k_{1\rho}a\right)H_n^{(1)}\left(k_{2\rho}a\right) - \overline{\boldsymbol{H}}_n^{(1)}\left(k_{2\rho}a\right)J_n\left(k_{1\rho}a\right)\right] \tag{3.30}$$

and

$$\overline{\boldsymbol{B}}_n\left(k_{i\rho}\rho\right) = \frac{1}{k_{i\rho}^2\rho}\begin{bmatrix} i\omega\varepsilon_i k_{i\rho}\rho B_n'\left(k_{i\rho}\rho\right) & -nk_z B_n\left(k_{i\rho}\rho\right) \\ -nk_z B_n\left(k_{i\rho}\rho\right) & -i\omega\mu_i k_{i\rho}\rho B_n'\left(k_{i\rho}\rho\right) \end{bmatrix} \tag{3.31}$$

where B_n is $H_n^{(1)}$ for $\overline{\boldsymbol{H}}_n^{(1)}$ and J_n for $\overline{\boldsymbol{J}}_n$.

Wave equations in the coordinate system of one geometric object can be written in terms of the coordinate system of the second geometric object by applying the vector wave addition theorem. The spherical vector wave addition theorem no longer applies since the equation corresponds to the coordinate system of interest. The cylindrical vector addition theorem utilized instead is:

$$H_m^{(1)}\left(k_p\left|\bar{\rho} - \bar{\rho}'\right|\right)e^{im\phi''} = \sum_{n=-\infty}^{\infty} H_{n-m}^{(1)}\left(k_p\rho'\right)J_n\left(k_p\rho\right)e^{in\phi - i(n-m)\phi'} \tag{3.32}$$

See Ref [19, 28-29] for further details regarding the cylindrical vector addition theorem.

3.3 Results

Radiative exchange calculations for nanorods with varying radii to length aspect ratios were analyzed. These graphs include both the effects of near-field and far-field exchange. To gain an overall understanding the impact of near-field radiative transfer, the data is first plotted vs. gap for the case of two silica nanorods with length to diameter ratio of 5 to 1 for nanorod radii of 2, 4, 6, and 8 nm. This is shown in Figure 3.2. Properties of silica were taken from [31]. Here the

exponential nature of the near-field radiative heat transfer is seen in the increase of the radiative power transfer as the gap between the nanorods decreases. This exponential increase would not occur without the presence of near-field radiative heat transfer.

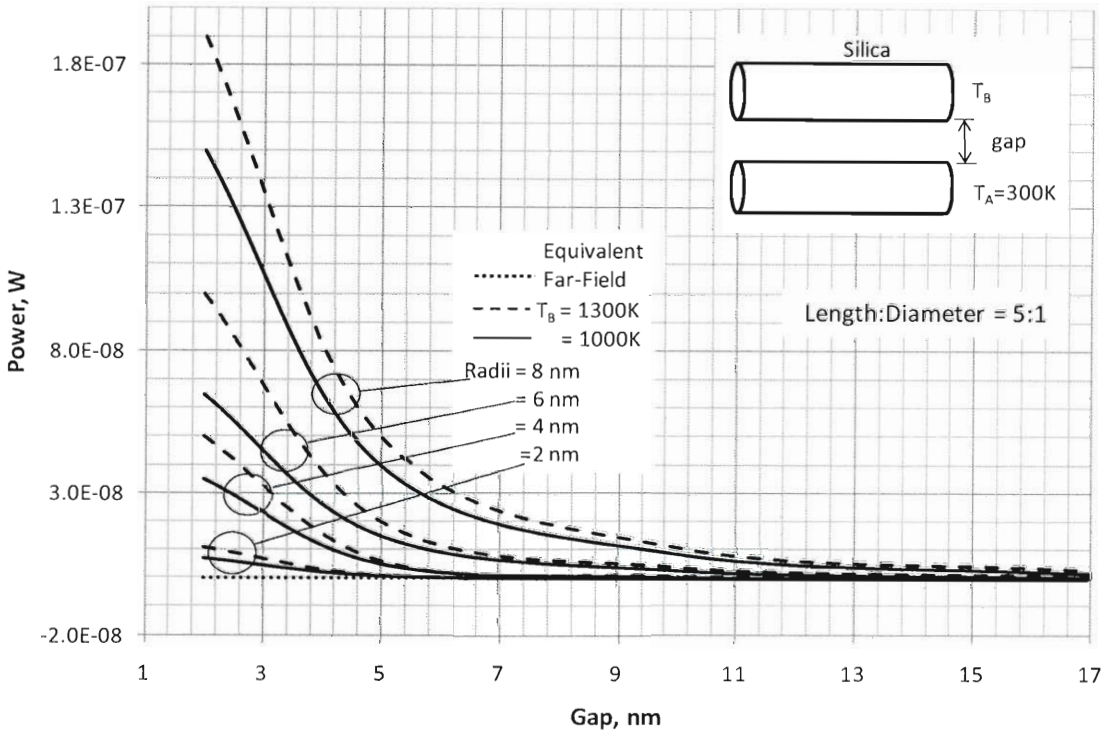

Figure 3.2: Nanorod-to-Nanorod Radiative Exchange vs. Gap : Silica, Equal Radii, Length: Diameter = 5:1

The equivalent far-field radiation line that does not contain the near-field radiation is also plotted on this graph. To gain an understanding of the behavior of the radiative heat transfer, we will isolate one case, namely 6nm at 1000K. By removing all of the other cases, plotting the y-axis on a logarithmic scale, and zooming in around its values, we can acquire a clearer picture of the equivalent far-field radiation vs. that which includes near-field. Figure 3.3 shows this result.

Note that as gap increases, the view factor between the two cylinders decreases. A decrease in view factor accounts for the decrease in far-field radiation transfer.

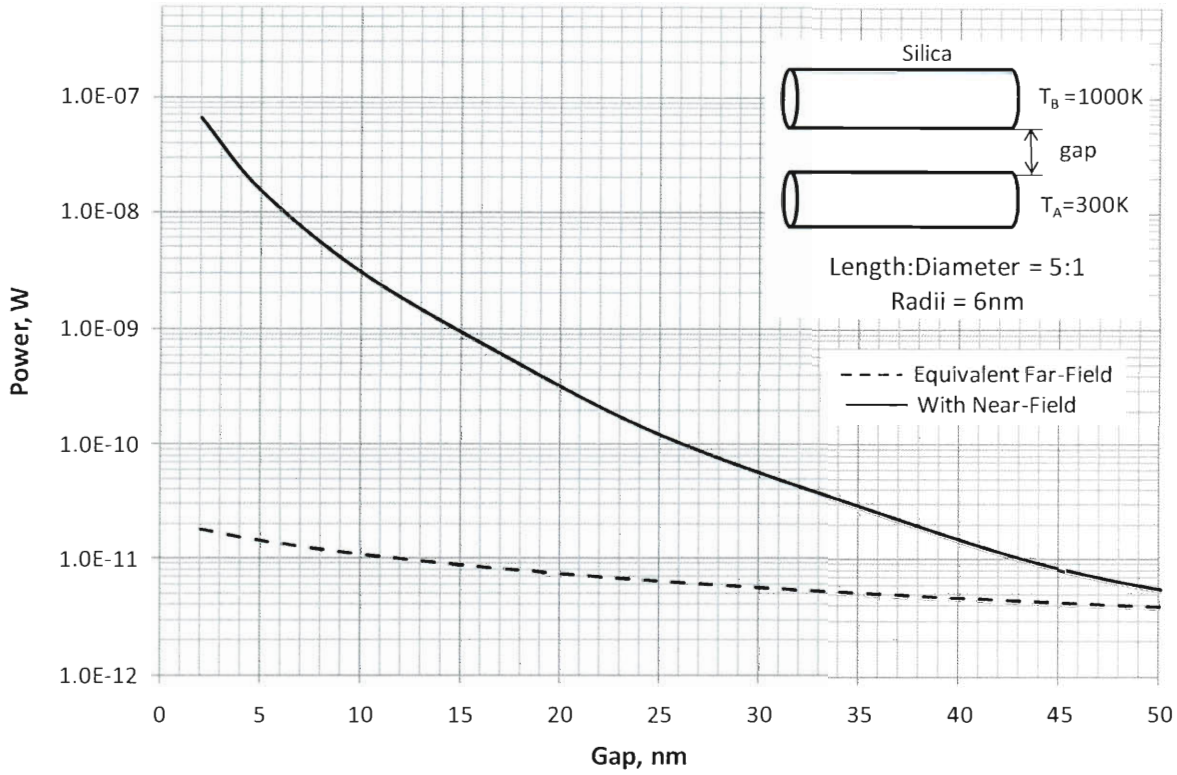

Figure 3.3: Nanorod-to-Nanorod Radiative Exchange vs. Gap : Silica, Length:Diameter = 5:1, Radii = 6nm

From Figure 3.3, the impact of the near-field transfer is evident. The cylindrical case is unique from the spherical case that has been discussed in Chapter 2, in that the near field transfer is magnified due to the larger geometric surface area for evanescent waves tunneling to be able to occur. This can be understood in the following graph. A unit sphere approximation in which the nanorod rigorous method is compared to a similar spherical configuration of five spheres placed side by side as shown in Figure 3.4. These results are shown in Figure 3.5. The rigorous

cylindrical method is computationally expensive and complex compared to the unit sphere approximation method. The unit sphere approximation can be used in situations where due to time or computational resource constraints it is not feasible to use the rigorous cylindrical method. Additional details of the unit sphere approximation method are covered in Chapter 4.

Figure 3.4: (a) Rigorous nanorod configuration vs. (b) side by side unit sphere approximation

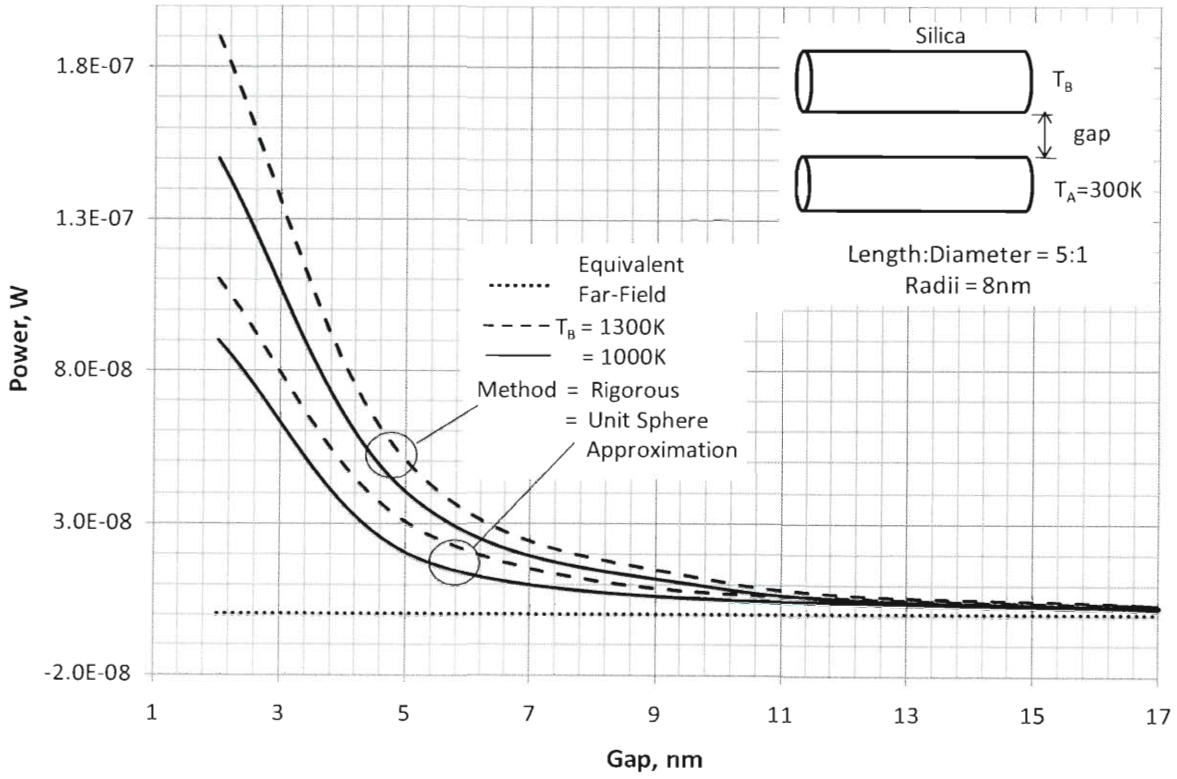

Figure 3.5: Nanorod-to-Nanorod Radiative Exchange vs. Gap: Silica, Equal Radii, Length: Diameter = 5:1.

The results that follow represent the radiative exchange versus nanorod radii between two same size silica nanorods plotted vs. nanorod radii. The range of nanorod radii is 10 nm down to 0.5 nm. The temperatures included are for the cases of T_A=1300K, 1000K, and 800K. Gaps investigated are 2nm, 5nm, and 10 nm. Figure 3.6 and 3.7 show the results for nanorods with a length: diameter ratios of 3:1 and 7:1 respectively. The same trend occurred in these plots with only a slight increase as the length to diameter ratio increased. The difference lies in the same order of magnitude.

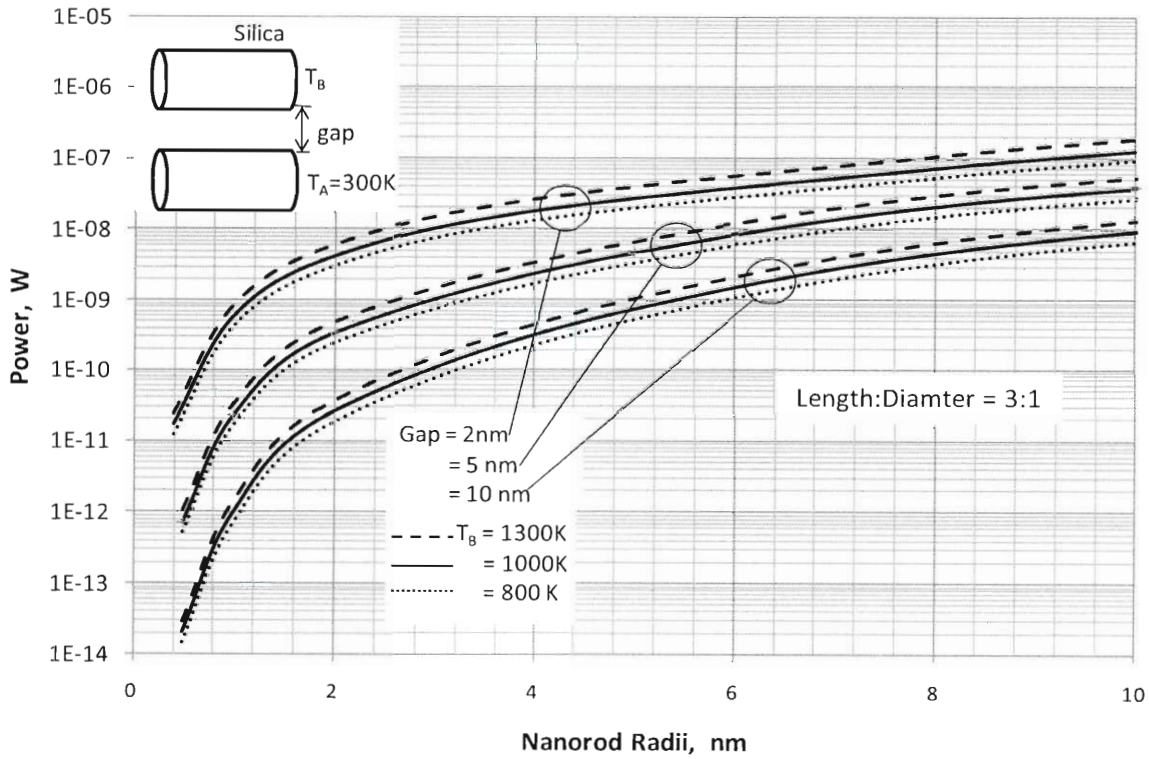

Figure 3.6: Nanorod-to-Nanorod Radiative Exchange: Silica, Equal Radii, Length: Diameter = 3:1

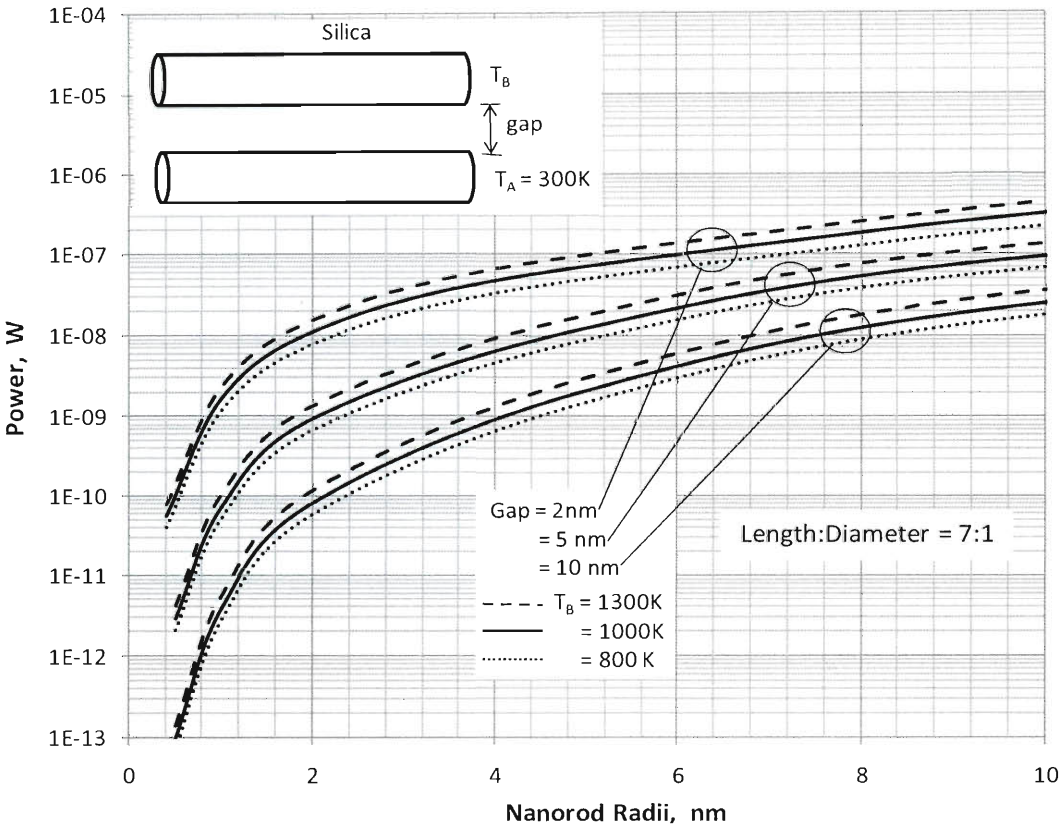

Figure 3.7: Nanorod-to-Nanorod Radiative Exchange: Silica, Equal Radii, Length:Diameter = 7:1.

The radiative exchange between a nanorod and a planar substrate are shown in Figure 3.8. Data is shown for nanorods with radii in the range of 0.5 nm to 10nm with gaps of 2 nm, 5 nm, and 10 nm. The length to radius radio for each nanorod is 5:1. The results generated were acquired by beginning with two nanorods with the same radii. One sphere was slowly increased and the radiative exchange recalculated until convergence. Convergence was defined as $\frac{x_2 - x_1}{x_1} < 0.05$ where x_1 and x_2 represent two subsequent calculated results. For the cases tested, gap influenced the time it took for the results to be acquired, but did not have a significant effect on when convergence was achieved.

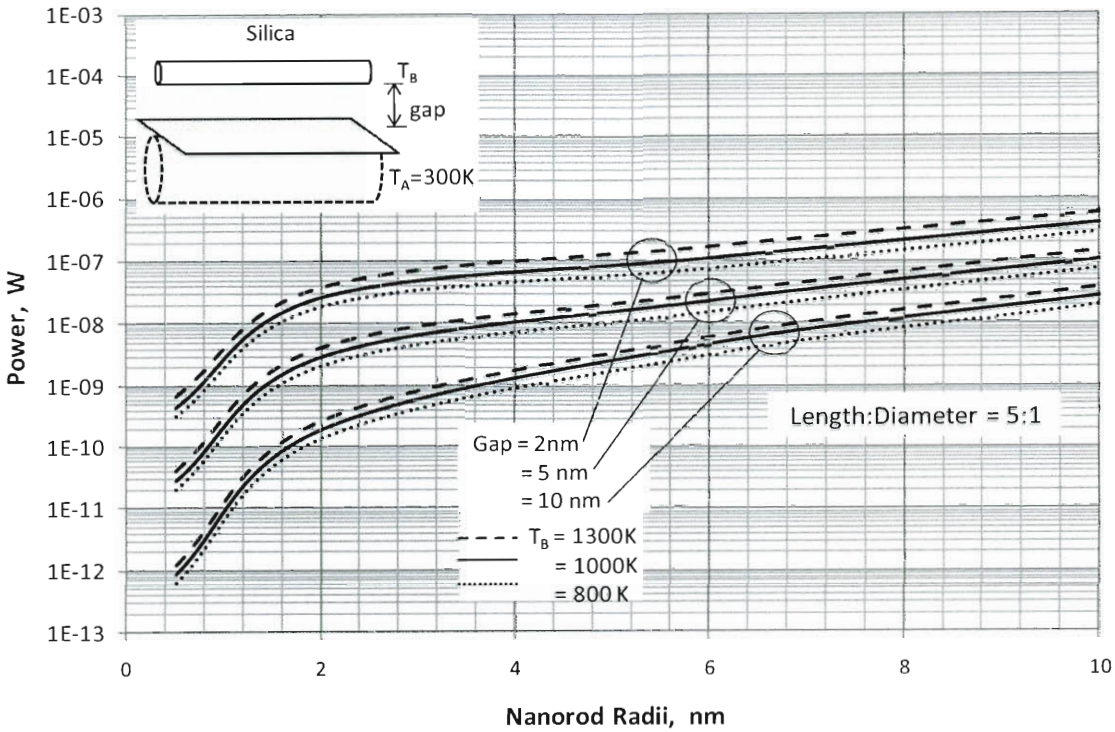

Figure 3.8 Cylinder to Plane Radiative Exchange

3.4 Conclusions

An investigation of near-field radiative heat transfer was conducted. A solution for radiative exchange between nanorods was formulated. The method was then applied to silica nanorods. Different length to diameter nanorod configurations were addressed. The near-field heat exchange impact is observed in a plot of power vs. decreasing gap with a closer look at the near-field vs. equivalent far-field radiation results comparison. Plots for energy versus nanorod radii were produced for varying gap and ratio. A new method for calculating nanorod-to-plane radiative transfer was presented and results were shown.

3.5 References

[1] Basu S, Zhang ZM, Fu CJ. Review of Near-Field Thermal Radiation and Its Application to Energy Conversion. Int J Energy Res. 2009; 33:1203-1232.

[2] Francoeur M, Menguc MP. Role of Fluctuational Electrodynamics in Near-Field Radiative Heat Transfer. J Quant Spectrosc & Radiat Transfer . 2008; 109(2): 280-293.

[3] Volz S, editor. Microscale and Nanoscale Heat Transfer. Topics in Applied Physics Series. Berlin: Springer; 2006. Ch. 1, 4, 6.

[4] Joulain K, Mulet J, Marquier F, Carminati R, Greffet JJ, Surface Electromagnetic Waves Thermally Excited: Radiative Heat Transfer, Coherence Properties and Casimir Forces Revisited in the Near Field. Surf Sci Rep. 2005; 57:59-112.

[5] Zhang Z, Menguc MP. Special Issue on Nano/Microscale Radiative Transfer. J Heat Transfer. 2007; 129(1):1-2.

[6] Mulet J, Joulain K, Carminati R, Greffet J, Enhanced Radiative Heat Transfer at Nanometric Distances. Nanoscale and Microscale Thermophysical Engineering. 2002; 6(3): 209-22.

[7] Zhang Z. Nano/Microscale Heat Transfer. New York: McGraw Hill; 2007. Ch. 10.

[8] Chen G. Nanoscale Energy Transport and Conversion: A Parallel Treatment of Electrons, Molecules, Phonons, and Photons. New York: Oxford University Press; 2005. Ch. 5.

[9] Carey VP, Chen G, Grigoropoulos C, Kaviany M, Majumdar A. A Review of Heat Transfer Physics. Nanoscale and Microscale Thermophysical Engineering. 2008; 12(1):1-60.

[10] Narayanaswamy A, Chen G. Thermal Near-Field Radiative Transfer Between Two Spheres. Phys Rev B77. 2008; 77(7): 1-12.

[11] Narayanaswamy A, Shen S, Chen G. Near-field Radiative Heat Transfer Between a Sphere and a Substrate. Phys Rev B78. 2008; 78(11):1-4.

[12] Carrillo LC, Bayazitoglu Y. Nanosphere Near-field Radiative Heat Exchange Analysis. AIAA J Thermophys Heat Transfer. 2010; 24(2): 309-315.

[13] Mackowski D, Mishchenko M. Prediction of Thermal Emission and Exchange Among Neighboring Wavelength-Sized Spheres. J Heat Transfer. 2008; 130:1-7.

[14] Prasher R. Thermal Radiation in Dense Nano- and Mircoparticulate Media. J Appl Phys. 2007; 102(7):1-9.

[15] Francoeur M, Menguc MP, Vaillon R. Solution of Near-Field Thermal Radiation in One-Dimensional Layered Media Using Dyadic Green's Function and the Scattering Matrix Method. J Quant Spectrosc & Radiat Transfer. 2009; 110(18): 2002-8.

[16] Francoeur M, Menguc MP, Vaillon R. Local Density of Electromagnetic States within a Nanometric Gap Formed Between Two Thin Films Supporting Surface Phonon Polaritons. J Appl Phys. 2010; 107(3):034313-034313-8.

[17] Francoeur M, Menguc MP, Vaillon R. Spectral Tuning of Near-Field Radiative Flux Between Two Thin Silicon Carbide Films. J Phys D: Appl Phys. 2010; 43(7):075501-075501-12.

[18] Wong B, Menguc MP. A Unified Monte Carlo Treatment of the Transport of Electromagnetic Energy, Electrons, and Phonons in Absorbing and Scattering Media. J Quant Spectrosc & Radiat Transfer. 2010; 111(3):399-419.

[19] Chew WC. Waves and Fields in Inhomogeneous Media. Piscataway: IEEE Press; 1995. p. 15-16, 184-189, 375-428.

[20] Tsang L, Kong JA, Ding K. Scattering of Electromagnetic Waves: Theories and Application. Hoboken: Wiley; 2000. p. 54-60.

[21] Landau LD, Lifshitz EM. Statistical Physics. 3rd ed. Part I. Boston: Reed Educational Publishing; 1985. p. 386-393.

[22] Rytov SM. Theory of Electric Fluctuations and Thermal Radiation. Bedford: U.S. Airforce Cambridge Research Lab; 1959.

[23] Rytov SM, Kravtsov YA, Tatarskii VI. Principles of Statistical Radiophysics. Vol 3. Berlin: Springer-Verlag; 1989. p. 109-22.

[24] Tai C. Dyadic Green's Function in Electromagnetic Theory. 2nd ed. Piscataway: IEEE Press; 1994.

[25] Korenev BG. Bessel Functions and Their Applications. Boca Raton: CRC Press; 2002. p. 17-9.

[26] Abramowitz M, Stegun IA, editors. Handbook of Mathematical Functions with Formulas, Graphs, and Mathematical Tables. 9th ed. New York: Dover; 1972. p. 435-78.

[27] Arfken G. Mathematical Methods for Physicists. 3rd ed. Orlando: Academic Press; 1985. p. 633-4.

[28] Chremmos ID, Uzunoglu NK. Transformation of Radially Traveling Cylindrical Waves Between Two Skew Cylindrical Coordinate System. J Opt Soc Am A. 2006; 23(8):1884-8.

[29] Chremmos I. Analytical Computation of the Electromagnetic Field Produced by an Optical Fiber Helix. Prog Electromag Res B. 2009; 16:189-207.

[30] Yannopapas, V. Non-local Optical Response of Two-Dimensional Arrays of Metallic Nanoparticles. J Phys: Condens. Matter 2008; 20: 325211.

[31] Palik ED. Handbook of Optical Constants of Solids. New York: Academic Press; 1985. p. 623-798.

Chapter 4

Near-field Radiative Heat Exchange by Nanosphere Approximation

4.1 Introduction

When two bodies are spaced at a distance that is less than or equal to the radiative exchange's dominant wavelength, the radiative exchange expected from the classical far-field heat transfer equations is exceeded due to the contribution of a phenomena known as near-field radiative transfer. A near-field radiative exchange that is impacted by temperature emerges. This is because the near-field exchange is dependent on the dominant wavelength. By Wien's displacement law, the dominant wavelength of the radiative exchange is a function of temperature. Physically, the near-field exchange is caused by surface or evanescent waves tunneling from one body to the other. Beyond the critical separation distance between the bodies, this additional energy transfer from radiation tunneling does not occur since the rapidly decaying evanenscent waves decay before reaching the neighboring body. The occurrence of near-field radiative transfer to enhance energy conversion applications between two bodies has been investigated for nanomanufacturing, near-field photovoltaic devices, and nanostructure imaging in [1]. For more information about near-field radiative exchange the reader is directed to [2-8].

There has been recent works discussing radiative heat exchange between bodies in difference configuration. Semi-infinite bodies and planar surfaces are discussed in [5] and [2]. Thin films and near-field thermal emissions has been analyzed in [9,10]. A formulation of near-field radiative exchange in one dimensional layered media of cubic boron nitride is given in [11]. In

[2], near-field transfer between microspheres utilizing a dipole approximation is addressed. A more rigorous solution for microspheres of equal radii was formulated and applied to silica in [12] by Narayanaswamy and Chen. An experimental investigation of this can be found in [13]. The rigorous method in [12] was extended to silica, lithium fluoride, and arsenic selenide nanospheres of equal and unequal radii in [14]. More complex geometries involving spheres include an analysis of sphere-to-plane geometry in [14] and an aggregate of spheres and dense nanoparticulate media in [15] and [16], respectively. A discussion of numerical methods associated with radiative transfer at the nanoscale is discussed in [17].

In this paper the procedure to calculate near-field radiative exchange presented by Narayanaswamy and Chen in [12] for sphere-to-sphere is utilized on cylinders subdivided into spheres to calculate the cylinder-to-cylinder geometry of nanorods. The fundamentals utilized for the applied spherical configuration are discussed in this work. An in-depth explanation of the wave fields and scattering theory fundamentals applied in this work can be found in [18-19]. The Fluctuation Dissipation Theorem (FDT), Dyadic Green's Function (DGF), and Bessel Functions are mathematical tools implemented to express the wave fields. For background on these theorems and functions, the reader is referred to [18-26].

4.2 Formulation

The proposed approximation method involves dividing up each nanorod into spheres, and calculating the radiative transfer between the spheres of one nanorod to the spheres of the other nanorod. This is shown graphically for nanorods with length to diameter ratios of 5:1 in Figure 4.1. A similar framework can be utilized for other length to diameter ratios.

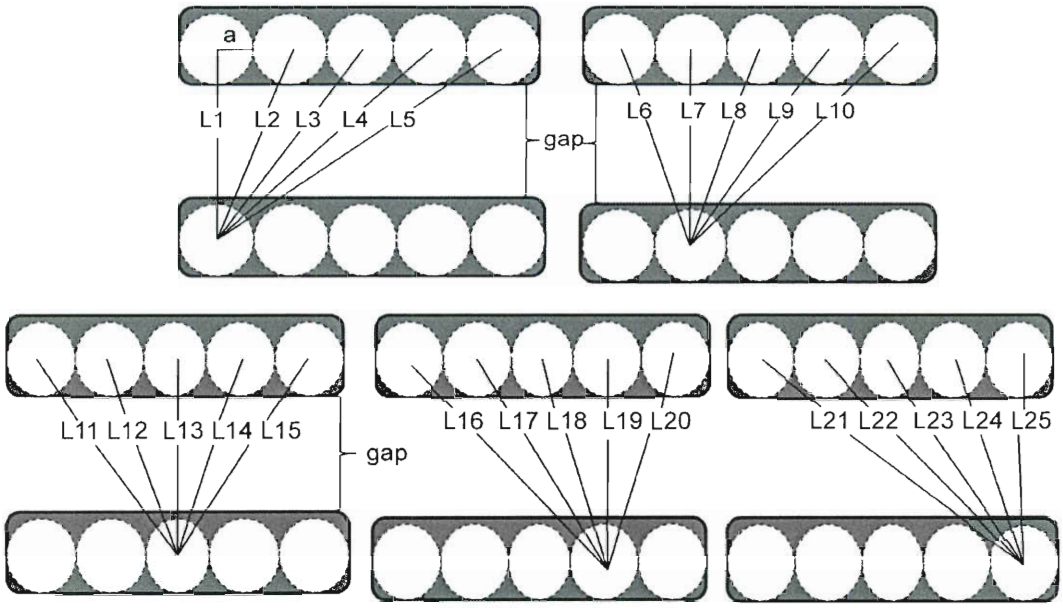

Figure 4.1: Framework for Nanorod-to-Nanorod Radiative Exchange Using Spherical Divisions

The nanosphere radiative exchange is calculated as described in the details that follow for the length calculations given in Equations 4.1 -4.5:

$$L1 = \text{gap} + 2a = L7 = L13 = L19 = L25 \tag{4.1}$$

$$L2 = \sqrt{(L1)^2 + (2a)^2} = L6 = L8 = L12 = L14 = L18 = L20 = L24 \tag{4.2}$$

$$L3 = \sqrt{(L1)^2 + (4a)^2} = L9 = L11 = L15 = L17 = L23 \tag{4.3}$$

$$L4 = \sqrt{(L1)^2 + (6a)^2} = L10 = L16 = L22 \tag{4.4}$$

$$L5 = \sqrt{(L1)^2 + (8a)^2} = L21 \tag{4.5}$$

The process used to calculate the radiative transfer between each sphere, is a method given in [12,14] that includes near-field effects. The Poynting vector, E x H is calculated from the electromagnetic wave fields E and H. The Poynting vector can be written as shown in [12] as:

$$\begin{aligned}&\left\langle E_{i\omega}H^{*}_{j\omega}\right\rangle \\ &= i\omega\mu_0\int_V d^3r'\left\{\overline{\overline{G_E}}(\vec{r}_1,\vec{r},\omega)\overline{\overline{G_M}}^{*}(\vec{r}_1,\vec{r}',\omega)\left\langle\vec{J}_l(\vec{r},\omega)\vec{J}^{*}_m(\vec{r}',\omega)\right\rangle\right\}\end{aligned} \tag{4.6}$$

where μ_0 is the permeability of vacuum. $\overline{\overline{G_E}}(\vec{r}_1,\vec{r},\omega)$ and $\overline{\overline{G_H}}(\vec{r}_1,\vec{r},\omega)$ are the DGFs due to a source at $\vec{r}$. These DGFs incorporate kernals which utilize 2nd rank matrices. Additional references for DGFs are given in the introduction of this work. Note that the integral is taken over the volume, V, containing the source. The notation $\langle\cdot,\cdot\rangle$ indicates a statistical average on the Fourier component of fluctuating current $\vec{J}(\vec{r},\omega)$. The Fluctuation Dissipation Theorem (FDT) given in [21, 22] is next applied. This incorporates the density matrix for thermal fluctuations in terms of the mean energy of the quantum oscillator as follows:

$$\theta(\omega,T)=\hbar\omega\Big/\left(\exp\left(\hbar\omega\big/k_bT\right)-1\right). \tag{4.7}$$

The FDT can then be written as shown in [20] as:

$$\left\langle\vec{J}_l(\vec{r},\omega)\vec{J}_m{}^{*}(\vec{r}',\omega)\right\rangle=\omega\varepsilon_0\varepsilon''(\omega)\theta(\omega,T)\delta_{lm}\delta(\vec{r}-\vec{r}') \tag{4.8}$$

where $\varepsilon''(\omega)$ is the imaginary part of the dielectric function, and ε_0 is the permittivity of a vacuum. Substituting this in to our earlier equation yields:

$$\left\langle E_i(\vec{r}_1,\omega)H_j{}^{*}(\vec{r}_1,\omega)\right\rangle=\frac{i\varepsilon_o\varepsilon''(\omega)\mu_0\omega^2\theta(\omega,T)}{\pi}\int_V d^3r\left\{\left(\overrightarrow{G_E}(\vec{r}_1,\vec{r},\omega)\overrightarrow{G^{*}_H}(\vec{r}_1,\vec{r}',\omega)\right)_{ij}\right\} \tag{4.9}$$

Finally, the Fourier component of the fluctuating fields as given in [23] is

$$\vec{E}(\vec{r}_1,\omega)=i\omega\mu_0\int_V \overline{\overline{G_E}}(\vec{r}_1,\vec{r},\omega)\cdot\vec{J}(\vec{r},\omega)d^3r \tag{4.10}$$

$$\vec{H}(\vec{r}_1,\omega)=\int_V \overline{\overline{G_H}}(\vec{r}_1,\vec{r},\omega)\cdot\vec{J}(\vec{r},\omega)d^3r \tag{4.11}$$

where $\overline{\overline{G_E}}(\vec{r}_1,\vec{r},\omega)$ and $\overline{\overline{G_H}}(\vec{r}_1,\vec{r},\omega)$ are the DGFs due to a source at $\vec{r}$. For additional details of this calculation procedure the reader is referred to [12, 18].

To gain a better understanding of these processes, it is necessary to take a look back at the fundamental vector wave equations that form the foundation of it. The vector wave solution is:

$$\nabla\times\nabla\times\boldsymbol{E}(\boldsymbol{r})-\omega^2\mu\varepsilon(\boldsymbol{E}(\boldsymbol{r}))=0. \tag{4.12}$$

This is derived from the general wave equations shown as:

$$\psi_{m,n}=j_n(kr)L_n^m(\cos\theta)h(m\phi). \tag{4.13}$$

The mathematical functions utilized in the above equation are: Legendre polynomials, $L_n^m(\cos\theta)$, spherical Bessel functions $j_n(kr)$, and time harmonic functions, $h(m\phi)$. The general wave equation is solved from the Helmholtz equation given as:

$$(\nabla^2+k^2)\boldsymbol{E}(\boldsymbol{r})=0. \tag{4.14}$$

The scalar version of the Helmholtz equation is written as

$$(\nabla^2+k^2)\psi(\boldsymbol{r})=0. \tag{4.15}$$

where $\psi(\boldsymbol{r})$ is the scalar potential. Note that the Helmholtz equation is direct derivative of the Maxwell's equations that describe associated electromagnetic fields.

Now that we have discussed the foundation, we can look at the mathematical construction of the vector wave solution using M waves, N waves, and L waves. The L waves are characterized as:

$$\boldsymbol{L}_{nm}(k,\boldsymbol{r})=\frac{1}{k}\nabla\psi_{nm}(k,\boldsymbol{r}) \tag{4.16}$$

The L waves are based on a gradient operator. These waves are translationally invariant. In this work we will focus on M and N since our geometries are cases where one object is a translation of the other. M waves are can be expressed as:

$$\boldsymbol{M}_{nm}(k,\boldsymbol{r})=\nabla\times c\psi_{nm}(\boldsymbol{r}) \tag{4.17}$$

where $\boldsymbol{c}$ is known as the pilot vector. The N waves are written as:

$$\boldsymbol{N}_{nm}(k,\boldsymbol{r})=\frac{1}{k}\nabla\times\boldsymbol{M}(k,\boldsymbol{r})=\frac{1}{k}\nabla\times\nabla\times c\psi_{nm}(\boldsymbol{r}). \tag{4.18}$$

Both M and N waves are based on the curl operator. The M waves can be associated with the transverse electric field, while the N wave as the transverse magnetic field. The forms of these equations change with the coordinate system that is chosen. The spherical coordinate system is unique in that the M and N waves are decoupled. Additional information on L waves, M waves, and N waves can be found in [18] and [19].

Each M and N waves incident on the spherical boundary from the outside produces a reflected wave and transmitted wave. The reflected wave formula for M waves is expressed as:

$$R_c^M = \frac{\sqrt{\varepsilon_1\mu_2}\,\hat{j}_n(k_2a)\hat{j}_n'(k_1a) - \sqrt{\varepsilon_2\mu_1}\,\hat{j}_n(k_1a)\hat{j}_n'(k_2a)}{\sqrt{\varepsilon_2\mu_1}\,\hat{j}_n(k_1a)\hat{h}_n'^{(1)}(k_2a) - \sqrt{\varepsilon_1\mu_2}\,\hat{h}_n^{(1)}(k_2a)\hat{j}_n'(k_1a)} \tag{4.19}$$

and the transmitted wave formula is:

$$T_c^M = \frac{i\mu_1\sqrt{\frac{\varepsilon_1}{\mu_1}}}{\sqrt{\varepsilon_2\mu_1}\,\hat{j}_n(k_1a)\hat{h}_n'^{(1)}(k_2a) - \sqrt{\varepsilon_1\mu_2}\,\hat{h}_n^{(1)}(k_2a)\hat{j}_n'(k_1a)}. \tag{4.20}$$

For N waves the reflected wave formula is:

$$R_c^N = \frac{\sqrt{\varepsilon_2\mu_1}\,\hat{j}_n(k_2a)\hat{j}_n'(k_1a) - \sqrt{\varepsilon_1\mu_2}\,\hat{j}_n(k_1a)\hat{j}_n'(k_2a)}{\sqrt{\varepsilon_1\mu_2}\,\hat{j}_n(k_1a)\hat{h}_n'^{(1)}(k_2a) - \sqrt{\varepsilon_2\mu_1}\,\hat{h}_n^{(1)}(k_2a)\hat{j}_n'(k_1a)} \tag{4.21}$$

and the transmitted wave formula is

$$T_c^N = \frac{i\varepsilon_1\sqrt{\frac{\mu_1}{\varepsilon_2}}}{\sqrt{\varepsilon_1\mu_2}\,\hat{j}_n(k_1a)\hat{h}_n'^{(1)}(k_2a) - \sqrt{\varepsilon_2\mu_1}\,\hat{h}_n^{(1)}(k_2a)\hat{j}_n'(k_1a)}. \tag{4.22}$$

Bessel functions are critical is writing the above M and N wave formulas. The types utilized in the spherical configuration include first order, second order, Hankel, and derivative spherical Bessel functions. Spherical Bessel functions of the first kind are written as:

$$j_n(x) \equiv \sqrt{\frac{\pi}{2x}} J_{n+\frac{1}{2}}(x). \tag{4.23}$$

The spherical Bessel functions of the 2nd kind as:

$$y_n(x) \equiv \sqrt{\frac{\pi}{2x}} Y_{n+\frac{1}{2}}(x) \tag{4.24}$$

In the above equations, $J_n(x)$ is a general Bessel function of the first kind and $Y_n(x)$ is a general Bessel function of the second kind. Hankel functions are composed of both first and second order Bessel functions as follows:

$$h_n(x) = j_n(x) + iy_n(x) \tag{4.25}$$

Recurrence relations useful in describing a function derived from the Bessel functions are:

$$j_n'(x) = j_{n-1}(x) - \frac{n}{x} j_n(x) \tag{4.26}$$

and

$$y_n'(x) = y_{n-1}(x) - \frac{n}{x} y_n(x). \tag{4.27}$$

Additional information about Bessel functions can be found in [18, 24-26]. After writing the vector wave solution for the coordinate system of one sphere, the overall vector wave solution is written using the spherical vector translation addition theorem shown as follows:

$$M_{nm}(\boldsymbol{r}) = \sum_{\nu=1} \sum_{\mu=-\nu}^{\nu} \left[M_{\nu\mu}(\boldsymbol{r}') A_{\nu\mu,nm} + N_{\nu\mu}(\boldsymbol{r}') B_{\nu\mu,nm} \right]. \tag{4.28}$$

The approximation presented in this work, by dividing the cylinders into side by side spheres is compared to a rigorous method of cylinder-to-cylinder radiative transfer with near-field effects. This rigorous method follows a similar framework as described by the sphere-to-sphere method, but is adapted to the case of cylinder-to-cylinder. Note that this is a complex calculation procedure which was the motivation for the development of the more simplified approximation method described in this paper. The rigorous method modifications were required for the

calculation procedure to be applicable to cylindrical nanorods. The spherical vector waves with spherical Bessel function were no longer utilized. For the cylindrical configuration, cylindrical vector waves with cylindrical Bessel functions were employed. Cylindrical vector wave functions are described as:

$$\vec{M}_n(k_p,k_z,\vec{r})=\nabla\times\hat{z}J_n(k_p\rho)e^{ik_z z+in\phi} \tag{4.29}$$

and

$$\vec{N}_n(k_p,k_z,\vec{r})=\frac{1}{k}\nabla\times\vec{M}_n(k_p,k_z,\vec{r}) \tag{4.30}$$

where

$$k_\rho^2+k_z^2=k^2 \tag{4.31}$$

Additional details are given in [18]. Cylindrical Bessel functions were built from the spherical Bessel functions based on the following formula:

$$J_n(x)=\sqrt{\frac{2x}{\pi}}j_{n-1/2}(x)) \tag{4.32}$$

where *J(x)* is a cylindrical Bessel function of the first kind, and *j(x)* is a spherical Bessel function of the first kind. Similarly, the relationship between spherical and cylindrical Bessel functions of the 2nd kind is expressed as:

$$Y_n(x)=\sqrt{\frac{2x}{\pi}}y_{n-1/2}(x)) \tag{4.33}$$

where *Y(x)* is a cylindrical Bessel function of the second kind, and y*(x)* is a spherical Bessel function of the second kind. The cylindrical geometry configuration becomes more complex than the spherical configuration given that the M and N waves do not decouple. Thus, instead of scalar coefficients, a matrix must be used to simultaneously store both the M and N field waves. The reflection coefficient matrix looks as follows.

$$\overline{\boldsymbol{R}} = \overline{\boldsymbol{D}}^{-1} \cdot \left[J_n^{(1)}(k_{1\rho}a)\overline{\boldsymbol{J}}_n^{(1)}(k_{2\rho}a) - J_n^{(1)}(k_{2\rho}a)\overline{\boldsymbol{J}}_n^{(1)}(k_{1\rho}a) \right] \tag{4.34}$$

The reader is referred to [18] for additional information. Another modification in the rigorous method was the application of the cylindrical vector addition theorem instead of the spherical vector addition theorm. The cylindrical vector addition theorem is:

$$H_m^{(1)}(k_p|\bar{\rho} - \bar{\rho}'|)e^{im\phi''} = \sum_{n=-\infty}^{\infty} H_{n-m}^{(1)}(k_p\rho')J_n(k_p\rho)e^{in\phi - i(n-m)\phi'} \tag{4.35}$$

See Ref [18, 27-28] for additional cylindrical vector addition theorem details.

4.3 Results

Figure 4.2 shows a comparison between the calculated method using the rigorous method versus the sphere approximation method. Material properties used were taken from [29]. As the near-field heat transfer decreases and far-field dominates, the sphere approximation method draws closer to the rigorous method. The sphere method predicts a slightly lower value than the rigorous method. This is due to the assumption of additive ray transfer of the near-field transfer from each unit sphere. The assumption that the physics of the transfer occurs as far-field physics dictates, under predicts the actual situation. This is understandable since near-field phenomena produce higher results than expected as the gap decreases. Even though the sphere method is

less than the rigorous method, it is still significantly closer of an estimate than what would occur with pure far-field calculations alone. Calculating the spherical case rigorously and using the additive ray transfer assumption provides a significant decrease is complexity and computation time when compared to the rigorous method of nanocylinders as a whole. Thus, the sphere approximation method is a preferred method compared to far-field calculation only when an approximation of radiative heat transfer between nanorods is needed.

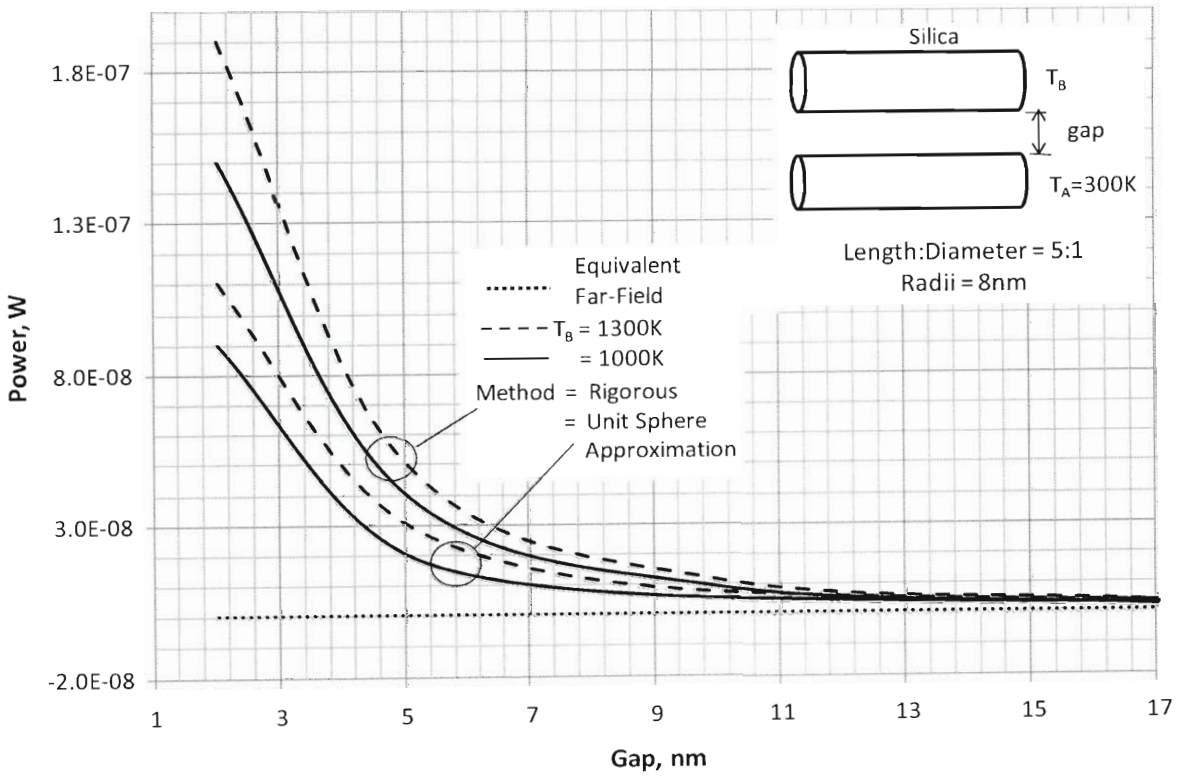

Figure 4.2: Nanorod-to-Nanorod Radiative Exchange vs. Gap: Silica, Equal Radii [30]

The equivalent far-field radiation line that does not contain the near-field radiation is also plotted on this graph. To gain an understanding of the behavior of the radiative heat transfer, one case was chosen and plotted on a specialized set of axis that showed a clear assessment of the

values of the rigorous method, the unit sphere method, and calculations with far-field only. The y-axis was set on a logarithmic scale, and the upper and lower axis values were chosen so as to zoom in around the graph. Figure 4.3 shows this result for the 6nm radii case with a length to diameter ratio of 5:1 with the hotter nanocylinder at 1000K.

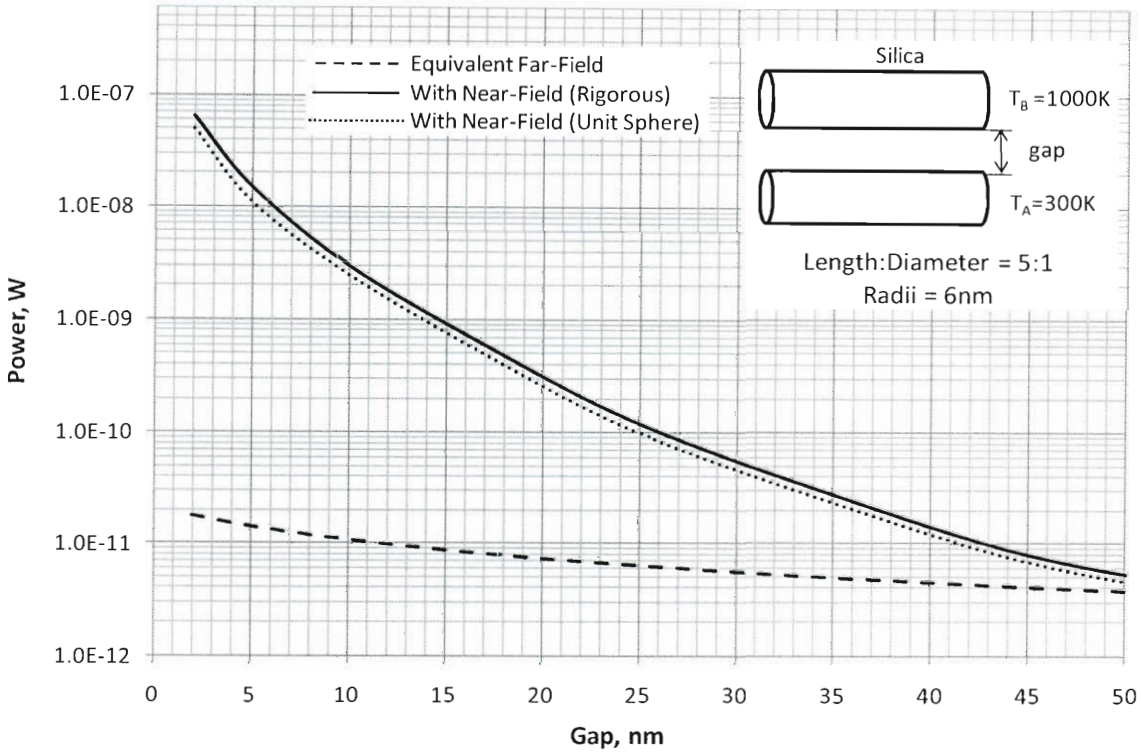

Figure 4.3: Nanorod-to-Nanorod Radiative Exchange vs. Gap : Silica, Length:Diameter = 5:1, Radii = 6nm

To understand the accuracy of the proposed method, an error analysis was completed. An estimation of the error was done by building a computer model of the nanorods and dividing them into spherical units. Millions of rays were shot normally from Sphere 1. The percentage of rays that reach Sphere 4, Sphere 5, Sphere 6 and Space is investigated. This is compared to the

percentage of rays that reach each Sphere when it exists independently from neighboring spheres across from Sphere 1 for the same distance. Figure 4.4 below shows the results of the error investigation. The view from Sphere 1 to Sphere 4 is essentially clear with virtually no error from blocking. As expected, the error of this method increases for Sphere 6 due to blocking from neighboring spheres. The error was originally investigated for a larger range of radii than what was shown. However, in order to be able to view the error, zooming in on a small range of radii was required. The nonsymmetrical nature of the error bar around the main line is due to the fact that the y axis is logarithmic.

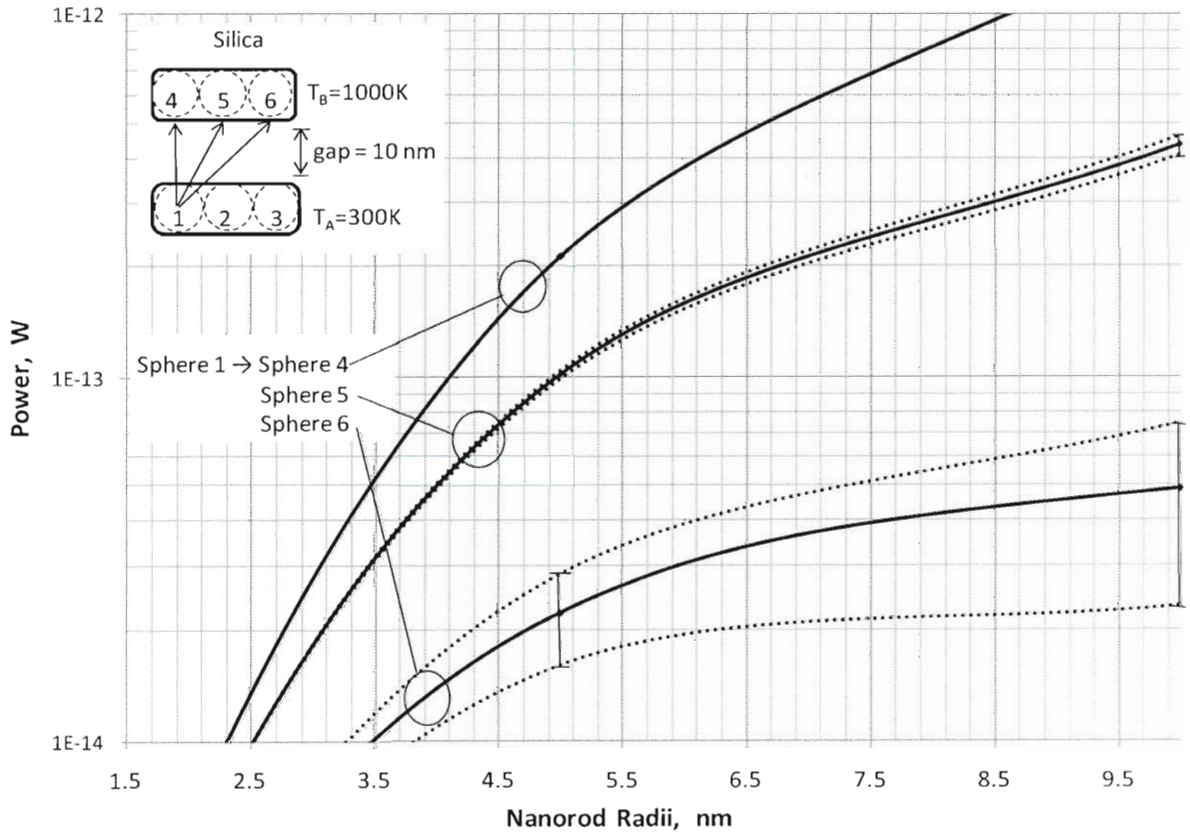

Figure 4.4: Error Analysis Zoomed in at Small Radii Range to Observe Error

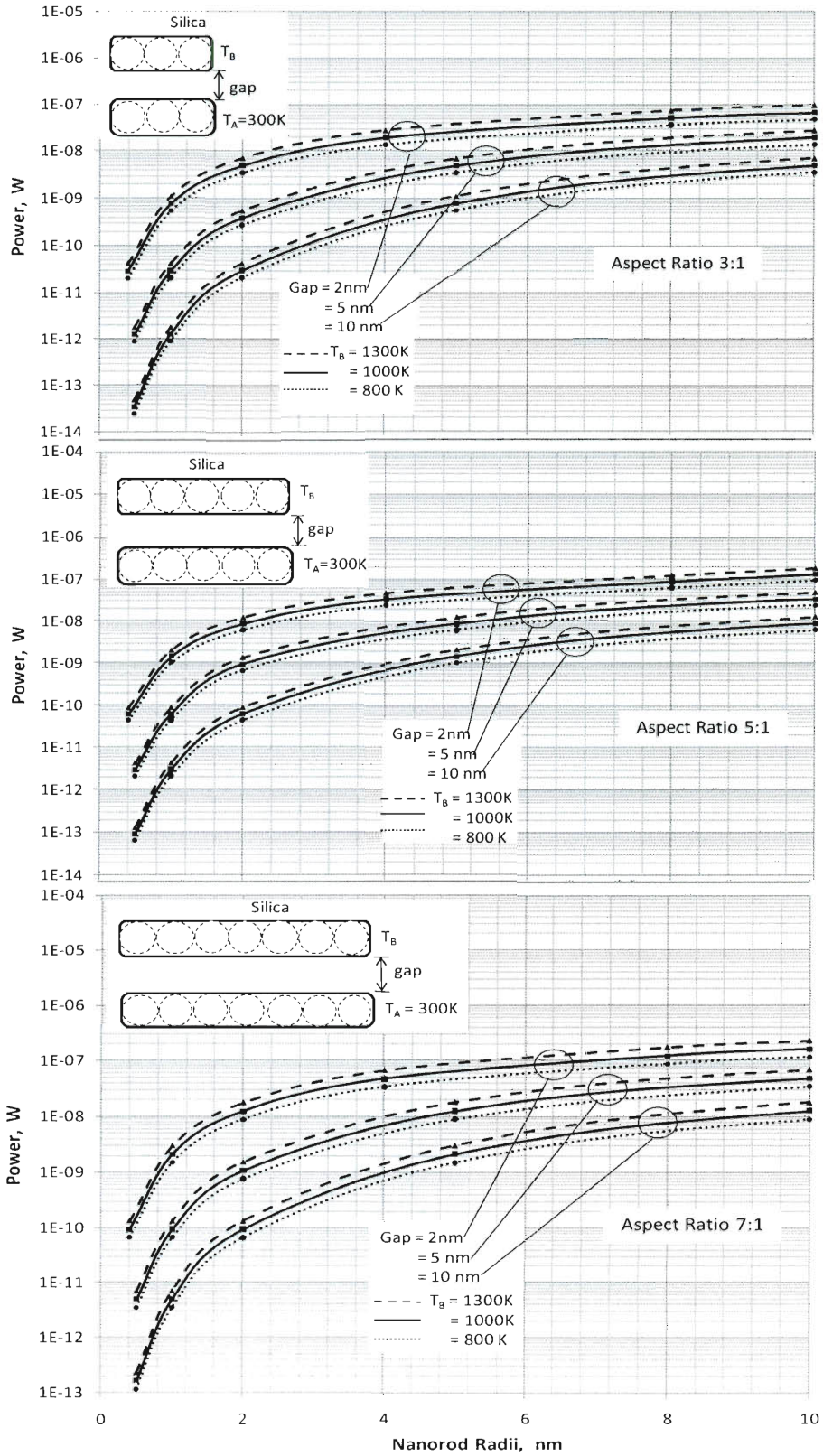

Figure 4.5: Radiative Transfer Power vs. Radius for Silica Nanorods

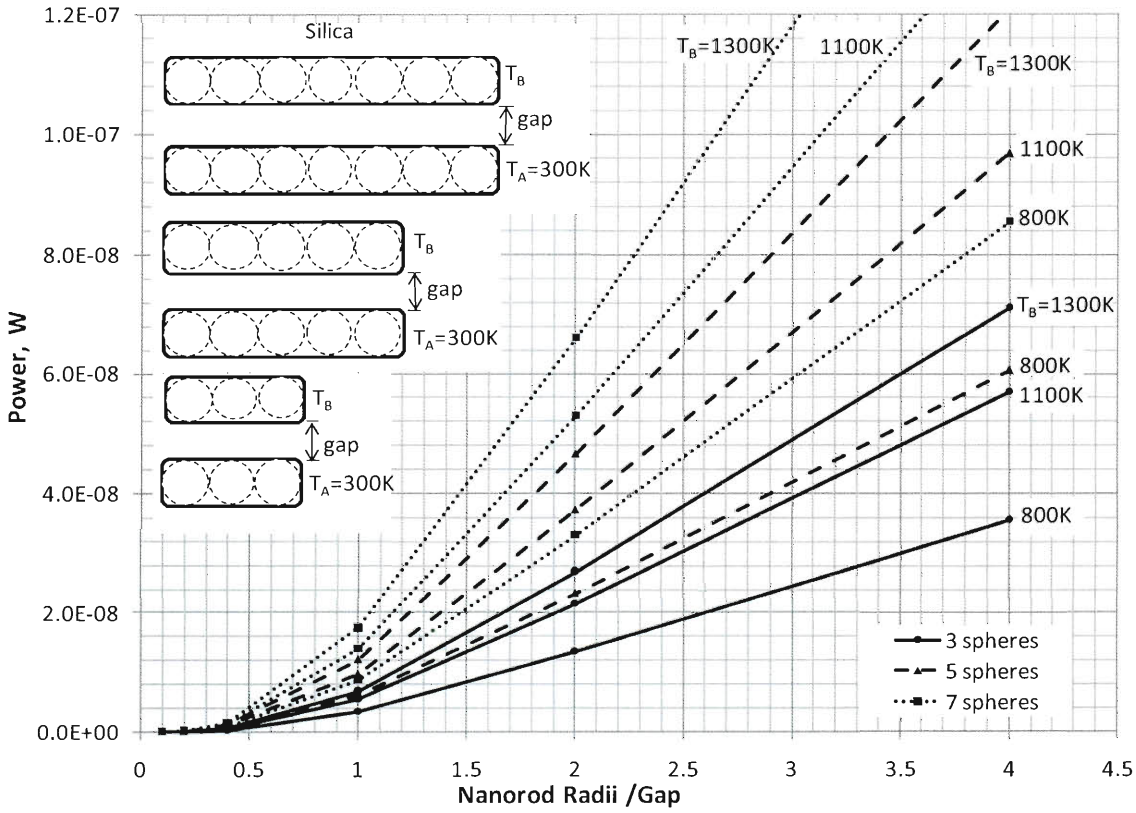

Figure 4.6: Radiative Transfer Power vs. Nanorod radii/gap ratio of Silica nanorods with length:width aspect ratio of 3:1, 5:1, and 7:1 for various temperature differences

Figure 4.5 is for the scenario of radiative heat transfer between nanorods with an aspect ratio of length:width of 3:1, 5:1, and 7:1. Results are shown for nanorods with a radii between 0.5-10 nm with varying temperature differences and gaps of 2, 5, and 10 nm. Figure 4.6 displays radiative heat transfer powers with respect to nanorod radii/gap for nanorods with length:width aspect ratio of 3:1, 5:1, and 7:1 and various temperature differences. Non-dimensionalization is shown to apply here, in that regardless of the radii or gap individual value, cases with the same overall ratios of radii to gap all plot on the same curve.

All of the previous results have been for the case of parallel nanorods. Figure 4.7 depicts radiative heat transfer power for nanorods in a V configuration of various angles for nanorods of 1 nm radii. Nanorod temperature differences shown include 1200K to 300K, 1000K to 300K, and 800K to 300K. Only nanorods with length:width aspect ratio of 3:1, and 5:1, are shown. This is due to the fact that the curve for nanorods with length:width aspect ratio of 7:1 lies too close to the curve for nanorods with length:width aspect ratio of 5:1 to distinguish any difference.

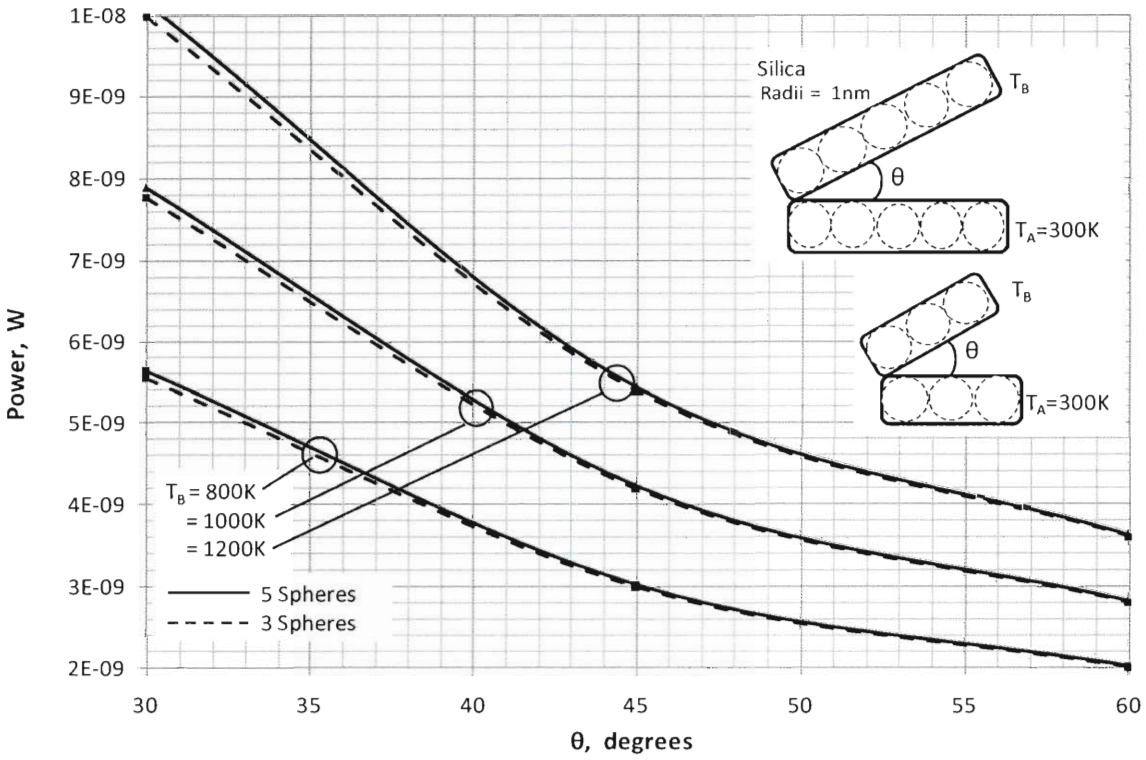

Figure 4.7: Radiative Transfer Power vs. Angle of Silica Nanorods in a V configuration with length:width aspect ratio of 3:1, 5:1, and 7:1 for various temperature differences

4.4 Conclusions

An investigation of cylinder-to-cylinder near-field radiative heat transfer was conducted using a sphere approximation method. A comparison to a previously developed rigorous nanorod near-field radiative heat transfer calculation method was discussed. The near-field impact observed in the heat exchange impact is observed in the plots depicting power vs. gap. The sphere approximation method was then applied to silica nanorods in a variety of configurations. Three different length to diameter nanorod configurations were addressed using the sphere approximation method with plots of power vs. nanorod radii. Geometric effects are observed from a dimensionless relationship in power with respect to nanoradii/gap. Graphical results for various temperatures are shown. A V-shaped configuration is presented with power vs. angle. An assessment of error using ray tracing assumptions is also provided with a ray tracing assumption.

4.6 References

[1] S. Basu, Z.M. Zhang and C.J. Fu, Review of Near-Field Thermal Radiation and Its Application to Energy Conversion, Int J Energy Res, vol. 33, pp. 1203-1232, 2009.

[2] S. Volz, editor, Microscale and Nanoscale Heat Transfer. Topics in Applied Physics Series, Ch. 1, 4, 6, Springer, Berlin, 2006.

[3] K. Joulain, J. Mulet, F. Marquier, R. Carminati and J.J Greffet, Surface Electromagnetic Waves Thermally Excited: Radiative Heat Transfer, Coherence Properties and Casimir Forces Revisited in the Near Field, Surf Sci Rep., Vol. 57, pp. 59-112, 2005.

[4] Z. Zhang and Menguc MP. Special Issue on Nano/Microscale Radiative Transfer,. J Heat Transfer, vol. 129, pp. 1-2, 2007.

[5] J. Mulet, K. Joulain, R. Carminati, and J. Greffet, Enhanced Radiative Heat Transfer at Nanometric Distances, Nanoscale and Microscale Thermophysical Engineering, vol. 6, pp. 209-222, 2002.

[6] Z. Zhang, Nano/Microscale Heat Transfer, Ch. 10, McGraw Hill, New York, 2007.

[7] G. Chen, Nanoscale Energy Transport and Conversion: A Parallel Treatment of Electrons, Molecules, Phonons, and Photons, Ch. 5, Oxford University Press, New York, 2005.

[8] V.P. Carey, G. Chen, C. Grigoropoulos, M. Kaviany, and A. Majumdar, A Review of Heat Transfer Physics, Nanoscale and Microscale Thermophysical Engineering, vol. 12, pp. 1-60, 2008.

[9] M. Francoeur, M.P. Menguc, and R. Vaillon, Local Density of Electromagnetic States within a Nanometric Gap Formed Between Two Thin Films Supporting Surface Phonon Polaritons, J Appl Phys., vol. 107, pp. 034313-034313-8, 2010.

[10] M. Francoeur, M.P. Menguc, and R. Vaillon, Spectral Tuning of Near-Field Radiative Flux Between Two Thin Silicon Carbide Films, J Phys D: Appl Phys., vol. 43, 075501-075501-12, 2010.

[11] M. Francoeur, M.P Menguc, and R. Vaillon, Solution of Near-Field Thermal Radiation in One-Dimensional Layered Media Using Dyadic Green's Function and the Scattering Matrix Method, J Quant Spectrosc & Radiat Transfer, vol. 110 pp. 2002-2018, 2009.

[12] A. Narayanaswamy, and G. Chen, Thermal Near-Field Radiative Transfer Between Two Spheres, Phys Rev B77, vol. 77, pp. 1-12, 2008.

[13] A. Narayanaswamy, S. Shen, and G. Chen, Near-field Radiative Heat Transfer Between a Sphere and a Substrate, Phys Rev B78, vol. 78, pp. 1-4, 2008.

[14] L. Y. Carrillo and Y. Bayazitoglu, Nanosphere Near-field Radiative Heat Exchange Analysis, AIAA J Thermophys Heat Transfer, vol. 24, pp. 309-315, 2010.

[15] D. Mackowski, and M. Mishchenko, Prediction of Thermal Emission and Exchange Among Neighboring Wavelength-Sized Spheres, J Heat Transfer, vol. 130, pp. 1-7, 2008.

[16] R. Prasher, Thermal Radiation in Dense Nano- and Mircoparticulate Media, J Appl Phys., vol. 102, pp. 1-9, 2007.

[17] B. Wong, and M.P. Menguc, A Unified Monte Carlo Treatment of the Transport of Electromagnetic Energy, Electrons, and Phonons in Absorbing and Scattering Media, J Quant Spectrosc & Radiat Transfer, vol. 111, pp. 399-419, 2010.

[18] W.C. Chew, Waves and Fields in Inhomogeneous Media, IEEE Press, Piscataway, pp. 15-16, 184-189, 375-428, 1995.

[19] L. Tsang, J.A. Kong, and K. Ding, Scattering of Electromagnetic Waves: Theories and Application, Wiley, Hoboken, pp. 54-60, 2000.

[20] L.D. Landau, and E.M. Lifshitz, Statistical Physics, 3rd ed., Part I, Reed Educational Publishing, Boston, pp. 386-393, 1985.

[21] S.M. Rytov, Theory of Electric Fluctuations and Thermal Radiation. Bedford: U.S. Airforce Cambridge Research Lab, 1959.

[22] S.M. Rytov, Y.A. Kravtsov and V.I. Tatarskii, Principles of Statistical Radiophysics, Vol 3. pp. 109-22, Berlin: Springer-Verlag, 1989.

[23] C. Tai, Dyadic Green's Function in Electromagnetic Theory, 2nd ed., IEEE Press, Piscataway, 1994.

[24] B.G. Korenev, Bessel Functions and Their Applications, pp. 17-19, CRC Press, Boca Raton, 2002.

[25] M. Abramowitz, I.A. Stegun, editors, Handbook of Mathematical Functions with Formulas, Graphs, and Mathematical Tables, 9th ed., p. 435-78, Dover, New York, 1972.

[26] G. Arfken, Mathematical Methods for Physicists, 3rd ed. pp. 633-4, Academic Press, Orlando, 1985.

[27] I.D. Chremmos, and N.K. Uzunoglu, Transformation of Radially Traveling Cylindrical Waves Between Two Skew Cylindrical Coordinate System, J Opt Soc Am A, vol. 23, pp. 1884-8, 2006.

[28] I. Chremmos, Analytical Computation of the Electromagnetic Field Produced by an Optical Fiber Helix, Prog Electromag Res B, vol. 16, pp. 189-207, 2009.

[29] E.D. Palik, Handbook of Optical Constants of Solids, Academic Press, New York pp. 623-798, 1985.

[30] L. Y. Carrillo and Y. Bayazitoglu, Nanorod Near-field Radiative Heat Exchange Analysis, J Quant Spectrosc & Radiat Transfer, vol. 112, pp. 412-419, 2010.

Chapter 5

Spacecraft Waste Heat Pyroelectric Converter Application Analysis

5.1 Introduction

Energy conversion research has recently focused on capitalizing near-field radiative exchange for innovative applications [1]. Near-field radiative exchange is a phenomenon where increased heat transfer is observed in the configuration of two bodies separated at a distance less than the length of the dominant wavelength of heat transfer. Typically, beyond this distance, classical far-field radiative transfer accurately represents the radiative exchange. However, below this critical distance the classical far-field radiative transfer equations under predict the radiative exchange where near-field radiative exchange dominates. The limitations of classical far-field radiative transfer equations are discussed in [2]. The near-field exchange is dependent on the temperature of the bodies, given that the dominant wavelength is also temperature dependent. The relationship between body temperature and dominant wavelength can be described by Wien's displacement with certain deviations as given in [3]. Physically, near-field radiative exchange occurs when the separation distance criterion is satisfied and evanescent waves can tunnel from one surface to the other. Conditions do not support radiation tunneling beyond the critical separation distance and the evanescent waves decay prior to reaching the neighboring surface. Additional information about near-field radiative exchange can be found in [2, 4-9].

A variety of investigations have been conducted to analyze the near-field radiative exchange for different geometric configurations. In [2, 6] semi-infinite bodies are covered. Spherical

geometries are addressed using several different calculation procedures in [10-14] and the key concepts are provided in [10]. These include topics in wave field and scattering theory, the Fluctuation Dissipation Theorem (FDT), Dyadic's Green Function (DGF), and Bessel Functions. Additional information about the mathematics associated with the FDT, DGF, and Bessel Functions is contained in [15-23]. The materials investigated in these spherical works include lithium fluoride, silica, and arsenic selenide. These two geometries were combined and a sphere to plane analysis was done for silica in [12]. Layered media of cubic boron nitride is considered in [24] and thin films in [25, 26]. An analysis of nanorods was conducted in [27-28]. For a discussion of near-field radiative exchange numerical methods, the reader is referred to [29].

Methodologies from some of these works are utilized to calculate the geometry that occurs in the energy conversion device given in [30]. This device generates electricity from waste heat using pyroelectric materials. Fundamentals concepts enabling this device are presented in the next section. For further details regarding energy conversion devices and pyroelectric material effects, the reader is referred to [30-37]. A plane-to-plane near-field radiative exchange geometric configuration is displayed in the device. To calculate this, an asymptotic method first introduced for sphere-to-plane in [12] is utilized and applied for silica and lithium fluoride.

A brief mention of considerations for non-local optical response is given here for completeness. Non-local optical response has been seen to occur in the near-field radiative exchange regime with respect to the resonant regions according to [38]. Certain materials possess resonant regions, whereby in certain wavelength regions, the near-field radiative exchange values spike. Materials with large, well-defined resonant regions provide idea support for near-field radiative transfer. The non-local optical response is observed as a blue-shift of the resonance region along with secondary resonance excitation. The non-local optical response is

neglected. Even though a blue-shift causes the resonant peak to shift by wavelength, the overall magnitude of the resonant regions is not impacted. In this work the total contributions of near-field radiative exchange from all wavelengths are considered, so the blue-shift effect is not expected to impact results. The secondary resonance excitation will alter the magnitude of the resonant region, thereby having an effect on the overall radiative near-field exchange. However, these excitations are small when compared to the overall resonant region magnitude, so as a first step it is acceptable to neglect this excitation. Full consideration of non-local optical response is left as future work.

5.2 Near-Field Heat Transfer Formulation

To calculate the radiative transfer between two planes, an approximation is employed. The transfer between a sphere and a plane was calculated using an asymptotic method in an earlier work [12]. This method is taken and expanded to the case of plane-to-plane. To apply, one of the planes is assumed to be composed of spheres. This asymptotic method is superimposed on each sphere comprising the plane to get the total near-field radiative transfer for plane to plane.

The fundamentals of the asymptotic method are based on a calculation methodology described in [10-11] for sphere-to-sphere near-field radiative transfer. To calculate the overall energy transfer for a given configuration, the electromagnetic field is considered taking into consideration contributions from the magnetic and electric fields. The Poynting vector can then be acquired. The Poynting vector is written as follows from [10]:

$$\begin{aligned}&\left\langle E_{i\omega} H^{*}_{j\omega} \right\rangle \\ &= i\omega\mu_0 \int_V d^3r' \left\{ \overline{\overline{G_E}}(\vec{r}_1, \vec{r}, \omega) \overline{\overline{G_H}}^{*}(\vec{r}_1, \vec{r}', \omega) \left\langle \vec{J}_l(\vec{r}, \omega) \vec{J}^{*}_m(\vec{r}', \omega) \right\rangle \right\}\end{aligned} \tag{5.1}$$

where $\bar{J}(\vec{r},\omega)$ is the Fourier component of the fluctuating current and μ_0 is the permeability of vacuum. Due to the fluctuations with regards to the current, a statistical average must be employed to capture a steady state assessment. The statistical average is represented as $\langle\cdot,\cdot\rangle$. $\overline{\overline{G_E}}(\vec{r}_1,\vec{r},\omega)$ and $\overline{\overline{G_H}}(\vec{r}_1,\vec{r},\omega)$ are kernels of 2nd rank dyad tensors. These functions are termed Dyadic Green's Functions (DGFs) due to a source at $\vec{r}$. For additional details regarding background and uses of DGFs, the readers is referred to [15, 16, and 20].

To make the equation easier to imagine we incorporate the Fluctuation Dissipation Theorem (FDT) described in [19]. The FDT relates the thermal fluctuations with the mean energy quantum oscillator $\theta(\omega,T)$. The mean energy quantum oscillator is written as:

$$\theta(\omega,T)=\hbar\omega\Big/\left(\exp\left(\hbar\omega/k_bT\right)-1\right). \tag{5.2}$$

There are several forms of the FDT, according to [17], it can be expressed as

$$\left\langle \bar{J}_l(\vec{r},\omega)\bar{J}_m^{\,*}(\vec{r}',\omega)\right\rangle=\omega\varepsilon_0\varepsilon''(\omega)\theta(\omega,T)\delta_{lm}\delta(\vec{r}-\vec{r}') \tag{5.3}$$

Combining the FDT and the Poynting vector equations yields:

$$\left\langle E_i(\vec{r}_1,\omega)H_j^{\,*}(\vec{r}_1,\omega)\right\rangle=\frac{i\varepsilon_o\varepsilon''(\omega)\mu_0\omega^2\theta(\omega,T)}{\pi}\int_V d^3r\left\{\left(\overline{\overline{G_E}}(\vec{r}_1,\vec{r},\omega)\overline{\overline{G_H}}^{\,*}(\vec{r}_1,\vec{r}',\omega)\right)_{ij}\right\} \tag{5.4}$$

where the fluctuating fields have the Fourier components given in [20] as:

$$\vec{E}(\vec{r}_1,\omega)=i\omega\mu_0\int_V\overline{\overline{G_E}}(\vec{r}_1,\vec{r},\omega)\cdot\bar{J}(\vec{r},\omega)d^3r \tag{5.5}$$

$$\vec{H}(\vec{r}_1,\omega)=\int_V\overline{\overline{G_H}}(\vec{r}_1,\vec{r},\omega)\cdot\bar{J}(\vec{r},\omega)d^3r \tag{5.6}$$

Further explanation of the procedural formulation can be found in [10].

The equations presented insofar are based on the fundamental wave equation written as:

$$\nabla\times\nabla\times\boldsymbol{E}(\boldsymbol{r})-\omega^2\mu\varepsilon(\boldsymbol{E}(\boldsymbol{r}))=0. \tag{5.7}$$

The related general wave equation has a solution that takes the form:

$$\psi_{m,n}=j_n(kr)L_n^m(\cos\theta)h(m\phi). \tag{5.8}$$

where, $L_n^m(\cos\theta)$ is a Legendre polynomials, $j_n(kr)$ designates a spherical Bessel functions, and $h(m\phi)$ indicates a time harmonic functions. The general wave equation can be handled in any coordinates of interest: rectangular, spherical, or cylindrical coordinates. In this case, the equations were solved in the spherical coordinate system since the procedure originated from the sphere-to-sphere geometry. The general wave equation is solved from the Helmholtz equation which is expressed in vector form as:

$$\left(\nabla^2+k^2\right)\boldsymbol{E}(\boldsymbol{r})=0. \tag{5.9}$$

and in scalar form as:

$$\left(\nabla^2+k^2\right)\psi(\boldsymbol{r})=0. \tag{5.10}$$

The Helmholtz equations come from Maxwell's equations which govern the electromagnetic fields.

To solve the vector wave equation, we can mathematically construct a solution based on details given [15, 16]. Three types of waves compose the vector wave solution: M waves, N waves, and L waves. The L waves utilize a gradient operator in the equation as follows:

$$\boldsymbol{L}_{nm}(k,\boldsymbol{r})=\frac{1}{k}\nabla\psi_{nm}(k,\boldsymbol{r}) \tag{5.11}$$

L waves are translationally invariant and therefore do not play a primary role in the geometric configurations where one object is a simple translation of the other. The M and N waves are based on the curl operator and characterizes as:

$$\boldsymbol{M}_{nm}(k,\boldsymbol{r})=\nabla\times c\psi_{nm}(\boldsymbol{r}) \tag{5.12}$$

and

$$\boldsymbol{N}_{nm}(k,\boldsymbol{r})=\frac{1}{k}\nabla\times\boldsymbol{M}(k,\boldsymbol{r})=\frac{1}{k}\nabla\times\nabla\times c\psi_{nm}(\boldsymbol{r}) \tag{5.13}$$

where $\boldsymbol{c}$ is known as the pilot vector. The M and N waves can be associated with the transverse electric field and transverse magnetic field, respectively. The forms of these equations are quite different for spherical, rectangular, and cylindrical coordinate systems. It can be noted that in spherical systems the M and N waves are decoupled making these systems less numerically complex compared to others.

The M and N waves hit the spherical boundary from the outside. These are incident standing waves. A reflected wave and a transmitted wave are produced. The reflected wave for M waves is governed by the equation:

$$R_c^M=\frac{\sqrt{\varepsilon_1\mu_2}\,\hat{j}_n(k_2a)\hat{j}_n'(k_1a)-\sqrt{\varepsilon_2\mu_1}\,\hat{j}_n(k_1a)\hat{j}_n'(k_2a)}{\sqrt{\varepsilon_2\mu_1}\,\hat{j}_n(k_1a)\hat{h}_n'^{(1)}(k_2a)-\sqrt{\varepsilon_1\mu_2}\,\hat{h}_n^{(1)}(k_2a)\hat{j}_n'(k_1a)} \tag{5.14}$$

and the transmitted wave formula by:

$$T_c^M = \frac{i\mu_1\sqrt{\frac{\varepsilon_1}{\mu_1}}}{\sqrt{\varepsilon_2\mu_1}\hat{j}_n(k_1a)\hat{h}_n'^{(1)}(k_2a) - \sqrt{\varepsilon_1\mu_2}\hat{h}_n^{(1)}(k_2a)\hat{j}_n'(k_1a)}. \tag{5.15}$$

For N waves, the reflected wave is expressed:

$$R_c^N = \frac{\sqrt{\varepsilon_2\mu_1}\hat{j}_n(k_2a)\hat{j}_n'(k_1a) - \sqrt{\varepsilon_1\mu_2}\hat{j}_n(k_1a)\hat{j}_n'(k_2a)}{\sqrt{\varepsilon_1\mu_2}\hat{j}_n(k_1a)\hat{h}_n'^{(1)}(k_2a) - \sqrt{\varepsilon_2\mu_1}\hat{h}_n^{(1)}(k_2a)\hat{j}_n'(k_1a)} \tag{5.16}$$

and the transmitted wave:

$$T_c^N = \frac{i\varepsilon_1\sqrt{\frac{\mu_1}{\varepsilon_2}}}{\sqrt{\varepsilon_1\mu_2}\hat{j}_n(k_1a)\hat{h}_n'^{(1)}(k_2a) - \sqrt{\varepsilon_2\mu_1}\hat{h}_n^{(1)}(k_2a)\hat{j}_n'(k_1a)}. \tag{5.17}$$

The equations above utilize a mathematical tool known as spherical Bessel, along with their related functions. These include the first order, second order, Hankel, and derivative spherical Bessel functions. Spherical Bessel functions of the first kind are of the form:

$$j_n(x) \equiv \sqrt{\frac{\pi}{2x}} J_{n+\frac{1}{2}}(x). \tag{5.18}$$

The spherical Bessel functions of the 2nd kind are given as:

$$y_n(x) \equiv \sqrt{\frac{\pi}{2x}} Y_{n+\frac{1}{2}}(x) \tag{5.19}$$

$J_n(x)$ is a general Bessel function of the first kind and $Y_n(x)$ is a general Bessel function of the second kind. The Hankel function is composed of first and second order Bessel functions as:

$$h_n(x) = j_n(x) + iy_n(x) \tag{5.20}$$

Additional useful relationships regarding Bessel functions are known as recurrence relations and written as:

$$j_n'(x) = j_{n-1}(x) - \frac{n}{x} j_n(x) \tag{5.21}$$

and

$$y_n'(x) = y_{n-1}(x) - \frac{n}{x} y_n(x) \tag{5.22}$$

See [15, 21-23] for further details concerning these functions.

After the vector wave solution has been constructed for the two different bodies, the overall vector wave solution is calculated using the vector translation addition theorem expressed as:

$$M_{nm}(\boldsymbol{r}) = \sum_{\nu=1}^{\nu} \sum_{\mu=-\nu} \left[M_{\nu\mu}(\boldsymbol{r}') A_{\nu\mu,nm} + N_{\nu\mu}(\boldsymbol{r}') B_{\nu\mu,nm} \right] \tag{5.23}$$

Using this method, the near-field radiative exchange can be computed for sphere-to-sphere configurations.

To take the next step of calculating the plane-to-sphere near-field radiative transfer, the asymptotic method detailed in [12] is applied. This method begins with two spheres of equal radii that are separated with a gap equal to the gap between the planes in the configuration being considered. The initial calculation is done in this sphere-to-sphere configuration. The next step is to take one of the spheres and increase the radius, while maintaining the gap away from the other sphere. The near-field transfer is then recalculated. This process is repeated while incrementally increasing the radius of one of the spheres. As the sphere increases to a large enough radius such that it closely approximates a plane-to-sphere configuration, the near-field

radiative transfer will converge on a value that approaches the near-field radiative transfer of the plane-to-sphere configuration. This can be seen in Figure 5.1.

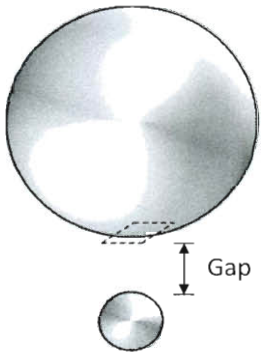

Figure 5.1: Plane to Sphere Near-Field Radiative Heat Transfer Approximation Schematic

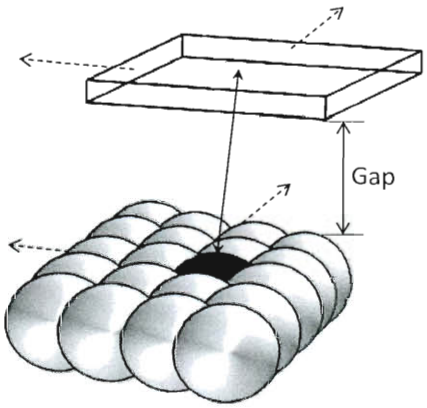

Figure 5.2: Plane-to-Plane Configuration composed of Multiple Spheres and a Plane

Finally, to acquire the transfer between two planes, one plane is assumed to be comprised of smaller spheres, and this calculation is repeated for each sphere with the result totaled. This idea

is shown here graphically in Figure 5.2 where the dotted-lined arrows indicate that the planes can be extended to the desired dimensions. Here one case for the darkened sphere is shown. As stated, this calculation would be repeated for each sphere and the results combined to determine the plane-to-plane transfer.

Two materials were chosen to investigate. This rationale for this choice is based on information presented in [12] where a similar calculation procedure was employed for a different geometric configuration. The materials considered in this paper included silica, lithium niobate, sodium chloride, cubic carbon, arsenic triselenide, silicon dioxide-alpha, titanium dioxide, potassium chloride, silicon monoxide, silicon nitride, and lithium fluoride. Material properties were acquired from [39]. Many of these materials were excluded from further numerical investigation due to lack of availability at the frequency of interest, low potential for technological application, and/or possession of a refractive index that varied with axis. The three materials investigated were arsenic triselenide, silica, and lithium fluoride. From these three materials, silica and lithium fluoride were shown to support the highest degree of near-field radiative transfer from a materials property perspective. Based on these results, the plane-to-plane investigation of this paper was conducted for silica and lithium fluoride. A sample of 10mm x 10mm is taken as this is a reasonable sample size to manufacture a pyroelectric coated with silica or lithium fluoride based on current technology. For purposes of the calculation described in this work, this plane is assumed to be comprised of 400 x 400 25μm spheres.

5.3 Pyroelectric Device Formulation

In [30], the extraction of the electrical energy in an energy conversion device is achieved by capitalizing on the capability of pyroelectric materials to generate electricity when they are heated and cooled. They are governed by the following equations:

$$\dot{D} = \varepsilon \dot{E} + p\dot{T} \tag{5.24}$$

$$\dot{S} = p\dot{E} + c\dot{T}/T \tag{5.25}$$

D, E, T, and S represent the electric induction, electric field, temperature, and entropy, respectively. ε is the dielectric constant. The heat capacity is given by c. The pyroelectric coefficient, p, is unique for different pyroelectric materials. It describes the change in polarization with respect to temperature. Note that the point above a variable indicates the time derivative. The following relationship can also be written:

$$E = -\rho \dot{D} \tag{5.26}$$

where the pyroelectric resistivity is given by ρ.

To gain a better understanding, let us take a look at the physics that occurs when pyroelectrics are heated and cooled. Pyroelectrics are polarized materials meaning that the positive and negative atoms are slightly shifted from equilibrium. They exist in this configuration in steady-state conditions. These shifted atoms are often described as being bound to their current location. In essence, the shifted nature of these atoms causes an internal separation of positive and negative charges creating a static electric dipole. The dipole moment gives an indication of the separation distances of the opposite charges. In equilibrium, the charges are still, and do not create any current. However, when a pyroelectric material is heated, an interesting phenomenon occurs. As the temperature of the material rises, the polarization reduces. This means that the separation distance between the negative and positive charges decreases causing the dipole moment to also decrease. The redistribution of charges during heating creates a temporary voltage and current. The same idea occurs if the material is heated, but the current is in the

opposite direction. When the heating or cooling element is removed from the material, the current and voltage will also be removed, since the charges will no longer be adjusting in equilibrium. A temperature limit known as the Curie temperature designates the highest temperature that the material can maintain its polarization. Above the Curie temperature, the polarization rapidly decreases. To maximize current generation, operation of cooling and heating can be done around this temperature range.

Early research applications such as [31], used the pyroelectric material in a parallel plate capacitor circuit similar to that depicted in the Figure 5.3 schematic shown.

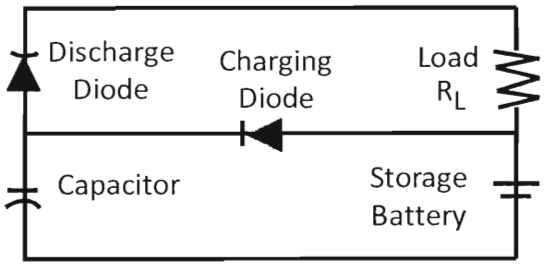

Figure 5.3: Early Pyroelectric Application Configuration: Parallel Plate Capacitor Circuit

At the Curie temperature, the capacitor is charged by the battering through the charging diode. As the temperature of the pyroelectric materials is raised, a voltage across the capacitor results producing electric energy. In such a system the storage battery is recharged such that the only energy utilized for electrical energy generation is that which is used to heat the pyroelectric material. A system built on this fundamental concept would be ideal for applications where waste energy is radiated to control temperature. In particular, this is a good fit for spacecraft applications where large amount of waste energy is radiated out into space, while power is a critical commodity.

This idea of harvesting waste energy has been the subject of other research design developments [30, 32-35, 37]. Several issues have prevented these devices from becoming common in practical applications without further refinement. To gain a broader understanding of this subject, a brief discussion of other non-pyroelectric designs for harvesting energy from waste heat will be given here along with some insights on the current associated limitations from Ref [34]. Thermoelectric generators create electric energy from thermal energy. A mechanism called the Seebeck effect enables electrical energy generation from an electromagnetic field established across two semiconductors at different temperatures. Current designs have only achieved low efficiencies of about ~5%. Further developments are required before this can be a viable operational device. Sterling engines are another technology that generate mechanical energy from thermal energy. These use an electric generator as an intermediate step. Additionally, high heat losses are an issue. Finally, the organic Rankine cycle generates electrical energy from thermal energy. This is done with a refrigerant that is pumped to a boiler to be evaporated and then through a turbine to recondense. This can be a heavy, bulky set up and is typically considered for power plant applications, instead of space applications where mass properties are a factor.

Researchers have refined the fundamental ideas presented thus far to develop prototype pyroelectric generators with improved characteristics from the design described earlier in this work. The more current configurations from Ref [34] will now be presented here. More recently, the thicker pyroelectric material has been replaced by thin films in the range of 250 micrometers made from materials such as Zirconate stannate titanate (PZST). To extract the electricity from the pyroelectric thin film, electrodes of Ni or Ag are attached to the surface of the pyroelectric. Alumina or mica sheet structures containing microchannels hold the

pyroelectric material while allowing silicone oil to flow through and contact the pyroelectric surface. The oil flows from a heat source to a heat sink providing the heat transfer changes the temperature of the pyroelectric. A piston drives the fluid up and down from the heat source at the top to the heat sink at the bottom. A simplified model (not drawn to scale), is shown in Figure 5.4. The piston, silicone oil, and flow tubes are not shown in this simplified model. A Teflon cylinder is shown holding a stack of mica plates with pyroelectric material embedded inside. The mica plates are separated by microchannels when they are stacked together allowing for the silicone oil to flow through. The front view of one single plate from the stack is also shown in Figure 5.4. The layered Kapton tape can be placed as shown in the front view to create the microchannels when the plates are sandwiched together and placed in the cylinder. Note that the converter designs by different researchers have slight variations. The temperature oscillation of the pyroelectric surface corresponds directly to piston oscillations that send oil from the heater to the cooling end. Convective heat transfer is the primary heat transfer method involved.

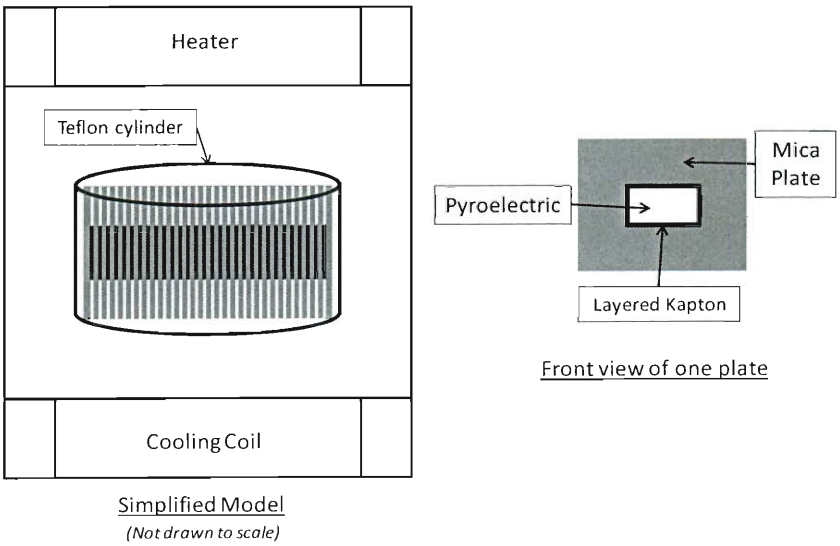

Figure 5.4: Simplified model and individual plate front view shown separately, based on [34] design.

A sample circuit set-up for this pyroelectric converter device is shown in Figure 5.5. Ohms and Kirchoff's laws are fundamental circuit equations that allow for the following relationships to be written for this pyroelectric circuit. The electrical displacement is given as:

$$D_{PE} = \frac{q_{PE}}{A} = \frac{C_1 V_1}{A} \tag{5.24}$$

and the electric field is

$$E_{PE} = \frac{V_{PE}}{t} = \frac{V_2\left(1 + \frac{R_L}{R_2}\right) - V_1}{t} \tag{5.25}$$

where A is the surface area of the pyroelectric and b is the thickness.

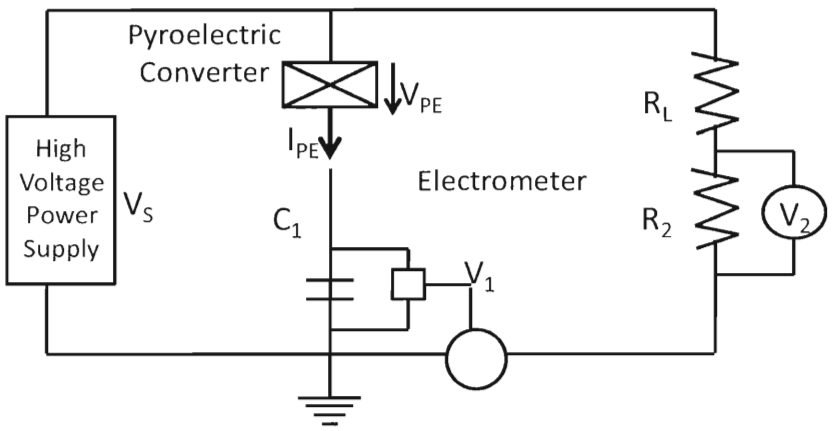

Figure 5.5: Pyroelectric Device Circuit

One limitation of this method is the time taken for the thermal energy to transfer from the heater to the fluid and on to the pyroelectric. Higher oscillation frequency capability from faster thermal transfer can increase the electrical energy production over a given time. Convection is not the fastest known method of heat transfer. Radiation is orders of magnitude faster since the

heat transfers at the speed of light by electromagnetic waves. A set-up utilizing radiation as the primary form of heat transfer would yield improved results. Additionally, entering into the range of near-field radiative transfer would create a higher radiative transfer than far-field radiative transfer only. This novel design was introduced in [30] and a schematic is shown in Figure 5.6.

In this design utilizing near-field radiation, a pyroelectric oscillates back and forth between a cold and hot plate. When the thermocouple reads that the temperature limit has been reached, a signal is sent to the piezoelectric positioners to move the pyroelectric closer to the opposite plate. As the temperature oscillates, electrical energy is produced. Many studies look for the pyroelectric yielding the highest electrical results. As new pyroelectric polymers and nanomaterials are developed, improved energy harvesting will result. A silica coating on the pyroelectric and aluminum plates support near-field radiative transfer. There has been much research in the area of nanopositioning utilizing piezoelectric actuators, as well as other methods. A good overview of the latest research of nanopositioners with corresponding capabilities and limitations is given in [40]. Taking a look at piezoelectrics, almost instantaneously, piezoelectrics can produce mechanical displacement with an applied electric field. An electrical control system separate from the rest of the device is employed. This can be powered by the electrical energy produced by the device. Much less power is required than the piston used in the previous design. A piezoelectric nano-positioning system is a well-tested technology that has been utilized for fifty year. Piezoelectric positioners are currently used in: fiber optic alignment, mirror tilting for imaging, and semiconductor wafer mask alignment. Modern refinements produce resolution to a nanometer or less. Additional details can be found in [41-42].

There are some key characteristics regarding the design of this device. The device performs at maximum efficiency in a vacuum environment. This is because friction is reduced as well as

the heat losses from convection or conduction to the surrounding gaseous environment. The vacuum of space makes it an ideal environment for this device, with the added benefit that

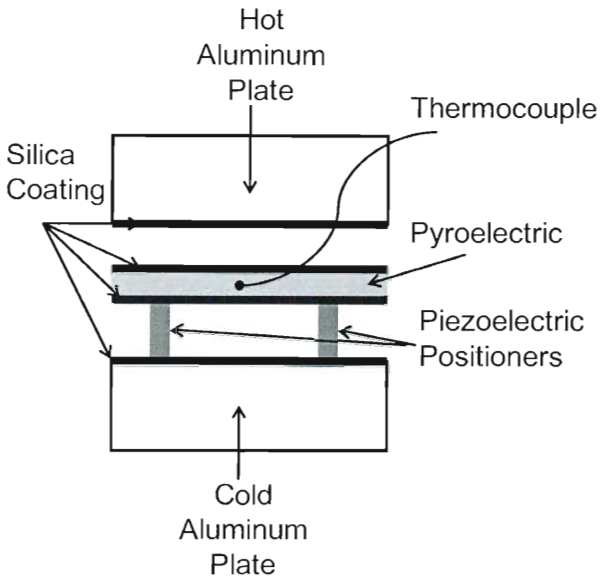

Figure 5.6: Pyroelectric device using near-field radiative heat transfer based on [30] design

spacecrafts often radiate a high rate of waste energy that could be capitalized on. An additional characteristic of the device is the criticality of achieving the correct spacing. Spacing too close could result in contact, and conduction is a much slower process than radiation. Spacing too far could prevent near-field radiative transfer from occurring dropping the radiative transfer rate by orders of magnitude.

5.4 Spacecraft Pyroelectric Energy Conversion Device Design Modification

Internal spacecraft systems produce large amounts of excess heat that is radiated into space to control spacecraft component temperatures to within their limits. These come from a myriad of internal systems including propulsion, guidance/navigation control, life support, environmental

control, computer and electrical systems. This work takes the initial idea presented in [30], but further develops it with the key changes to increase the efficiency and adapt it for use as a spacecraft thermal control system. In previous research, it has been recommended to utilize silica as the coating to enhance near-field radiative design. Based on the calculations, LiF is recommended. In addition to a change in material, the overall rectangular design shown in Figs. 5.7-5.10 is suggested, along with an alternate circular design in Figs. 5.11-5.12. There are several key characteristics that make these designs unique. The rectangular pyroelectric apparatus consists of window-like openings where the pyroelectric material is mounted. A 9 x 3 pyroelectric window mount apparatus is assumed as in Fig. 5.7

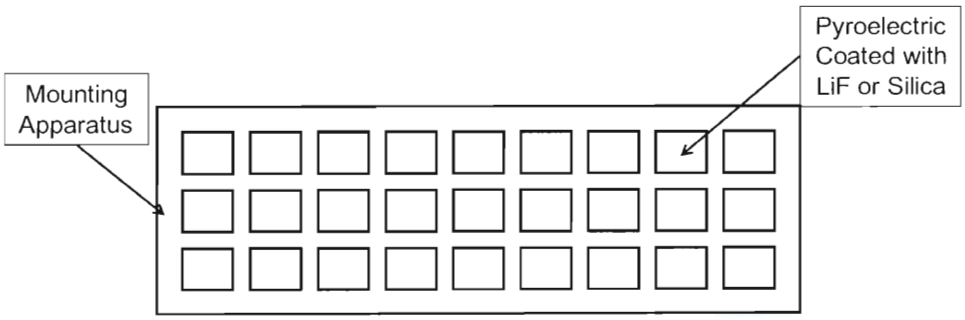

Figure 5.7: Mounting Apparatus

The overall design works in the vacuum of space. This provides the optimum environment for heat loss and friction reduction. The temperature of deep space at approximately 2.7 K alleviates the need for a cooling mechanism in this design. Instead, simply exposing the pyroelectric to deep space will enable it to cool at the fastest rate possible as shown in Fig. 5.8. Another change is that instead of heating on one side and cooling on another, the heat transfer occurs on both sides of the pyroelectric, increasing the rate of heating. Two heating plates rotate

or slide out beside the pyroelectric to heat on each side. The transition phase is shown in Fig. 5.9 and the heating phase in Fig. 5.10. For returning to cooling, these plates slide or rotate back and deep space quickly cools the plates. The figure demonstrates plates that rotate out, but a sliding mechanism would also work. Note that the device is only operated when it is in back of the spacecraft opposite the velocity vector so as to protect it from micrometeroids. If it is leading the spacecraft towards the velocity vector, a cover is placed over it to protect from micrometeoroids.

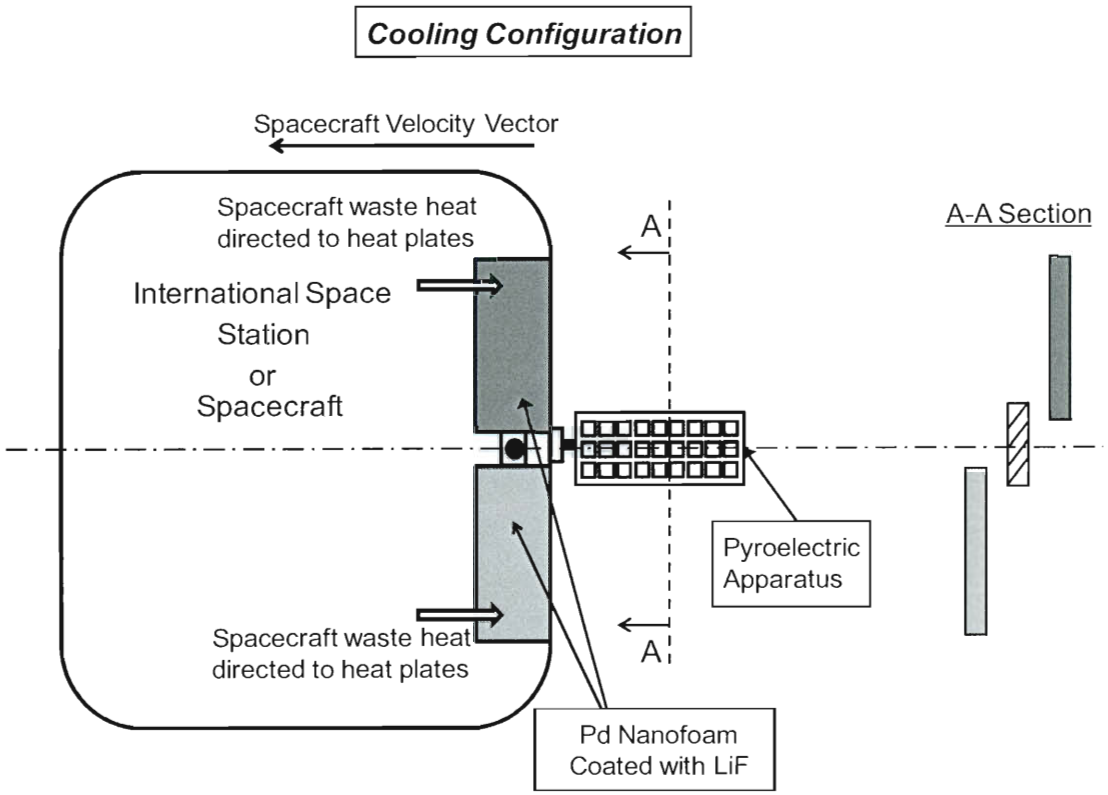

Figure 5.8: Cooling Configuration of the Spacecraft Pyroelectric Waste Heat Converter Device

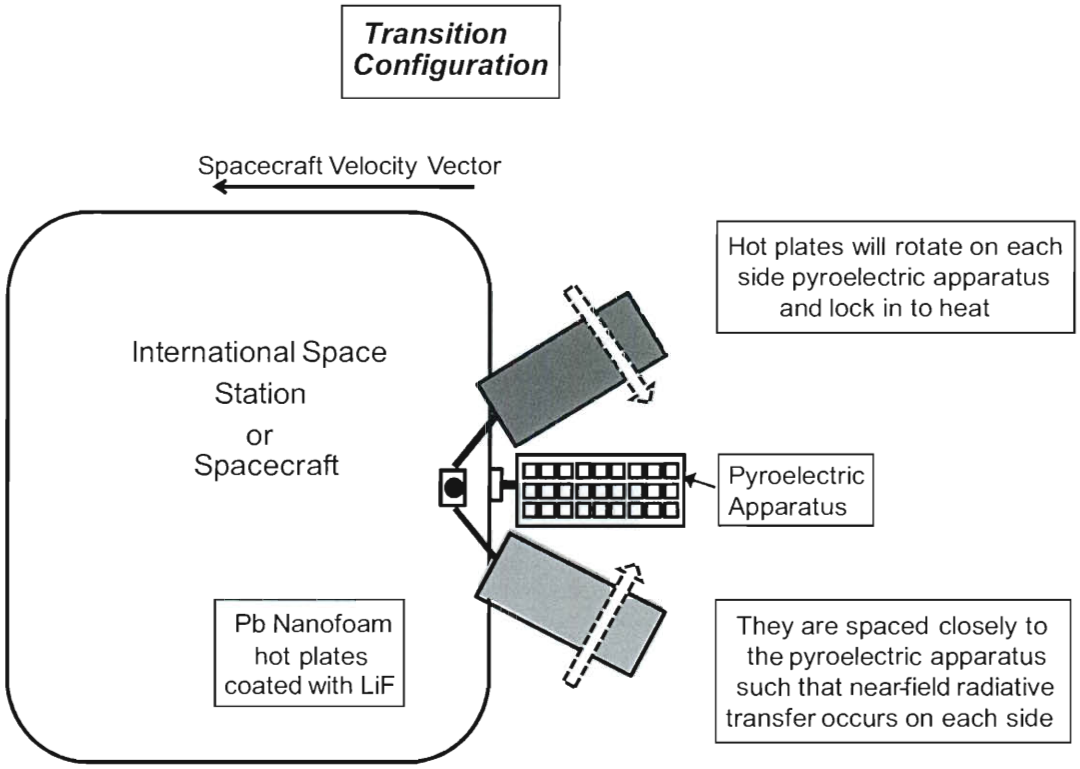

Figure 5.9: Transition Configuration of the Spacecraft Pyroelectric Waste Heat Converter Device

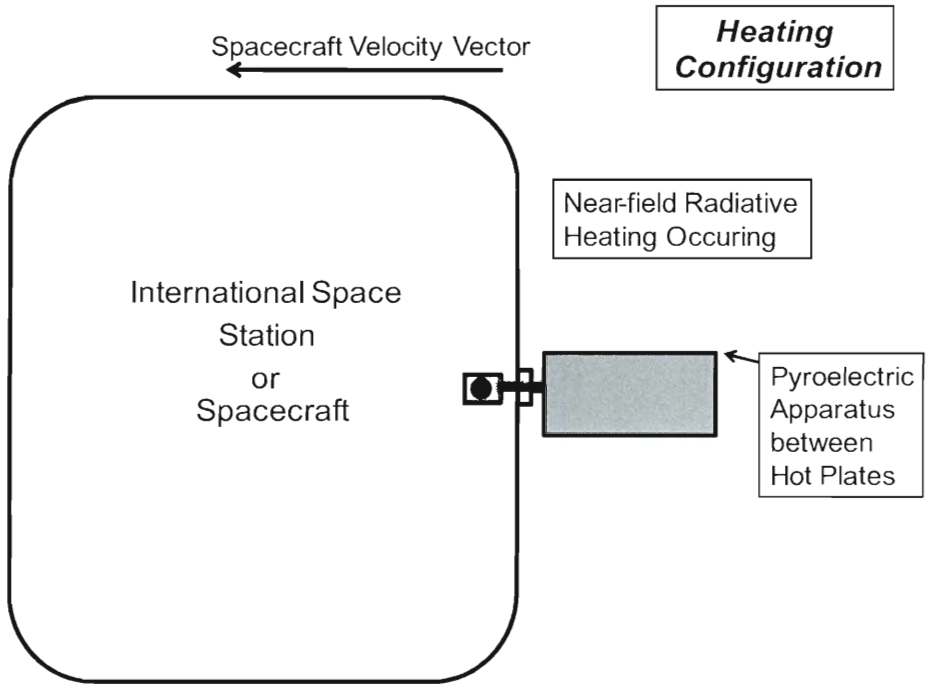

Figure 5.10: Heating Configuration of the Spacecraft Pyroelectric Waste Heat Converter Device

An alternate design configuration is a circular design shown in Figure 5.11-5.12. This design configuration consists of three disks as shown in Figure 5.11. Disks 1 and 3 will be stationary outside disks that will be on the outer ends of the sandwich configuration shown in Figure 5.12. Disks 1 and 3 consist of alternating Pd nanofoam sections, with open sections. The heated sections provide heat to the inner Disk 2 pyroelectric material sections when aligned. Alternatively, when the open sections are aligned with the pyroelectric sections, deep space will cool the pyroelectric material. The outer disks remain stationary, while the inner disk 2 rotates to either the cooling or heating configuration.

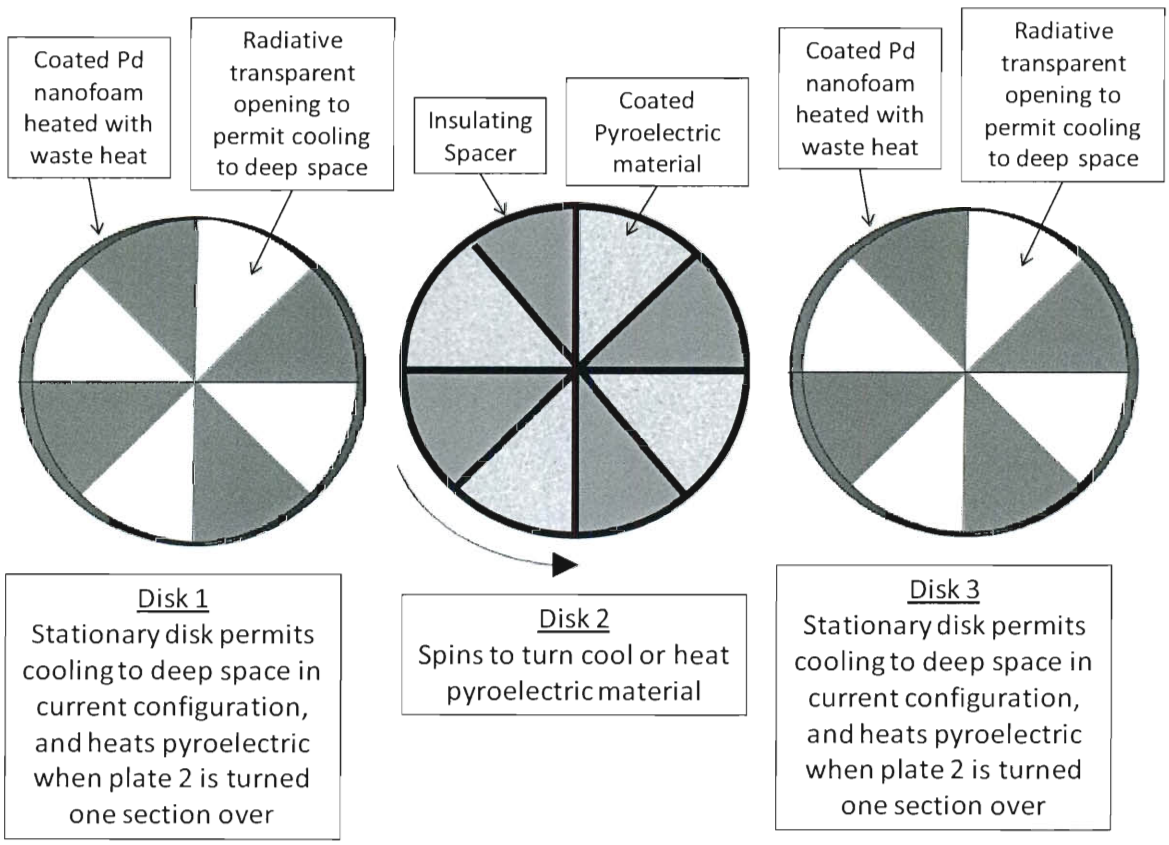

Figure 5.11: Schematic of individual disks

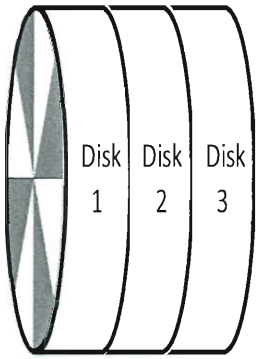

Figure 5.12: Disks assembled in a sandwich configuration

Several different materials were considered for the heating metal sections of the above designs. These materials included aluminum, copper, composite aluminum matrix, aluminum foam, copper nanofoam, and pallandium (Pd) nanofoam. The Pd nanofoam is a unique porous metal that was chosen for several reasons. The low density of 0.01 g/cm^3 makes it have less mass to heat than other metals of higher density. The low specific heat of 0.24 J/g-K also ensures that minimal heat is required to raise the material to the desired temperature. The melting temperature of Pd nanofoam is 1828K making it able to withstand a wide range of temperatures. Additional information about Pd nanofoams can be found in [43].

It is important to discuss the thermodynamics of the device in terms of thermal efficiency denoted as η. Thermal efficiency is a dimensionless ratio that measures of the energy conversion performance of a thermal device. Based on the first law of thermodynamics, the energy output cannot exceed the energy input. Mathematically, thermal efficiency is written as the useable energy out of the device over the energy in or ideal energy of the device. This is expressed as:

$$\eta = \frac{E_{OUT}}{Q_{IN}}. \tag{5.26}$$

Here, E_{OUT}, is the electric power generated by the device. The Q_{IN} is the heat flux provided by the hot plate to the pyroelectric over one cycle. The Carnot thermodynamic cycle is the most ideal thermodynamic cycle. There is not another cycle that surpasses its efficiency. Often the efficiency for given devices are compared to that achieved by the Carnot cycle. The Curzon-Ahlborn (CA) efficiency indicates the efficiency at maximum power of heat engines. This only accounts for the irreversibility of finite heat transfer. The equations for the Carnot efficiency and the CA efficiency are given as:

$$\eta_{Carnot} = 1 - T_c / T_h \tag{5.27}$$

$$\eta_{CA} = 1 - \sqrt{T_c / T_h} \tag{5.28}$$

Additional details on thermal efficiency fundamentals can be found in [44]. For specific details regarding thermal efficiency of pyroelectric material converters the reader is referred to [30].

5.5 Results

The asymptotic method utilized in this work is not the only method that has been utilized to acquire near-field radiative transfer measurements. In [6], an alternate plane-to-plane method for near-field radiation calculations is discussed. As a comparison to the asymptotic method, the results using [6] were calculated and plotted along with the asymptotic method in Figure 5.13.

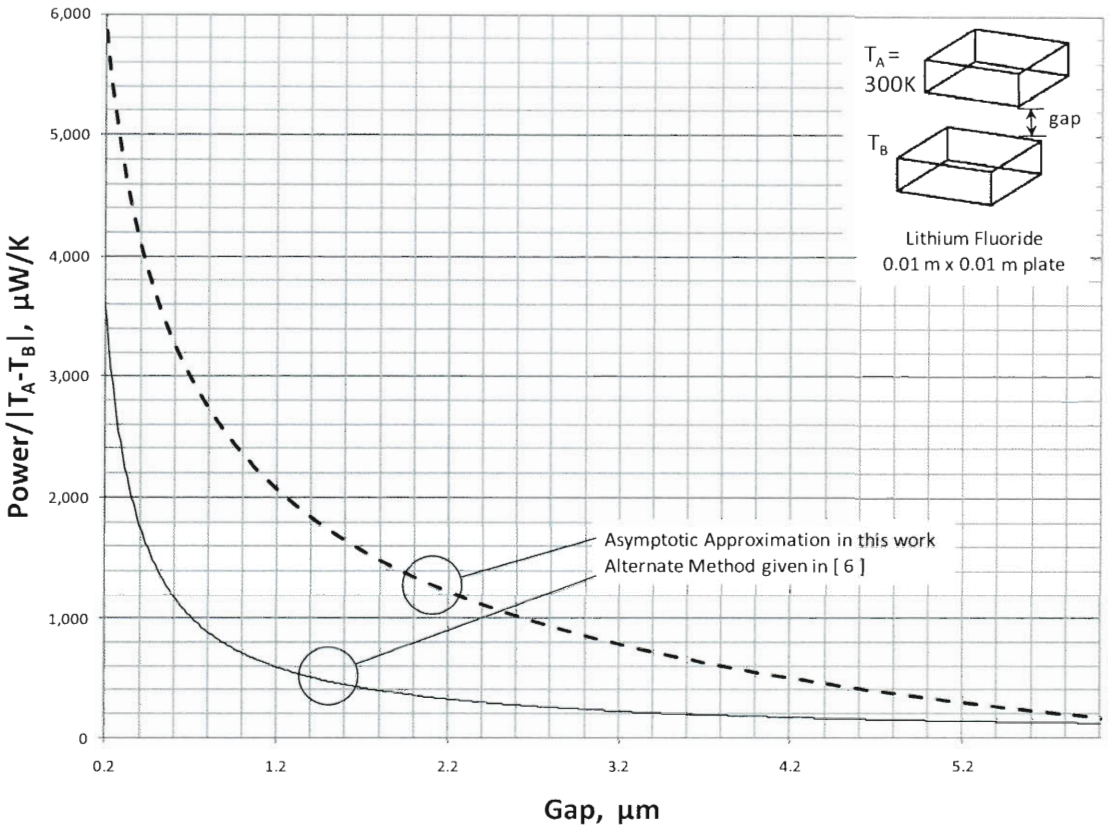

Figure 5.13: Comparison of Calculation Method

Figure 5.14 shows the results for lithium fluoride and silica. As shown, lithium fluoride provides an order of magnitude increase from silica. Figure 5.15 shows the values plotted for near-field heat transfer occurring on each side of this pyroelectric as described in the proposed design of this paper. Using lithium fluoride in this configuration enables near-field heat transfer on both sides, resulting in a 20 fold increase in near-field heat transfer when compared to silica with near-field heat transfer on only one side. This increase heat transfer will enable the pyroelectric material to reach its critical upper temperature faster, and increase the frequency of plate oscillation.

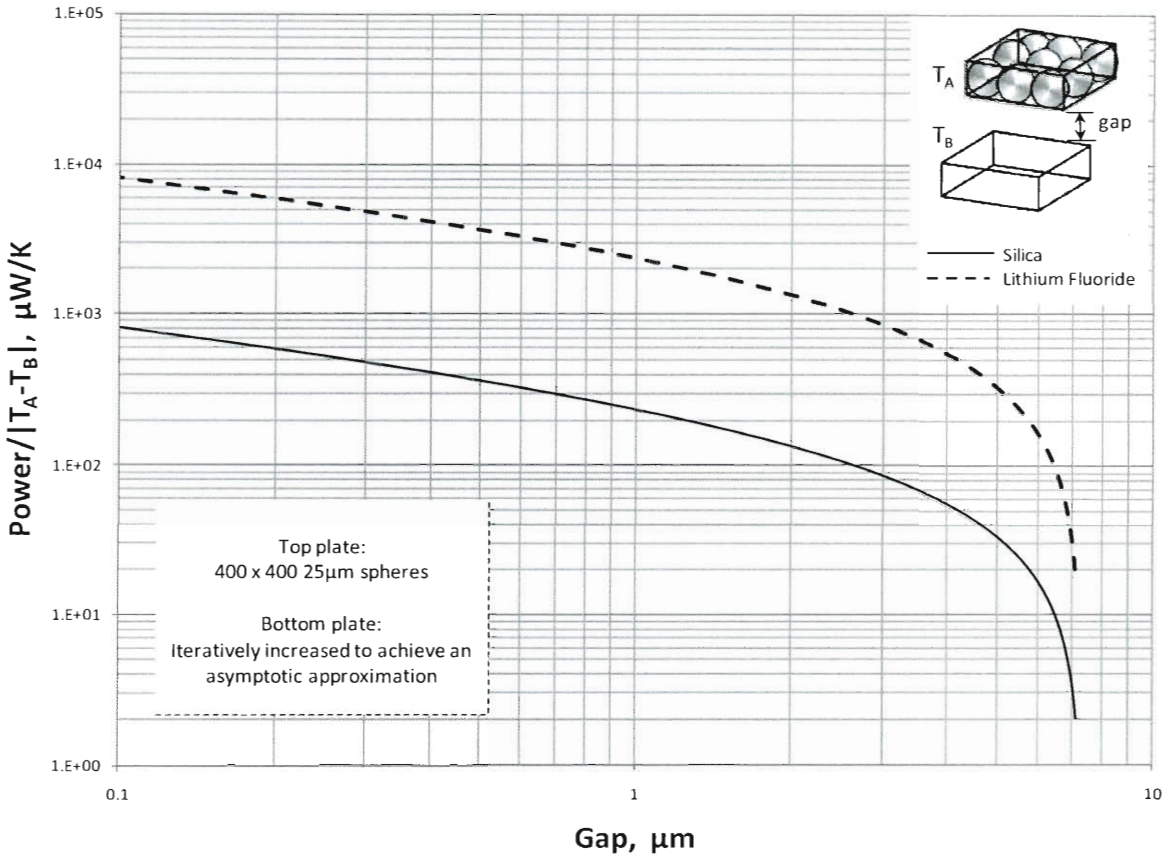

Figure 5.14: Plane-to-Plane Near-field Radiative Transfer

Figure 5.16 shows the near field heat transfer that will occur with the entire mounting apparatus with 27 windows of pyroelectric coated with lithium fluoride or silica. Here, we see values that approach 1 W/K. Note the change of the units to mW. This design would exhibit between two and three order of magnitude increase from the single silica transfer on one side design. Finally the cooling would occur much more rapidly given that the plate will be completely exposed to deep space at approximately 2.7 K. Previous designs required coolers that were held at higher temperatures. The circular design results are displayed in Figure 5.17

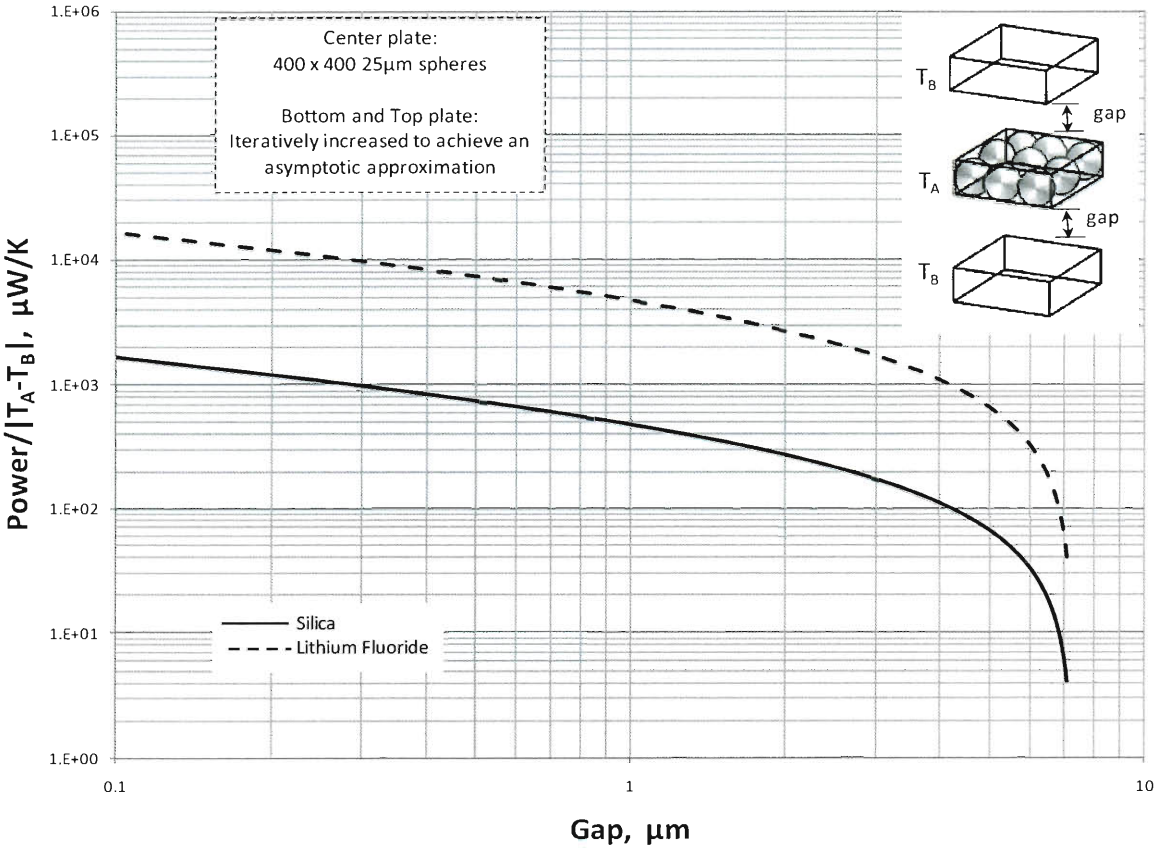

Figure 5.15: Near-field radiation for device configuration of two planes heating each side

The efficiency is calculated for the disk design and the non-linear pyroelectric $PbZr_{0.95}Ti_{0.05}O_3$. Pyroelectric material specifics are given in [45]. The assumptions include a gap of 0.1μm and pyroelectric thickness of 100μm. The heat transfer surface is calculated to be $6x10^2$ mW/k (7k W/K-m^2). A delta temperature of 20K is used. The heat flux from the hot plate to the pyroelectric is 12W. The generated electric power is 0.14W. The average thermodynamic efficiency (η) is 1.16%. The ratio compared to Carnot efficiency (η/η_{Carnot}) is 17%. The ratio to the Curzon-Ahlborn efficiency (η/η_{CA}) is 32%. It is worth noting, however, that currently waste

heat of spacecraft radiated into space results in a 100% loss of this energy, any amount of return would be beneficial from a spacecraft systems standpoint.

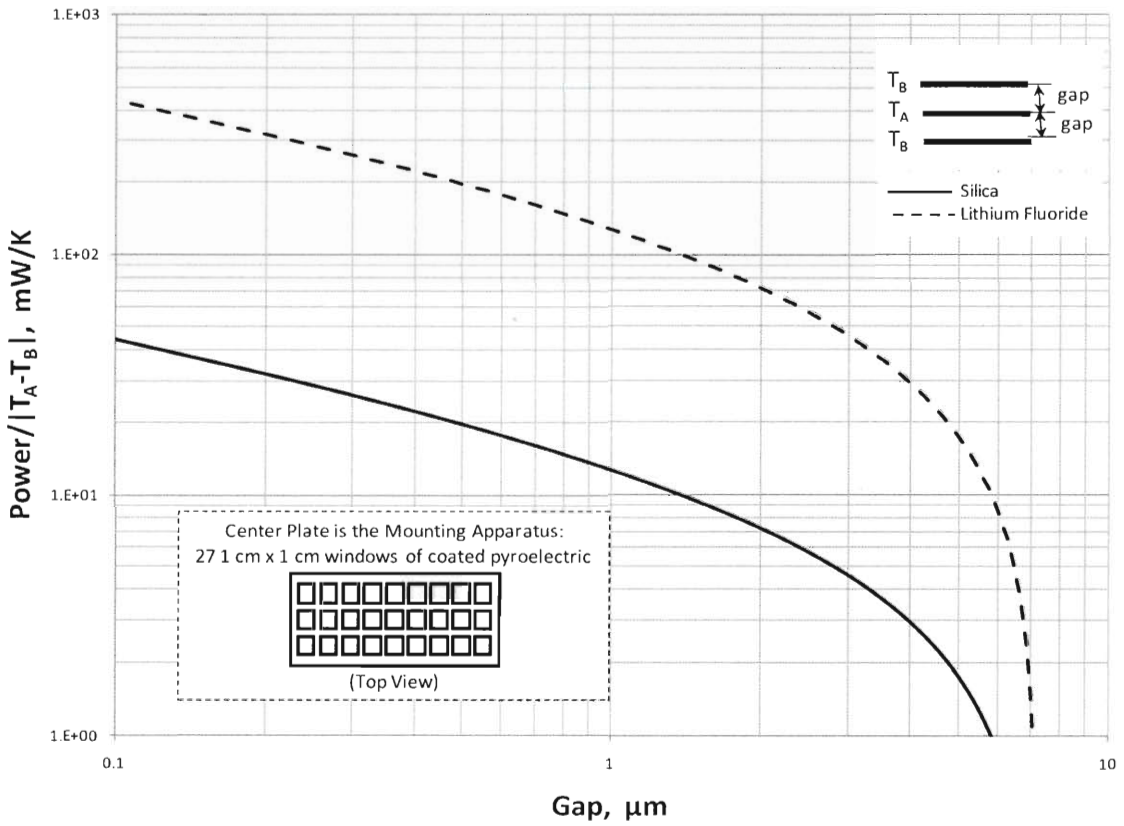

Figure 5.16: Near-field radiative transfer for the entire mounting apparatus

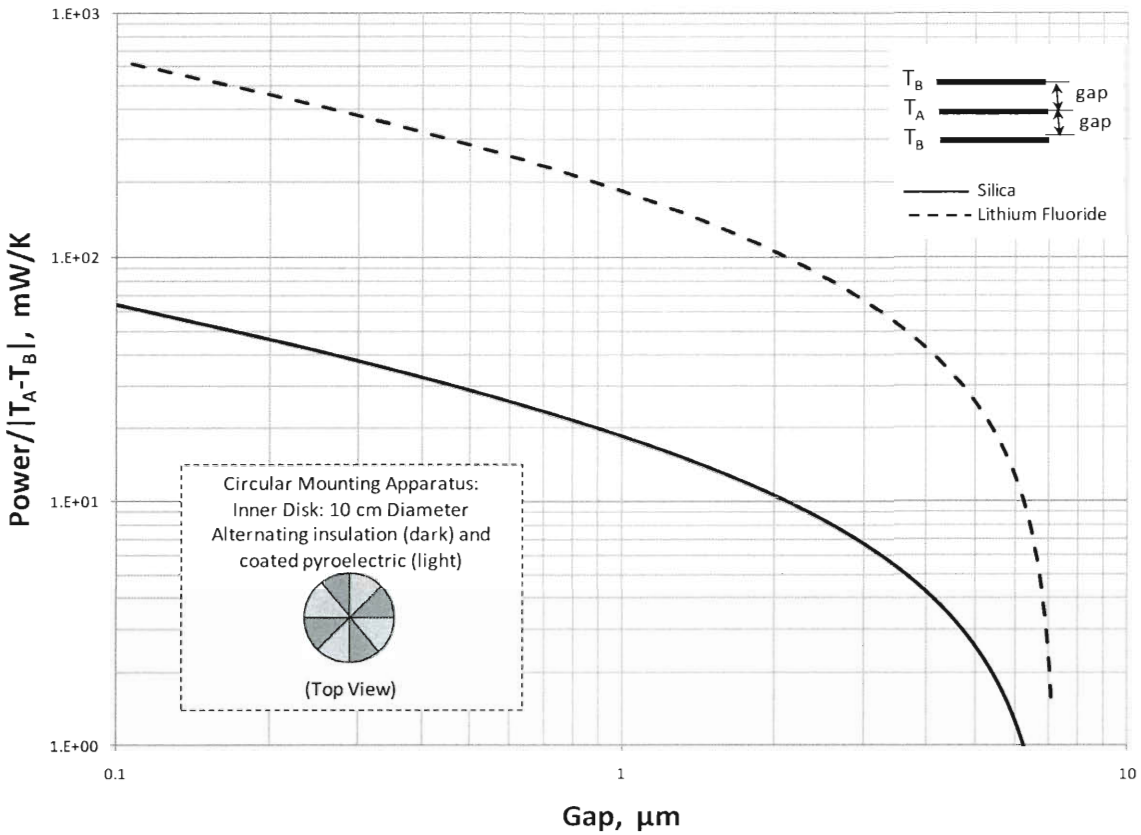

Figure 5.17: Near-field Radiative Transfer for Circular Mounting Apparatus

5.6 Conclusion

An investigation of near-field radiative heat transfer was described for an asymptotic method. This was applied to a unique spacecraft device design that utilizes waste heat for electrical energy generation. The vacuum of space is utilized for cooling, while the pyroelectric material is heated on each side via near-field radiative exchange whereby the heat rate can be maximized. Near-field radiative exchange curves are given for silica and lithium fluoride. In the future, it would be worthwhile to consider operating at higher temperatures, larger multiple devices, additional pyroelectric materials, impacts of thermal expansion, and increased surface area with

microfins. Future development work includes building a prototype of this design, and conducting a vacuum chamber test to simulate the conditions of space where the device will be operated.

5.7 References

[1] Basu, S., Zhang, Z.M., and Fu, C.J., 2009, "Review of Near-Field Thermal Radiation and Its Application to Energy Conversion," International Journal of Energy Research, **33**, pp. 1203-1232.

[2] Volz, S. (ed.), 2006, *Microscale and Nanoscale Heat Transfer (Topics in Applied Physics),* Springer Berlin, Heidelberg, Chap. 1, 4, 6.

[3] Francoeur M., and Menguc M.P., 2008, "Role of Fluctuational Electrodynamics in Near-Field Radiative Heat Transfer," J. Quant. Spectrosc. Radiat. Transfer **109**(2), pp. 280–93.

[4] Joulain K., Mulet J., Marquier F., Carminati R., Greffet J.J., 2005, "Surface Electromagnetic Waves Thermally Excited: Radiative Heat Transfer, Coherence Properties and Casimir Forces Revisited in the Near Field," Surf. Sci. Rep., **57**, pp. 59-112.

[5] Zhang Z., and Menguc M. P., 2007, "Special Issue on Nano/Microscale Radiative Transfer," J. Heat Transfer, **129**(1), pp. 1–2.

[6] Mulet J., Joulain K., Carminati R.,and Greffet J., 2002, "Enhanced Radiative Heat Transfer at Nanometric Distances," Nanoscale Microscale Thermophys. Eng.," **6**(3), pp. 209–22.

[7] Zhang Z., 2007, *Nano/Microscale Heat Transfer,* McGraw Hill, New York, Chap. 10.

[8] Chen G., 2005, *Nanoscale Energy Transport and Conversion: a Parallel Treatment of Electrons, Molecules, Phonons, and Photons*, Oxford University Press, New York, Chap. 5.

[9] Carey V. P., Chen G., Grigoropoulos C., Kaviany M., and Majumdar A. A., 2008, "Review of Heat Transfer Physics," Nanoscale Microscale Thermophys. Eng. **12**(1), pp. 1–60.

[10] Narayanaswamy A., and Chen G., 2008, "Thermal Near-Field Radiative Transfer Between Two Spheres," Phys. Rev. B, **77**(7), pp. 1–12.

[11] Narayanaswamy A., Shen S., and Chen G., 2008, "Near-Field Radiative Heat Transfer Between a Sphere and a Substrate," Phys. Rev. B, **78**(11), pp. 1–4.

[12] Carrillo L. Y., and Bayazitoglu Y., 2010, "Nanosphere Near-Field Radiative Heat Exchange Analysis," AIAA J. Thermophys. Heat Transfer, **24**(2), pp. 309–15.

[13] Mackowski D., and Mishchenko M., 2008, "Prediction of Thermal Emission and Exchange Among Neighboring Wavelength-Sized Spheres," J. Heat Transfer, **130**, pp. 1–7.

[14] Prasher R., 2007, "Thermal Radiation in Dense Nano- and Mircoparticulate Media," J. Appl. Phys., **102**(7), pp. 1–9.

[15] Chew W. C., 1995, *Waves and Fields in Inhomogeneous Media*, IEEE Press, Piscataway, pp. 15–16, 184–189, 375– 428.

[16] Tsang L., Kong J. A., and Ding K., 2000, "Scattering of Electromagnetic Waves: Theories and Application," Wiley, Hoboken, pp. 54–60.

[17] Landau L. D., and Lifshitz E. M., 1985, *Statistical Physics. Part I.*, 3rd ed., Reed Educational Publishing, Boston, pp. 386–393.

[18] Rytov S. M., 1959, "Theory of Electric Fluctuations and Thermal Radiation," US Airforce Cambridge Research Lab, Bedford.

[19] Rytov S. M., Kravtsov Y. A., and Tatarskii V. I., 1989, *Principles of Statistical Radiophysics*, Vol. 3, Springer-Verlag, Berlin, pp. 109–22.

[20] Tai C., 1994, *Dyadic Green's Function in Electromagnetic Theory*, 2nd ed., IEEE Press, Piscataway.

[21] Korenev B. G., 2002, *Bessel Functions and their Applications*, CRC Press, Boca Raton, pp. 17–9.

[22] Abramowitz M., Stegun IA, (editors), 1972, *Handbook of Mathematical Functions*, 9th ed., Dover, New York.

[23] Arfken G., 1985, *Mathematical Methods for Physicists*, 3rd ed., Academic Press, Orlando, pp. 633–4.

[24] Francoeur M., Menguc M. P., and Vaillon R., 2009, "Solution of Near-Field Thermal Radiation in One-Dimensional Layered Media using Dyadic Green's Function and the Scattering Matrix Method," J. Quant. Spectrosc. Radiat. Transfer, **110**(18), pp. 2002–8.

[25] Francoeur M., Menguc M. P., and Vaillon R., 2010, "Local Density of Electromagnetic States within a Nanometric Gap Formed between Two Thin Films Supporting Surface Phonon Polaritons," J. Appl. Phys., **107**(3), pp. 034313–034313-8.

[26] Francoeur M., Menguc M. P., and Vaillon R., 2010, "Spectral Tuning of Near-Field Radiative Flux between Two Thin Silicon Carbide Films," J. Phys. D: Appl Phys, **43**(7), pp. 075501–075501-12.

[27] Carrillo, L. Y., and Bayazitoglu, Y., 2011, "Nanorod Near-Field Radiative Heat Exchange Analysis," J. Quant. Spectrosc. Radiat. Transfer, **112**(3), pp. 412–419.

[28] Carrillo, L. Y., and Bayazitoglu, Y., Submitted Nov. 2010, "Sphere Approximation for Nanorod Near-Field Radiative Heat Exchange Analysis," Nanoscale Microscale Thermophys. Eng.

[29] Wong B., and Menguc M. P., 2010, "Unified Monte Carlo Treatment of the Transport of Electromagnetic Energy, Electrons, and Phonons in Absorbing and Scattering Media," J. Quant. Spectrosc. Radiat. Transfer, **111**(3), pp. 399–419.

[30] Fang, J., Frederich, H., and Pilon, L., 2010, "Harvesting Nanoscale Thermal Radiation Using Pyroelectric Materials," ASME Journal of Heat Transfer, **132**, 092701-1 to 092701-10.

[31] Clingman, W. H., and Moore, R. G., 1961, "Application of Ferroelectricity to Energy Conversion Processes," Journal of Applied Physics, **33**(4), pp. 675-681.

[32] Fatuzzo, E., Kiess, H., and Nitsche, R., 1966, "Theoretical Efficiency of Pyroelectric Power Converters," Journal of Applied Physics, **37**(2), pp. 510-516.

[33] Van Der Ziel, A., 1974, "Solar Power Generation with the Pyroelectric Effect," Journal of Applied Physics, **45**(9), pp. 4128.

[34] Nguyen, H., Navid, A., and Pilon, L., 2010, "Pyroelectric Energy Converter Using Co-polymer P(VDF-TrFE) for Waste Heat Energy Harvesting," Applied Thermal Engineering, **20,** pp. 2127-2137.

[35] Vanderpool D., Yoon, J., and Pilon, L., 2008, "Simulation of a Prototypical Device using Pyroelectric Materials for Harvesting Waste Heat," International Journal of Heat and Mass Transfer, **51**, pp. 5052-5062.

[36] Lang, S., 2005, "Pyroelectricity: From Ancient Curiosity to Modern Imaging Tool," Physics Today, pp 31-36.

[37] Olsen, R., Bruno, D., Briscoe, J., and Jacobs, E., 1985, "Polymer Conversion Cycle of Vinylidene Fluoride-Trifluoroethylene Copolymer," J. Appl. Phys., **57**(11), pp. 5036-5042.

[38] Yannopapas V., 2008, "Non-Local Optical Response of Two-Dimensional Arrays of Metallic Nanoparticles," J. Phys. Condens. Matter, **20**, 325211.

[39] Palik E. D., 1985, *Handbook of Optical Constants of Solids,* Academic Press, New York, pp. 623–798.

[40] Hubbard, N., Culpepper, and M., Howell, L., 2006, "Actuators for Micropositioners and Nanopositioners," Appl. Mech. Rev., **59**, pp. 324-334.

[41] Katz, R.N., 2000, "Piezoceramics," Ceramic Industry, pp 1.

[42] Damjanovic, D., 2006, *The Science of Hysteris*, Vol. 3, Elsevier, Burlington, pp. 337-45, Chap. 4.

[43] Luther, Tappan, Mueller, Mihaila, Volz, Papin, Veauthier, Cardenas, and Stan., 2009 "Nanostructured Metal Foams: Synthesis and Applications", PowderMet., Los Alamos National Lab, US Govt., pp. 1-13.

[44] Faires, V., and Simmang, C., 1978, *Thermodynamics*, 6th ed, MacMillan Publishing, NY.

[45] Sebald G., Guyomar, D., and Agbossou, A., "On thermoelectric and pyroelectric energy harvesting," 2009, Smart Mater. Struct., **18**, 125006, pp. 1-7.

Chapter 6

Conclusions and Future Work

6.1 Conclusions

In this work, the near-field energy exchange has been analyzed for nanospheres, nanorods, and planar configurations. The rigorous analysis involving nanospheres was presented in Chapter 2. This is based on equations derived directly from Maxwell's equations. Spherical surface wave equations were integrated. Mathematical techniques were employed including the DGFs and the FDT. The Poynting vector was calculated followed by an integration over wavelength to calculate the total energy exchange. Equal and unequal radii in the nano-regime were investigated for varied temperatures, gaps, and materials. Radii ratios were also considered. The energy exchange results indicated an approximate difference of three orders of magnitude between lithium fluoride and arsenic triselenide. Lithium fluoride provides the best support for near-field radiative exchange due to its thermophysical and optical properties. Silica and arsenic triselenide were also shown to support near-field exchange but to a lesser degree. Results indicate that it is not enough to know the radii ratio when calculating near-field energy exchange. Equal radii ratio having different individual spherical radii produced approximately a five order of magnitude difference for the cases considered. The nanosphere-to-nanosphere procedure was adapted to calculate energy transfer between a nanosphere and plane. This was compared to previously published theoretical data and experimental data.

In Chapter 3, the procedure for nanorod-to-nanorod is developed and implemented. The spherical wave equations discussed in the previous chapter are replaced with cylindrical waves. The spherical Bessel functions are replaced with cylindrical Bessel functions. Unlike the spherical configuration, the M and N surface waves do not decouple in the cylindrical case. Since they cannot be calculated separately, a matrix must be used to simultaneously deal with these. The cylindrical wave addition theorem is then applied to get an overall wave equation. The nanorod-to-nanorod procedure was applied to cases of different gaps, temperatures, and length-to-diameter ratios. The unit sphere approximation method was introduced and initial results show good agreement with rigorous results. The nanorod-to-plane geometry was investigated.

The unit-sphere approximation is detailed in Chapter 4 and used to analyze a variety of configurations. The basis is to assume that the nanorods are composed of spherical subdivisions. The rigorous sphere-to-sphere method can then be applied. Total energy exchange is calculated using a ray tracing addition assumption. The unit sphere approximation provides a much simpler and computationally inexpensive means of calculation when compared to the rigorous nanorod-to-nanorod method. This occurs because the M and N surface waves do not decouple. The approximation yields a much higher accuracy when compared to far-field alone. Additional results include an interesting dimensionless relationship for the energy exchange vs. length-to-diameter aspect ratio. This discovery was not intuitive.

The experience gained from the earlier chapters is applied to a spacecraft waste heat energy device in Chapter 5. This device makes use of waste heat generated from the many internal spacecraft systems. Typically, large amounts of waste heat are radiated into space at 100% loss. In particular, advanced propulsion systems produce large amounts of waste heat. Pyroelectric

materials generate electricity upon cyclic cooling and heating. The heating will be provided by the waste heat and the cooling by the cold of deep space (~2.7K). Near-field heat transfer is the mechanism for cycling the pyroelectric material temperature. Designs for the device are given. Efficiency of the device when compared to the Carnot cycle is calculated at 17%. The device efficiency compared to the Curzon-Ahlborn efficiency is 32%. The results indicate that the device shows promise, though additional development is needed prior to manufacturing for wide-spread use.

6.2 Future Work

Though the nanosphere-to-plane configuration was compared to experimental data, many other cases were not compared to experimental results. This is due to technology limitations making available experimental data scarce. For completeness it would be advantageous to compare the rest of the theoretical results to experimental data.

Regarding the application, future work includes building a prototype design to test the device. A thermal vacuum test would be important in order to simulate the environment of space. New pyroelectric materials are always being developed. As new pyroelectric materials become available, a consideration should be done to assess the impact to device performance. Thermal expansion effects would also need to be assessed. Possible modifications to the design such as fins to increase the surface area could be considered. Future work would also take into account varied cyclic temperature ranges to identify the range of optimum performance.

Appendix A

Derivation

A structural overview of key equations derived from Maxwell's equations is shown below:

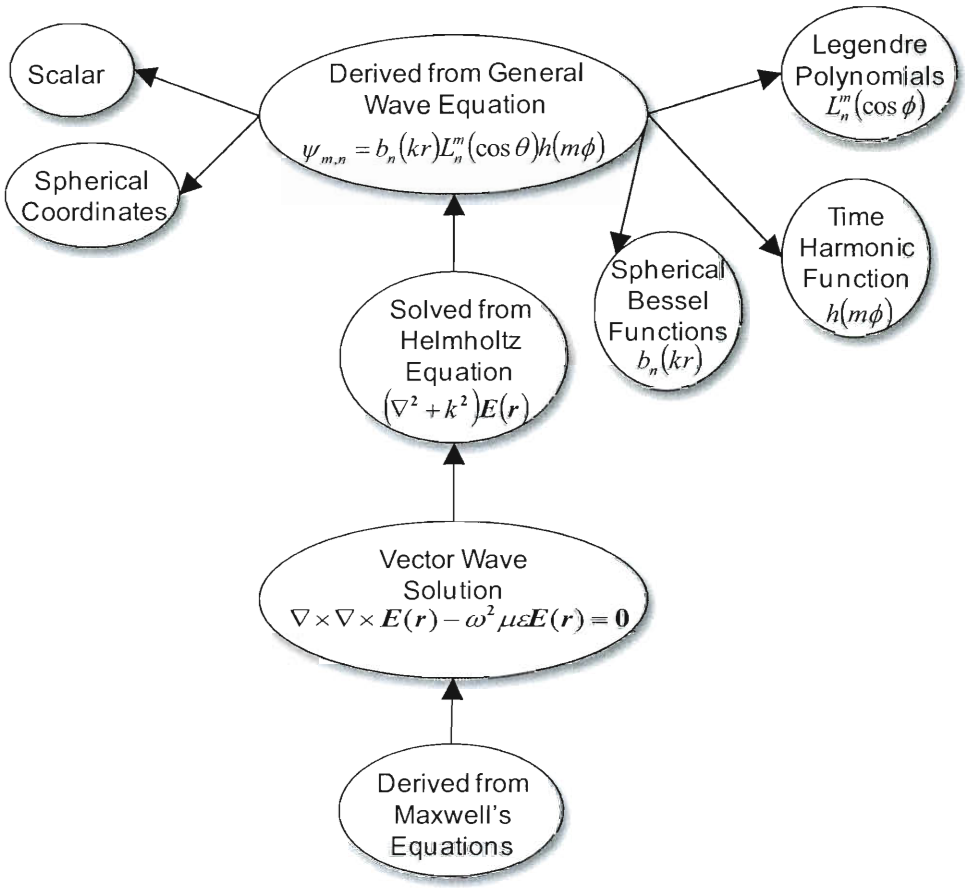

Figure A.1: Structural Equation Overview Schematic

To discuss background, it is noted that electromagnetic fields are defined by electromagnetic theory. These fields exist as waves and are governed by Maxwell's equations. Contributors to

Maxwell's equations include Faraday, Ampere, Gauss, and Poisson. Maxwell's equations in vector notation and SI units are written as follows:

$$\nabla \times \boldsymbol{E}(\boldsymbol{r},t) = -\frac{\partial}{\partial t}\boldsymbol{B}(\boldsymbol{r},t) \tag{A.1}$$

$$\nabla \times \boldsymbol{H}(\boldsymbol{r},t) = \frac{\partial}{\partial t}\boldsymbol{D}(\boldsymbol{r},t) + \boldsymbol{J}(\boldsymbol{r},t) \tag{A.2}$$

$$\nabla \cdot \boldsymbol{B}(\boldsymbol{r},t) = 0 \tag{A.3}$$

$$\nabla \cdot \boldsymbol{D}(\boldsymbol{r},t) = \rho(\boldsymbol{r},t) \tag{A.4}$$

where **E** = electric field (Volts/m), **H** = magnetic field (Amperes/m), **B** = magnetic flux (Webers/m^2), **D** = electric flux (Coulombs/m^2), **J** = current density (Amperes/m^2), and $\rho(\boldsymbol{r},t)$ = charge density (Coulombs/m^3). Note: In the static case, all four equations are needed because the magnetic and electric fields are decoupled in this case. But in the time varying case (electrodynamics), only the first two are. Equation A.1 was discovered by Faraday and is known as Faraday's Law. This equation relates magnetic flux and electric fields. The curl,$\nabla \times$, measures the rotation of the field. So it follows that for a time varying magnetic flux, a rotating electric field is generated. The second of Maxwell's equations given in A.2 is known as Ampere's Law. It was originally discovered without the current density term by Ampere. Maxwell added the current density term to produce the equation in its current form. Ampere's Law relates the electric flux and the magnetic field. Since the curl measures the rotation of the field, it follows that for a time varying electric flux, a rotating magnetic field is generated. The third equation given in A.3 governs the magnetic flux. The divergence, $\nabla \cdot$, measures the flux that exudes from a point. If there is not a sink or a source such that nothing is expanding out or collapsing in, then the divergence is 0. Magnetic charge is currently not known to exist,

therefore there is not magnetic flux source or sink. It follows that this equation is equivalent to 0 as shown. Equation A.4 is expressed as governs the electric flux. From the equation we can see that the divergence of the electric flux as a given point is related to the charge density at that point. This follows directly from Gauss' law which states that the electric flux is created by a charge density. Electrodynamics is covered in this work, thus only the first two equations are needed for the time varying case. This still leaves four magnetic/electric field unknowns namely, **E, H, B, D**. There are several assumptions that are made. The following constitutive relations can be written assuming isotropic, homogeneous, source-free media

$$\boldsymbol{D} = \epsilon \cdot \boldsymbol{E} \tag{A.5}$$

$$\boldsymbol{B} = \mu \cdot \boldsymbol{H} \tag{A.6}$$

where ϵ is the permittivity and μ is the permeability. For free space:

$$\epsilon = \epsilon_0 = 8.854 \times 10^{-12} \text{ Farad/m} \tag{A.7}$$

$$\mu = \mu_0 = 4\pi \times 10^{-7} \text{ Henry/m.} \tag{A.8}$$

Assuming time harmonic fields, the fields can be written as:

$$\boldsymbol{A}(\boldsymbol{r}, t) = \Re e\left[\boldsymbol{A}(\boldsymbol{r}) e^{-i\omega t}\right]. \tag{A.9}$$

Taking the partial derivative of the fields yields:

$$\frac{\partial}{\partial t}\boldsymbol{A}(\boldsymbol{r}, t) = \Re e\left[-i\omega \boldsymbol{A}(\boldsymbol{r}) e^{-i\omega t}\right]. \tag{A.10}$$

Substituting into Maxwell's equations:

$$\nabla \times \boldsymbol{E}(\boldsymbol{r}) = i\omega \boldsymbol{B}(\boldsymbol{r}) \tag{A.11}$$

$$\nabla \times \boldsymbol{H}(\boldsymbol{r}) = -i\omega \boldsymbol{D}(\boldsymbol{r}) + \boldsymbol{J}(\boldsymbol{r}) \tag{A.12}$$

$$\nabla \cdot \boldsymbol{B}(\boldsymbol{r}) = 0 \tag{A.13}$$

$$\nabla \cdot \boldsymbol{D}(\boldsymbol{r}) = \rho(\boldsymbol{r}) \tag{A.14}$$

Substituting constitutive relationship A.6 into A.11 yields

$$\nabla \times \boldsymbol{E}(\boldsymbol{r}) = i\omega\mu \boldsymbol{H}(\boldsymbol{r}). \tag{A.15}$$

Rearranging to isolate the magnetic field:

$$\boldsymbol{H}(\boldsymbol{r}) = \frac{\nabla \times \boldsymbol{E}(\boldsymbol{r})}{i\omega\mu}. \tag{A.16}$$

Taking the curl yields:

$$\nabla \times \boldsymbol{H}(\boldsymbol{r}) = \frac{\nabla \times \nabla \times \boldsymbol{E}(\boldsymbol{r})}{i\omega\mu}. \tag{A.17}$$

Substituting this A.12 results in the following:

$$\frac{\nabla \times \nabla \times \boldsymbol{E}(\boldsymbol{r})}{i\omega\mu} = -i\omega \boldsymbol{D}(\boldsymbol{r}) + \boldsymbol{J}(\boldsymbol{r}). \tag{A.18}$$

Assuming no current source and multiplying the denominator the equation becomes:

$$\nabla \times \nabla \times \boldsymbol{E}(\boldsymbol{r}) = \omega^2 \mu \boldsymbol{D}(\boldsymbol{r}). \tag{A.19}$$

Substituting constitutive relationship A.5 and moving to the left hand side we can write:

$$\nabla \times \nabla \times \boldsymbol{E}(\boldsymbol{r}) - \omega^2 \mu\epsilon \boldsymbol{E}(\boldsymbol{r}) = 0. \tag{A.20}$$

This is known as the Vector Wave Equation. Substituting the vector identity:

$$\nabla \times \nabla \times \boldsymbol{E}(\boldsymbol{r}) = \nabla\big(\nabla \cdot \boldsymbol{E}(\boldsymbol{r})\big) - \nabla^2 \boldsymbol{E}(\boldsymbol{r}) \tag{A.21}$$

the equation becomes:

$$\nabla\big(\nabla \cdot \boldsymbol{E}(\boldsymbol{r})\big) - \nabla^2 \boldsymbol{E}(\boldsymbol{r}) - \omega^2 \mu\epsilon \boldsymbol{E}(\boldsymbol{r}) = 0. \tag{A.22}$$

For the assumption of homogeneous, source free medium, $\nabla \cdot \boldsymbol{E}(\boldsymbol{r}) = 0$. By substitution:

$$-\nabla^2 \boldsymbol{E}(\boldsymbol{r}) - \omega^2 \mu\epsilon \boldsymbol{E}(\boldsymbol{r}) = 0. \tag{A.23}$$

Letting

$$k^2 = \omega^2 \mu\epsilon \tag{A.24}$$

the equation becomes:

$$\nabla^2 \boldsymbol{E}(\boldsymbol{r}) + k^2 \boldsymbol{E}(\boldsymbol{r}) = 0. \tag{A.25}$$

Rewriting yields:

$$(\nabla^2 + k^2)\boldsymbol{E}(\boldsymbol{r}) = 0. \tag{A.26}$$

This is known as Helmholtz equation. A scalar version can be written with the scalar potential $\psi(\boldsymbol{r})$ as:

$$(\nabla^2 + k^2)\psi(\boldsymbol{r}) = 0. \tag{A.27}$$

Solutions for $\boldsymbol{E}(\boldsymbol{r})$ that satisfy the vector wave equation above can be derived by finding the scalar potential. For spherical media, the Helmholtz equation can be written in spherical coordinates as:

$$\frac{1}{r^2}\frac{\partial}{\partial r}\left(r^2\frac{\partial \psi}{\partial r}\right) + \frac{1}{r^2 \sin\theta}\frac{\partial}{\partial \theta}\left(\sin\theta\frac{\partial \psi}{\partial \theta}\right) + \frac{1}{r^2 \sin^2\theta}\frac{\partial^2 \psi}{\partial \phi^2} + k^2\psi = 0. \tag{A.28}$$

This can be solved by employing the separation of variables. Dividing through by ψ, and multiplying through by $r^2 sin^2\theta$:

$$\frac{\sin^2\theta}{\psi}\frac{d}{dr}\left(r^2\frac{d\psi}{dr}\right) + \frac{\sin\theta}{\psi}\frac{d}{d\theta}\left(\sin\theta\frac{\partial \psi}{\partial \theta}\right) + \frac{1}{\psi}\frac{d^2\psi}{d\phi^2} + k^2 r^2 \sin^2\theta = 0 \tag{A.29}$$

The following relationship is defined:

$$\psi = R(r)H(\theta)\Phi(\phi). \tag{A.30}$$

By substitution,

$$\frac{\sin^2\theta}{RH\Phi}\frac{d}{dr}\left(r^2\frac{dH\Phi R(r)}{dr}\right) + \frac{\sin\theta}{RH\Phi}\frac{d}{d\theta}\left(\sin\theta\frac{\partial R\Phi H(\theta)}{\partial \theta}\right) + \frac{1}{RH\Phi}\frac{d^2 RH\Phi(\phi)}{d\phi^2} + k^2 r^2 \sin^2\theta = 0 \tag{A.31}$$

Simplifying,

$$\frac{\sin^2\theta}{R}\frac{d}{dr}\left(r^2\frac{dR}{dr}\right)+\frac{\sin\theta}{H}\frac{d}{d\theta}\left(\sin\theta\frac{\partial H}{\partial\theta}\right)+\frac{1}{\Phi}\frac{d^2\Phi}{d\phi^2}+k^2r^2\sin^2\theta=0. \tag{A.32}$$

Let us separate the ϕ dependence from the equation by employing the following relation where m is constant:

$$\frac{1}{\Phi}\frac{d^2}{d\Phi^2}=-m^2 \tag{A.33}$$

Substituting and dividing through by $sin^2\theta$:

$$\frac{1}{R}\frac{d}{dr}\left(r^2\frac{dR}{dr}\right)+\frac{1}{H\sin\theta}\frac{d}{d\theta}\left(\sin\theta\frac{dH}{d\theta}\right)-\frac{m^2}{\sin^2\theta}+k^2r^2=0. \tag{A.34}$$

Continuing with the separation of variables, we define the following relations:

$$\frac{1}{H\sin\theta}\frac{d}{d\theta}\left(\sin\theta\frac{dH}{d\theta}\right)-\frac{m^2}{\sin^2\theta}=-n(n+1). \tag{A.35}$$

Note: n(n+1) is chosen so as to make the derivation come out cleanly. Substituting this relationship:

$$\frac{1}{R}\frac{d}{dr}\left(r^2\frac{dR}{dr}\right)-n(n+1)+k^2r^2=0. \tag{A.36}$$

Collecting terms the separated equations are:

$$\frac{d}{dr}\left(r^2\frac{dR}{dr}\right)+[k^2r^2-n(n+1)]R=0 \tag{A.37}$$

$$\frac{1}{\sin\theta}\frac{d}{d\theta}\left(\sin\theta\frac{dH}{d\theta}\right)+\left[n(n+1)-\frac{m^2}{\sin^2\theta}\right]H=0 \tag{A.38}$$

$$\frac{d^2\Phi}{d\phi^2} + m\Phi = 0 \tag{A.39}$$

Solutions of A.37 are known as spherical Bessel functions, $b_n(kr)$. Solutions of A.38 are known as associated Legendre functions, $P_n^m(cos\theta)$. Finally, solutions of A.40 are called time harmonic functions, $h(m\theta)$. Thus the general wave equation is written as:

$$\psi_{m,n} = b_n(kr)L_n^m(cos\theta)\mathrm{h}(m\phi) \tag{A.40}$$

Now that we have an idea of origination of the vector wave solution, we begin solving our problem by mathematically constructing it as shown in Figure A.2. The vector wave solution consists of three types of waves: M waves, N waves, and L waves. The L waves are based on a gradient operator and written as:

$$\boldsymbol{L}_{nm}(k,\boldsymbol{r}) = \frac{1}{k}\nabla\,\psi_{nm}(k,r) \tag{A.41}$$

L waves are translationally invariant and therefore of little interest for our purpose of two nanospheres, one of which is a translation of the other. The M and N waves are the crux of what we will need for the vector wave equation. M waves are characterized as

$$\boldsymbol{M}_{nm}(k,\boldsymbol{r}) = \nabla \times \boldsymbol{c}\,\psi_{nm}(r). \tag{A.42}$$

where $\boldsymbol{c}$ is known as the pilot vector. The N waves are expressed as:

$$\boldsymbol{N}_{nm}(k,\boldsymbol{r}) = \frac{1}{k}\nabla \times \boldsymbol{M}(\mathrm{k,r}) = \frac{1}{k}\nabla \times \nabla \times \boldsymbol{c}\,\psi_{nm}(k,r) \tag{A.43}$$

There are similarities between these two equations, though the final equations to represent them are different. Both M and N waves are based on the curl operator. The M waves can be thought of as representing the transverse electric field, while the N wave is associated with the transverse magnetic field. The forms of these equations are quite different for spherical, rectangular, and

cylindrical coordinate systems. The spherical system is unique in that the M and N waves are decoupled.

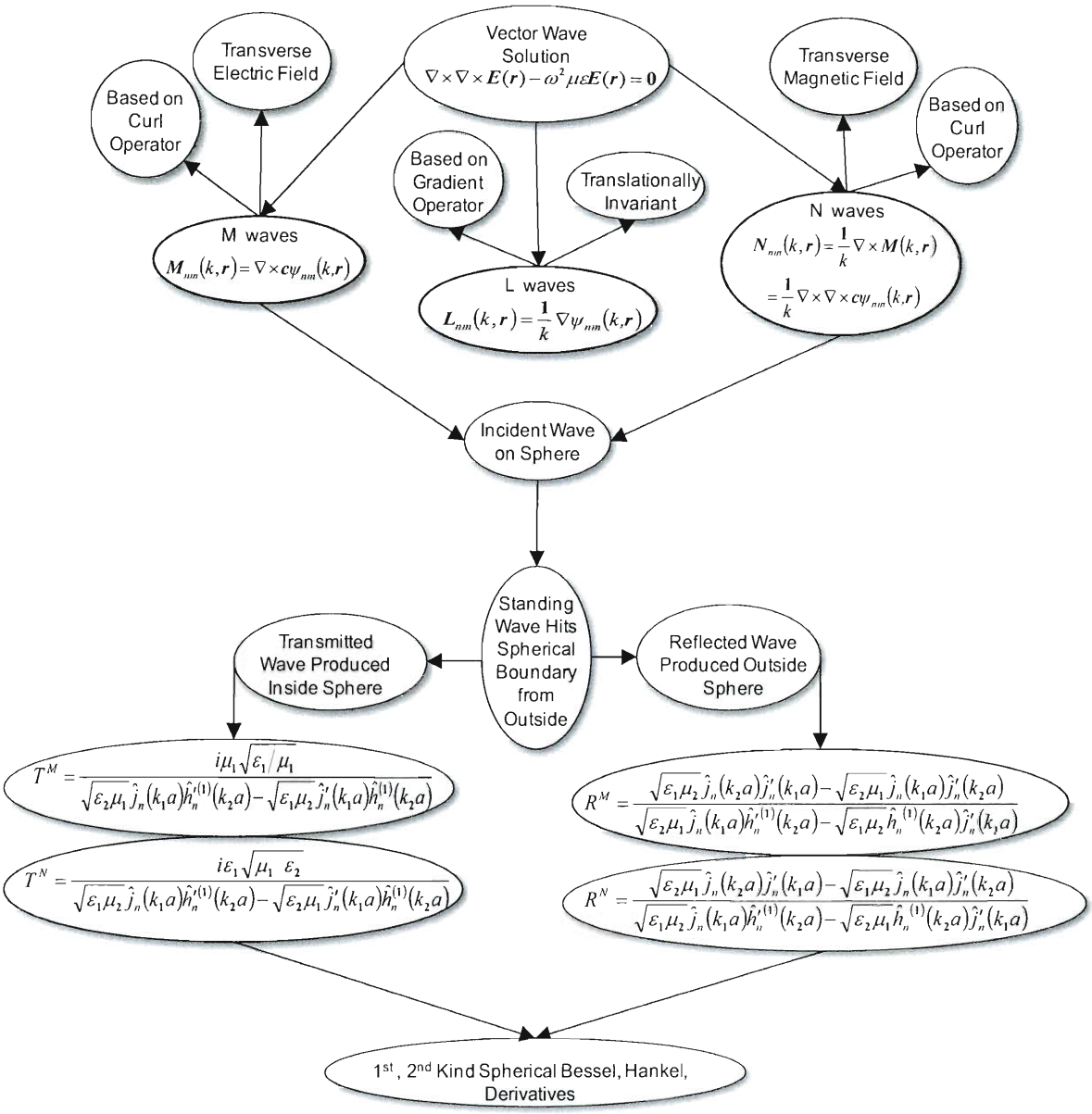

Figure A.2: Mathematical construction of wave solution

Both M and N waves are incident standing waves that hit the spherical boundary from the outside. Each M and N waves produce a reflected wave and transmitted wave. These are governed by the transmitted wave formula and reflected wave formula. The formulas governing these waves are different for the M and N waves. The reflected wave formula for M waves is expressed as:

$$R_c^M = \frac{\sqrt{\epsilon_1\mu_2}\,\hat{\jmath}_n(k_2a)\hat{\jmath}_n'(k_1a) - \sqrt{\epsilon_2\mu_1}\,\hat{\jmath}_n(k_1a)\hat{\jmath}_n'(k_2a)}{\sqrt{\epsilon_2\mu_1}\,\hat{\jmath}_n(k_1a)\hat{h}_n^{(1)'}(k_2a) - \sqrt{\epsilon_1\mu_2}\,\hat{h}_n^{(1)}(k_2a)\hat{\jmath}_n'(k_1a)} \tag{A.44}$$

while the transmitted wave formula is

$$T_c^M = \frac{i\mu_1\sqrt{\frac{\epsilon_1}{\mu_1}}}{\sqrt{\epsilon_2\mu_1}\,\hat{\jmath}_n(k_1a)\hat{h}_n^{(1)'}(k_2a) - \sqrt{\epsilon_1\mu_2}\,\hat{h}_n^{(1)}(k_2a)\hat{\jmath}_n'(k_1a)}. \tag{A.45}$$

For N waves the reflected wave formula is described as

$$R_c^N = \frac{\sqrt{\epsilon_2\mu_1}\,\hat{\jmath}_n(k_2a)\hat{\jmath}_n'(k_1a) - \sqrt{\epsilon_1\mu_2}\,\hat{\jmath}_n(k_1a)\hat{\jmath}_n'(k_2a)}{\sqrt{\epsilon_1\mu_2}\,\hat{\jmath}_n(k_1a)\hat{h}_n^{(1)'}(k_2a) - \sqrt{\epsilon_2\mu_1}\,\hat{h}_n^{(1)}(k_2a)\hat{\jmath}_n'(k_1a)} \tag{A.46}$$

and the transmitted waves as

$$T_c^N = \frac{i\epsilon_1\sqrt{\frac{\mu_1}{\epsilon_2}}}{\sqrt{\epsilon_1\mu_2}\,\hat{\jmath}_n(k_1a)\hat{h}_n^{(1)'}(k_2a) - \sqrt{\epsilon_2\mu_1}\,\hat{h}_n^{(1)}(k_2a)\hat{\jmath}_n'(k_1a)}. \tag{A.47}$$

Both M and N waves are written in terms of spherical Bessel and related functions. The types utilized include first order, second order, Hankel, and derivative spherical Bessel functions. Bessel functions of the first kind are expressed as:

$$j_n(x) \equiv \sqrt{\frac{\pi}{2x}} J_{n+\frac{1}{2}}(x). \tag{A.48}$$

The spherical Bessel functions of the 2nd kind are given as:

$$y_n(x) \equiv \sqrt{\frac{\pi}{2x}} Y_{n+\frac{1}{2}}(x). \tag{A.49}$$

$J_n(x)$ is a general Bessel function of the first kind and $Y_n(x)$ is a general Bessel function of the second kind. The Hankel function is composed of first and second order Bessel functions. The Hankel function is expressed as:

$$h_n(x) = j_n(x) + iy_n(x) \tag{A.50}$$

Additional useful relationships describing a function derived from the Bessel functions are known as the recurrence relations:

$$j'_n(x) = j_{n-1}(x) - \frac{n}{x} j_n(x) \tag{A.51}$$

and

$$y'_n(x) = y_{n-1}(x) - \frac{n}{x} y_n(x). \tag{A.52}$$

Once the wave solution has been written for the coordinate system of each unit sphere, the overall solution must be calculated by combing these solutions as shown in the schematic in Figure A.3. This is done via the vector translation addition theorem expressed as

$$M_{nm}(\boldsymbol{r}) = \sum_{\nu=1}^{\infty} \sum_{\mu=-\nu}^{\nu} \left[M_{\nu\mu}(\boldsymbol{r}') A_{\nu\mu,nm} + N_{\nu\mu}(\boldsymbol{r}') B_{\nu\mu,nm} \right]. \tag{A.53}$$

where $\boldsymbol{r} = \boldsymbol{r}' + \boldsymbol{r}''$ is as shown in Figure A.4.

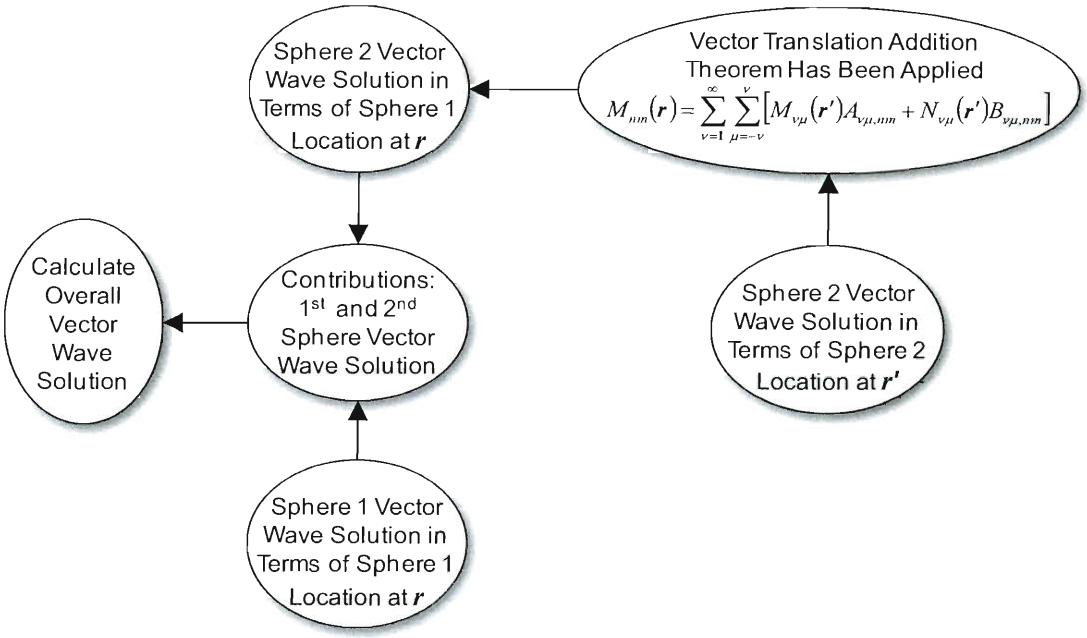

Figure A.3: Calculation of overall vector wave solution

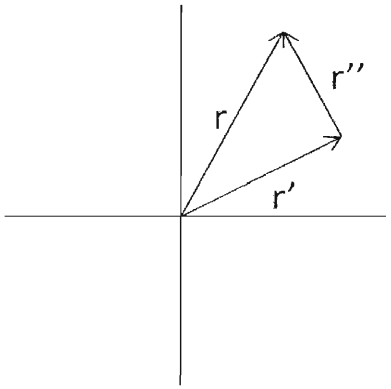

Figure A.4: Vector coordinate system

The center of each sphere is located at the end point of $\boldsymbol{r}$ and $\boldsymbol{r}'$. The vector translation addition theorem transforms the vector M and N waves for the sphere at radius $\boldsymbol{r}'$ to the sphere at radius $\boldsymbol{r}''$. From the M wave, the N wave can be calculated at the new sphere location. Translation matrices A and B are utilized. There have been numerous studies on different methods to

calculate these vector translation matrices A and B. Described in further detail in this section is a method based on the vector that occurs between the sphere location points and calculation of scalar wave translation coefficients utilizing the scalar addition theorem. The scalar addition theorem method involves efficiently calculating a translation matrix $\beta_{\nu\mu,nm}$ using a set of mathematical relationships known as recurrence relations applicable to Bessel functions. The translation matrices ($\beta_{\nu\mu,nm}$) are incorporated within the theorem allowing for the vector wave solutions to be translated to one coordinate system. These solutions can then be added.

Expanding on this procedure, the following relationships were utilized. Note that these equation are written in terms of $\beta_{\nu\mu,nm}$ which is related to the scalar wave addition theorem.

$$A_{\nu\mu,nm} = B_{\nu\mu,nm} + m^{\mp}_{\nu+1,\mu-1}\beta_{\nu+1,\mu-1,nm} + m^{++}_{\nu-1,\mu-1}\beta_{\nu-1,\mu-1,nm} + \quad \text{(A.54)}$$

$$m^{--}_{\nu+1,\mu+1}\beta_{\nu+1,\mu+1,nm} + m^{+-}_{\nu-1,\mu+1}\beta_{\nu-1,\mu+1,nm} + m^{-0}_{\nu+1,\mu}\beta_{\nu+1,\mu,nm} +$$

$$m^{+0}_{\nu-1,\mu}\beta_{\nu-1,\mu,nm}$$

where

$$m^{-+}_{\nu+1,\mu-1} = r'' \sin\theta'' \frac{e^{-i\phi''}}{2} \frac{1}{\nu+1} \sqrt{\frac{(\nu-\mu+2)(\nu-\mu+1)}{(2\nu+1)(2\nu+3)}} \quad \text{(A.55)}$$

$$m^{++}_{\nu-1,\mu-1} = r'' \sin\theta'' \frac{e^{-i\phi''}}{2} \frac{-1}{\nu} \sqrt{\frac{(\nu+\mu-1)(\nu+\mu)}{(2\nu-1)(2\nu+1)}} \quad \text{(A.56)}$$

$$m^{--}_{\nu+1,\mu+1} = r'' \sin\theta'' \frac{e^{i\phi''}}{2} \frac{-1}{\nu+1} \sqrt{\frac{(\nu+\mu+2)(\nu+\mu+1)}{(2\nu+1)(2\nu+3)}} \quad \text{(A.57)}$$

$$m^{+-}_{\nu-1,\mu+1} = r'' \sin\theta'' \frac{e^{i\phi''}}{2} \frac{1}{\nu} \sqrt{\frac{(\nu-\mu-1)(\nu-\mu)}{(2\nu-1)(2\nu+1)}} \quad \text{(A.58)}$$

$$m_{\nu+1,\mu}^{-0} = r'' \cos\theta'' \frac{1}{\nu+1}\sqrt{\frac{(\nu+\mu+1)(\nu-\mu+1)}{(2\nu+1)(2\nu+3)}} \tag{A.59}$$

$$m_{\nu-1,\mu}^{+0} = r'' \cos\theta'' \frac{1}{\nu}\sqrt{\frac{(\nu+\mu)(\nu-\mu)}{(2\nu-1)(2\nu+1)}} \tag{A.60}$$

and

$$B_{\nu\mu,nm} = n_{\nu,\mu-1}^{0+}\beta_{\nu,\mu-1,nm} + n_{\nu,\mu+1}^{0-}\beta_{\nu,\mu+1,nm} + n_{\nu\mu}^{00}\beta_{\nu\mu,nm} \tag{A.61}$$

where

$$n_{\nu\mu}^{00} = r'' cos\theta'' \frac{i\mu}{\nu(\nu+1)} \tag{A.62}$$

$$n_{\nu,\mu-1}^{0+} = r'' sin\theta'' \frac{e^{-i\phi''}}{2} i\sqrt{\frac{(\nu-\mu+1)(\nu+\mu)}{\nu(\nu+1)}} \tag{A.63}$$

$$n_{\nu,\mu+1}^{0-} = r'' sin\theta'' \frac{e^{i\phi''}}{2} i\sqrt{\frac{(\nu+\mu+1)(\nu-\mu)}{\nu(\nu+1)}} \tag{A.64}$$

The two spheres are centered at different values of z with the same θ, ϕ. The center of one sphere is kd away from the center of the other sphere. So $\boldsymbol{r}''$ in the cylindrical coordinate system yields.

$$\boldsymbol{r}'' = 0\hat{\theta} + 0\hat{\phi} + kd\hat{z} \tag{A.65}$$

Substituting this causes several terms in the above equations to go to 0 since $sin\theta''$ goes to 0. The equations then look as follows:

$$A_{\nu\mu,nm} = +m^{-0}_{\nu+1,\mu}\beta_{\nu+1,\mu,nm} + m^{+0}_{\nu-1,\mu}\beta_{\nu-1,\mu,nm} \tag{A.66}$$

$$= \left(kd\frac{1}{\nu+1}\sqrt{\frac{(\nu+\mu+1)(\nu-\mu+1)}{(2\nu+1)(2\nu+3)}}\right)\beta_{\nu+1,\mu,nm} + \left(kd\frac{1}{\nu}\sqrt{\frac{(\nu+\mu)(\nu-\mu)}{(2\nu-1)(2\nu+1)}}\right)\beta_{\nu-1,\mu,nm}$$

and

$$B_{\nu\mu,nm} = n^{00}_{\nu\mu}\beta_{\nu\mu,nm} = kd\frac{i\mu}{\nu(\nu+1)} \tag{A.67}$$

The translation matrix $\beta_{\nu\mu,nm}$ equations applied in this work are now discussed. The scalar wave addition theorem is written as:

$$\psi_{nm} = \sum_{\nu=0}^{\infty}\sum_{\mu=-\nu}^{\nu}\psi_{\nu\mu}(\boldsymbol{r}')\beta_{\nu\mu,nm} \tag{A.68}$$

where $\beta_{\nu\mu,nm}$ is the translation matrix. Taking the partial derivative with respect to z of both sides yields,

$$a^{+}_{nm}\psi_{n+1,m}(\boldsymbol{r}) = -a^{-}_{nm}\psi_{n-1,m}(\boldsymbol{r}) + \sum_{\nu=0}^{\infty}\sum_{\mu=-\nu}^{\nu}a^{+}_{\nu\mu}\psi_{\nu-1,\mu}(\boldsymbol{r}')\beta_{\nu\mu,nm} \tag{A.69}$$

Rearranging terms, equating terms in series, and expanding summation yields,

$$a^{+}_{nm}\beta_{\nu\mu,n+1,m} = -a^{-}_{nm}\beta_{\nu\mu,n-1,m} + a^{+}_{\nu-1,\mu}\beta_{\nu-1,\mu,nm} + a^{-}_{\nu+1,\mu}\beta_{\nu+1,\mu,nm}. \tag{A.70}$$

Given $\beta_{\nu-1,\mu,nm}$ and $\beta_{\nu\mu,nm}$ for $(\nu,\mu) \in S$, from this equation we can solve for $\beta_{\nu-1,\mu,n+1,m}$ by dividing the equation by a_{nm}^{+}. This is written as:

$$\beta_{\nu\mu,n+1,m} = \frac{1}{a_{nm}^{+}}\left[-a_{nm}^{-}\beta_{\nu\mu,n-1,m} + a_{\nu-1,\mu}^{+}\beta_{\nu-1,\mu,nm} + a_{\nu+1,\mu}^{-}\beta_{\nu+1,\mu,nm}\right]. \qquad \text{(A.71)}$$

This equation can be continuously applied for all n, m in ψ_{nm} until a converged solution is reached.

Once the M, N waves for each sphere have been combined via the vector addition theorem just described, several mathematical manipulations are employed as indicated in Figure A.5. Details of the application of mathematical techniques are shown here.

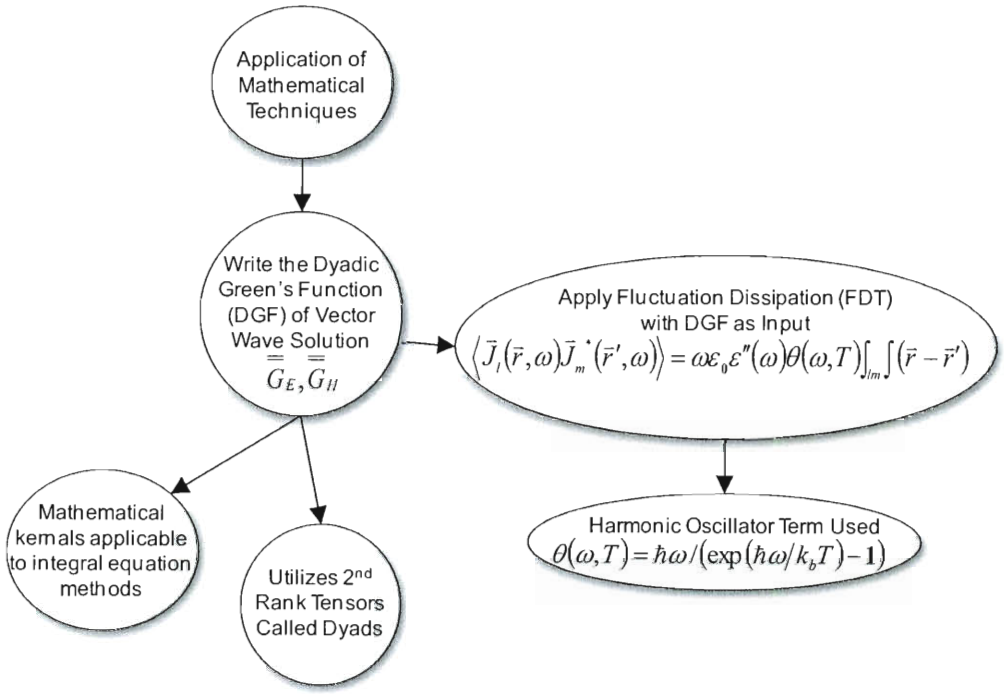

Figure A.5: Application of Mathematical Techniques

The mathematical techniques allow for the incorporation of the fluctuating nature of the current involved. The current responsible for creating the N and M waves is fluctuating due to the chaotic motion of the charged particles that produce it. The radiation emitted by this thermally fluctuating EM field can be determined by calculating the associated electric and magnetic field. The Fourier component of the fluctuating electric and magnetic field at any point r_1 outside a volume containing the sources is:

$$E(\vec{r_1},\omega) = i\omega\mu_0 \int_V \overline{\overline{G_E}}(\vec{r_1},\vec{r},\omega)\cdot\vec{J}(\vec{r},\omega)d^3r \tag{A.72}$$

$$H(\vec{r_1},\omega) = \int_V \overline{\overline{G_H}}(\vec{r_1},\vec{r},\omega)\cdot\vec{J}(\vec{r},\omega)d^3r \tag{A.73}$$

where $\overline{\overline{G_E}}(\vec{r_1},\vec{r},\omega)$and $\overline{\overline{G_H}}(\vec{r_1},\vec{r},\omega)$ are the dyadic Green's functions (DGF) due to a source at $\vec{r}$. Here an additional mathematical technique involving kernals called DGFs which utilize 2nd rank dyad tensors is incorporated. The integration is performed over the entire volume V containing the source. μ_0 is the permeability of vacuum, and $\vec{J}(\vec{r},\omega)$is the Fourier component of the fluctuating current due to the fluctuating charged particles. To deal with the phenomena of fluctuation, a statistical average must be involved within the formulation. This is denoted as $\langle\cdot,\cdot\rangle$. The equation can be further manipulated by the application of the Fluctuation Dissipation Theorem (FDT). This theorem states that the density matrix for thermal fluctuations can be expressed in terms of $\theta(\omega,T)$ or the mean energy of the quantum oscillator where:

$$\theta(\omega,T) = \hbar\omega/\left(\exp\left(\frac{\hbar\omega}{k_bT}\right)-1\right). \tag{A.74}$$

There are several different forms of the FDT. The one utilized in this work is shown as follows:

$$\langle\vec{J}_l(\vec{r},\omega)\vec{J}_m{}^*\left(\vec{r'},\omega\right)\rangle = \omega\varepsilon_0\varepsilon''(\omega)\theta(\omega,T)\int_{lm}\int(\vec{r}-\vec{r}') \tag{A.75}$$

With this information, we are able to take the next step of calculating the Poynting vector, *E x H,* from the acquired electromagnetic wave fields E and H. To compute the spectral Poynting vector, we take the cross product of the electric and magnetic fields:

$$\langle E_{i\omega}, H^{*}_{j\omega} \rangle =$$

$$i\omega\mu_0 \int_V d^3r \int_V d^3r' \left\{ \overline{\overline{G_E}}(\vec{r_1}, \vec{r}, \omega) \overline{\overline{G_H}^{*}} \left(\vec{r_1}, \vec{r'}, \omega \right) \langle \vec{J}_l(\vec{r}, \omega) \vec{J}_m{}^{*} \left(\vec{r'}, \omega \right) \rangle \right\} \qquad \text{(A.76)}$$

where $\varepsilon"(\omega)$ is the imaginary part of the dielectric function, and ε_0 is the permittivity of a vacuum.

The final step is to calculate the Poynting vector which will enable the acquisition of the radiative exchange between the spheres. The specifics of this are given below:

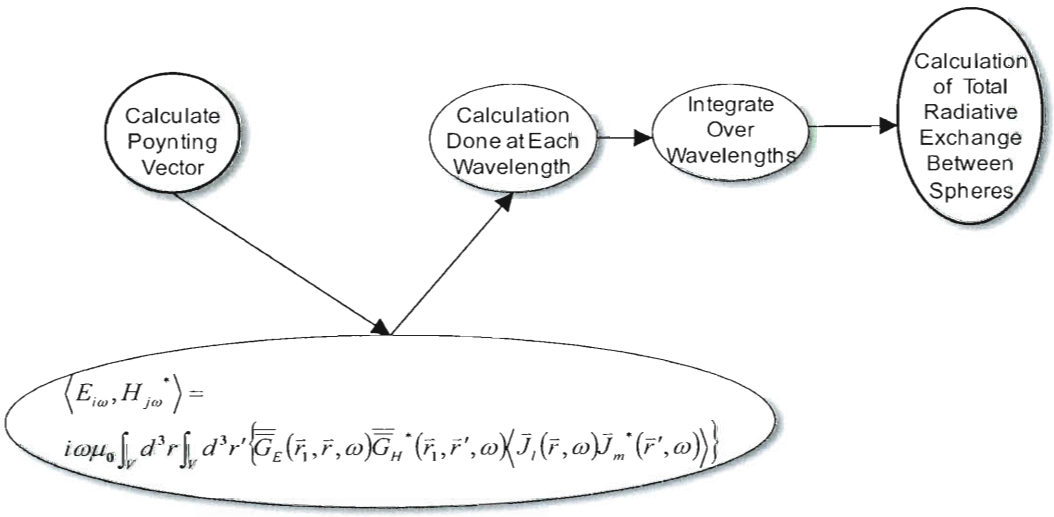

Figure A.6: Radiative exchange between the spheres

We can now write the Poynting vector by substitution:

$$\langle E_i(\vec{r_1},\omega), H_j{}^*(\vec{r_1},\omega)\rangle = \frac{i\varepsilon_0\varepsilon''(\omega)\mu_0\omega^2\theta(\omega,T)}{T}\int_V d^3r\left\{\left(\overrightarrow{G_E}(\vec{r_1},\vec{r},\omega)\overrightarrow{G_H}^*\left(\vec{r_1},\vec{r'},\omega\right)\right)_{ii}\right\} \tag{A.77}$$

The wavelength and material properties, in particular, the refractive index, are the final elements needed to complete calculation of the spectral radiative transfer between spheres. Integration can then be done over the wavelength to produce the total radiative transfer between the spheres.

Appendix B

Dyadic Green's Function

A key element of the Fluctuation Dissipation theorem is the utilization of the Dyadic Green's Function (DGF). DGF's are mathematical kernals that are applicable to many integral equation methods. In this case we apply it to the equations describing the interaction of the EM waves in terms of various geometries considering an excitation source and boundary values. A dyad is a second rank tensor formed from 2 vectors such as a and b, and has the following property operation on vector c:

$$ab \cdot c = a(b \cdot c).$$

A tensor represents a physical property that under a coordinate rotation is invariant. A Dyadic Green's function is a dyad that relates a vector field to its vector current source. The DGF is typically written in terms of the applicable vector wave function. There are two types of DGF: magnetic and electric. This work focuses on electric. The electric DGF gives a specific relation between the electric field and the current density that can be utilized to solve for the radiant power.

There are two types of DGFs: the scattering DGF, G_S, and the unbounded free space DGF, G_0. Together, these form the overall DGF for a given region. This property of acquiring the overall DGF by summing the scattering and unbounded DGF is known as the scattering superposition. The unbounded free space DGF is used when the source is within the region of investigation. It accounts for the contributions from the source. The scattering DGF accounts

for the contributions from transmission or reflection at the interface. The scattering DGF is constructed by including the scattering dyadic coefficients calculated by taking the boundary conditions satisfied by the unbounded free space DGF at the interfaces. The unbounded free space DGF for a cylinder derived from the vector wave function in cylindrical coordinates can be found in [1]. Detailed derivation information including the scattering DGF for a cylindrical geometry with the transmission and reflection coefficients obtained in compact matrix form can be found in [2-5]. Practical applications can utilize developed Mathematica software as shown by Li et.al in [2] for calculation of DGFs. The developed code allows for the calculated DGF to be expressed in terms of transmission and reflection matrices, or permeability, permittivity, and propagation constants. For details on the application of DGFs for waves and fields to different geometric configurations, the reader is referred to [6].

Additional Resources

[1] Tai C., Dyadic Green's Function in Electromagnetic Theory. 2nd ed. Piscataway: IEEE Press; 1994.

[2] Li, L., Leong, M., and Yeo, T., Symbolic Derivation and Numeric Computation of Dyadic Green's Functions Using Mathematica. IEEE Antennas and Propagation Magazine; 2001, 43(1): 108-118.

[3] Li, L., Leong, M., and Yeo, T., On the Eigenfunction Expansion of DGF in Planar Stratified Media. Journal of EM Waves and Application; 1994, 8(6):667-678.

[4] Li, L., Leong, M., and Yeo, T., Electromagnetic DGF in Spherically Multilayered Media. IEEE Transactions on Microwave Theory and Techniques; 1994, 12:2302-2310.

[5] Li, L., Leong, M., and Yeo, T., and Kooi, P., Electromagnetic Dyadic Green's Function in Spectral Domain for Multilayered Cylinders. Journal of Electromagnetic Waves and Applications; 2000, 14: 961-985.

[6] Chew WC. Waves and Fields in Inhomogeneous Media. Piscataway: IEEE Press; 1995. p. 15-16, 184-189, 375-428.